



Mechanics of motility initiation and motility arrest in crawling cells



Pierre Recho^{a,b}, Thibaut Putelat^c, Lev Truskinovsky^{a,*}

^a LMS, CNRS-UMR 7649, Ecole Polytechnique, Route de Saclay, 91128 Palaiseau, France

^b Physicochimie Curie, CNRS-UMR168, Institut Curie, Centre de Recherche, 26 rue d'Ulm, F-75248 Paris Cedex 05, France

^c DEM, Queen's School of Engineering, University of Bristol, Bristol BS8 1TR, UK

ARTICLE INFO

Article history:

Received 19 December 2014

Received in revised form

21 July 2015

Accepted 6 August 2015

Available online 7 August 2015

ABSTRACT

Motility initiation in crawling cells requires transformation of a symmetric state into a polarized state. In contrast, motility arrest is associated with re-symmetrization of the internal configuration of a cell. Experiments on keratocytes suggest that polarization is triggered by the increased contractility of motor proteins but the conditions of re-symmetrization remain unknown. In this paper we show that if adhesion with the extracellular substrate is sufficiently low, the progressive intensification of motor-induced contraction may be responsible for both transitions: from static (symmetric) to motile (polarized) at a lower contractility threshold and from motile (polarized) back to static (symmetric) at a higher contractility threshold. Our model of lamellipodial cell motility is based on a 1D projection of the complex intra-cellular dynamics on the direction of locomotion. In the interest of analytical transparency we also neglect active protrusion and view adhesion as passive. Despite the unavoidable oversimplifications associated with these assumptions, the model reproduces quantitatively the motility initiation pattern in fish keratocytes and reveals a crucial role played in cell motility by the nonlocal feedback between the mechanics and the transport of active agents. A prediction of the model that a crawling cell can stop and re-symmetrize when contractility increases sufficiently far beyond the motility initiation threshold still awaits experimental verification.

© 2015 Elsevier Ltd. All rights reserved.

1. Introduction

The ability of cells to self-propel is essential for many biological processes. In the early life of an embryo, stem cells move to form tissues and organs. During the immune response, leukocytes migrate through capillaries to attack infections. Wound healing requires the motion of epithelial cells. While the biochemistry of such motility is rather well understood, the underlying *mechanics* of active continuum media is still in the stage of development (Bray, 2000; Mogilner, 2009; Carlsson and Sept, 2008; Joanny and Prost, 2011; Adler and Givli, 2013; Ziebert and Aranson, 2013; Giomi and DeSimone, 2014; Recho et al., 2014; Cox and Smith, 2014).

At a very general level, a cell can be viewed as an elastic ‘bag’ whose interior is separated from the exterior by a bi-layer lipid membrane. The membrane is attached from inside to a thin cortex – an active muscle-type layer maintaining the cell's shape. The interior is filled with a passive medium, the cytosol, where all essential cell organelles are immersed. The active machinery inside the cytosol ensuring self-propulsion is contained in the cytoskeleton: a perpetually renewed network of

* Corresponding author.

actin filaments cross-linked by myosin motors that can inflict contractile stresses. The cytoskeleton can be mechanically linked to the cell exterior through adhesion proteins (Alberts et al., 2002).

The elementary mechanisms responsible for the steady crawling of keratocytes (flattened cells with fibroblastic functions) have been identified (Abercrombie, 1980; Bell, 1984; Stossel, 1993; Bellairs, 2000). The advance starts with protrusion driven by active polymerization of the actin network in the frontal area of the cell (the lamellipodium) with a simultaneous formation of adhesion clusters at the advancing edge. After the adhesion of the protruding part of the cell is secured, the cytoskeleton contracts thanks to the activity of myosin motors. This contraction leads to the detachment at the rear and lessening of the actin network through de-polymerization. All these *active* phenomena are driven by ATP hydrolysis and are highly synchronized which allows the cell to move with a stable shape and relatively constant velocity (Barnhart et al., 2011).

The *initiation* of such motility requires a polarization of the cell which is a process that discriminates the leading edge from the trailing edge. The implied symmetry breaking turns a symmetric stationary configuration of a cell into a polar motile configuration. While both contraction and protrusion contribute to steady state cell migration, contraction appears to be the dominating mechanism of polarization: it has been shown experimentally that motility initiation in keratocytes may be triggered by raising the contractility of myosin (Verkhovsky et al., 1999; Csucs et al., 2007; Lombardi et al., 2007; Yam et al., 2007; Vicente-Manzanares et al., 2009; Poincloux et al., 2011). It is also known that cells may self-propel by contraction only (Keller et al., 2002).

In physical terms, the contraction-driven polarization/motility is performed by ‘pullers’ (contractile agents) while ‘pushers’ (protrusive agents) remain largely disabled. Some numerical models suggest that the relative role of ‘pushers’ and ‘pullers’ in cellular motility may be tightly linked to the task to be performed (Simha and Ramaswamy, 2002; Saintillan and Shelley, 2012) and even to the nature of the cargo (Recho and Truskinovsky, 2013). However, it is still not fully understood why in case of keratocytes the motility initiation is primarily contraction-driven. In contrast to motility initiation, the reciprocal process of motility *arrest* is associated with re-symmetrization and such symmetry recovery is a typical precursor of cell division (Stewart et al., 2011; Lancaster et al., 2013; Lancaster and Baum, 2014). It is not yet clear whether re-symmetrization is also predominantly contraction-driven and if yes, whether it requires contractility reduction or contractility increase beyond the motility initiation threshold. It is, however, known that some cells can switch from static to motile state as a result of a decrease in the level of contractility (Liu et al., 2010; Hur et al., 2011).

A large variety of modeling approaches targeting cell motility mechanisms can be found in the literature, see the reviews by Rafelski and Theriot (2004), Carlsson and Sept (2008), Mogilner (2009), and Wang et al. (2012). In some models, the actin network is viewed as a highly viscous active *fluid* moving through a cytoplasm by generating internal contractile stresses (Alt and Dembo, 1999; Oliver et al., 2005; Herant and Dembo, 2010; Kimpton et al., 2014). In other models, the cytoskeleton is represented by an active *gel* whose polar nature is modeled in the framework of the theory of liquid crystals (Kruse et al., 2005; Joanny et al., 2007; Jülicher et al., 2007; Joanny and Prost, 2011; Callan-Jones and Jülicher, 2011). The active gel theory approach, which we basically follow in this study without an explicit reference to local orientational order, was particularly successful in reproducing rings, asters, vortices and some other sub cellular structures observed in vivo (Doubrovinski and Kruse, 2007; Sankararaman and Ramaswamy, 2009; Doubrovinski and Kruse, 2010; Du et al., 2012). At sufficiently fast time scales, the cytoskeleton can be also modeled as an active *solid* with a highly nonlinear scale-free rheology (Broedersz and MacKintosh, 2014; Pritchard et al., 2014).

Various specific sub-elements of the motility mechanism have been subjected to careful mechanical study. Thus, it was shown that in some cases the plasmic membrane with an attached cortex can be viewed as a passive elastic surface and modeled by phase field methods allowing one to go smoothly through topological transitions (Wang et al., 2012; Giomi and DeSimone, 2014). In other cases, the membrane may also play an active role, for instance, an asymmetric distribution of channels on the surface of the membrane can be responsible for a particular mechanism of cell motility relying on variation of osmotic pressure (Stroka et al., 2014). While most models assume that the cell membrane interacts with the exterior of the cell through passive viscous forces, active dynamics of adhesion complexes has recently become an area of intense research driven in part by the finding of a complex dependence of the crawling velocity on the adhesive properties of the environment (DiMilla et al., 1991; Novak et al., 2004; Deshpande et al., 2008; Gao et al., 2011; Lin et al., 2008; Ronan et al., 2014; Lin, 2010; Ziebert and Aranson, 2013). The account of other relevant factors, including realistic geometry, G-actin transport, Rac/Rho-regulation, etc., have led to the development of rather comprehensive models that can already serve as powerful predictive tools (Rubinstein et al., 2009; Wolgemuth et al., 2011; Tjhung et al., 2012; Giomi and DeSimone, 2014; Barnhart et al., 2015).

The more focused problem of finding the detailed mechanism of motility initiation is most commonly addressed in the framework of theories emphasizing polymerization-driven protrusion (Mogilner and Edelstein-Keshet, 2002; Dawes et al., 2006; Bernheim-Groswasser et al., 2005; Schreiber et al., 2010; Campas et al., 2012; Hodge and Papadopoulos, 2012). With such emphasis on ‘pushers’, spontaneous polarization was studied by Kozlov and Mogilner (2007), Callan-Jones et al. (2008), John et al. (2008), Hawkins et al. (2009b), Hawkins and Voituriez (2010), Doubrovinski and Kruse (2011), and Blanch-Mercader and Casademunt (2013). In Banerjee and Marchetti (2011), Ziebert et al. (2012) and Ziebert and Aranson (2013), polarization was interpreted as a result of an inhomogeneity of adhesive interactions. Yet another group of authors have successfully argued that cell polarity may be induced by a Turing-type instability (Mori et al., 2008; Altschuler et al., 2008; Vanderlei et al., 2011; Jilkin and Edelstein-Keshet, 2011). Such a variety of modeling approaches is a manifestation of the fact that very different mechanisms of motility initiation are engaged in cells of different types.

The observation that contraction may be the leading factor behind the polarization of *keratocytes* has been broadly discussed in the literature. It was realized that active contraction creates an asymmetry-amplifying positive feedback because it causes actin flow which in turn carries the regulators of contraction (Kruse et al., 2003; Ahmadi et al., 2006; Salbreux et al., 2009; Recho et al., 2013; Barnhart et al., 2015). In constrained conditions such positive feedback generates peaks in the concentration of stress activators (myosin motors) (Bois et al., 2011; Howard et al., 2011) and this patterning mechanism was used to model polarization induced by angular cortex flow (Hawkins et al., 2009a, 2011). Closely related heuristic models of the Keller–Segel type (Perthame, 2012) describing symmetry breaking and localization were independently proposed by Kruse and Jülicher (2003) and Calvez et al. (2010). In all these models, however, the effect of contraction (pullers) was obscured by the account of other mechanisms, in particular, polymerization induced protrusion (pushers), and the focus was on generation of internal flow and the resulting pattern formation, rather than on the problem of ensuring steady *translocation* of a cell.

This shortcoming was overcome in more recent models of contraction-induced polarization relying on splay instability in an active gel (Tjhung et al., 2012, 2015; Giomi and DeSimone, 2014). In these models, however, ‘pushers’ were not the only players, in particular, polarization was induced by a local phase transition from non-polar to polar gel. In Callan-Jones and Voituriez (2013), the motility initiation was attributed to a contraction-induced instability in a poro-elastic active gel permeated by a solvent. Here again the non-contraction active mechanism was involved as well and therefore the domineering role of contraction could not be made explicit.

The goal of the present paper is to focus on the special role of *bare contraction* in symmetry breaking processes by studying a minimalistic, analytically transparent model of motility initiation in a segment of an active gel. Following previous work, we exploit the Keller–Segel mechanism, but now in a *free boundary* setting, and show that the underlying symmetry breaking instability is fundamentally similar to an uphill diffusion of the Cahn–Hilliard type. In contrast to most previous studies, our contraction driven *translocation* of a cell is caused exclusively by the internal flow generated by molecular motors (pullers) and no other active agents are involved. Each ‘puller’ contributes to the stress field and simultaneously undergoes biased random motion resulting in an uphill diffusion along the corresponding stress gradient. In other words our ‘pullers’ (active cross-linkers) use the continuum environment (passive actin network) as a medium through which they interact and self-organize.

We emphasize that the contraction mechanism of polarization and motility (Recho et al., 2013, 2014) is conceptually very close to chemotaxis, however, instead of *chemical* gradients, the localization and motility is ultimately driven by the self-induced *mechanical* gradients. More specifically, the pullers propel the passive medium by inflicting contraction which creates an autocatalytic effect since the pullers are themselves advected by this medium (Mayer et al., 2010). The inevitable build up of mechanical gradients in these conditions is limited by diffusion which resists the runaway and provides the negative feedback. After the symmetry of the static configuration is broken in the conditions where matter can circulate, the resultant contraction-driven flow ensures the perpetual renewal of the network and then frictional interaction with the environment allows for the steady *translocation* of the cell body.

The next natural question is how such steady translocations can be halted. For instance, if motility initiation is contraction-driven, can motility arrest be also contraction driven and what a steadily moving cell can do in order to stop and symmetrize? Several computational models provided an indication that motility initiation and motility arrest may be related to a re-entrant behavior of the same branch of motile regimes (Kruse and Jülicher, 2003; Tjhung et al., 2012; Recho et al., 2013; Giomi and DeSimone, 2014). To make the link between motility initiation and motility arrest more transparent we study in this paper an *analytically* tractable problem which captures the complexity of the underlying physical phenomena. While most of the elements of the proposed model (Recho et al., 2013, 2014) have been anticipated by some comprehensive computational approaches (e.g. Rubinstein et al., 2009), it was previously not apparent that the initiation of motility, steady *translocation* and the arrest of motility can be *all* captured in such a minimal setting.

Our model of lamellipodial cell motility is based on a 1D projection of the complex intra-cellular dynamics on the direction of locomotion. In the interest of analytical transparency, we decouple the dynamics of actin and myosin by assuming infinite compressibility of the cross-linked actin network (Jülicher et al., 2007; Rubinstein et al., 2009). To ensure that the crawling cell maintains its size, we introduce a simplified cortex/osmolarity mediated quasi-elastic interaction between the front and the back of the self-propelling fragment (Banerjee and Marchetti, 2012; Barnhart et al., 2010; Du et al., 2012; Loosley and Tang, 2012); a comparison of such mean field elasticity with more conventional bulk elasticity models can be found in Recho and Truskinovsky (2013). We remark that the coupling between the front and the rear of the fragment may also have an active origin resulting from different rates of polymerization and depolymerization at the extremities of the lamellipodium (Recho and Truskinovsky, 2013; Étienne et al., 2015). In other respects we neglect active protrusion (pushers). We also view adhesion as fully passive.

Despite the unavoidable oversimplifications associated with these assumptions, we show that our model reproduces quantitatively the motility initiation pattern in fish *keratocytes* and reveals a crucial role played in cell motility by the *nonlocal* feedback between the mechanics and the transport of active agents. It also provides compelling evidence that both, the *initiation* of motility and its *arrest*, may be fully controlled by the average contractility of motor proteins.

More precisely, we show that the increase of contractility beyond a well defined threshold leads to a bifurcation from a static symmetric solution of the governing system of equations (of Keller–Segel type) to an asymmetric traveling wave (TW) solution corresponding to steadily moving cells. While several TW regimes may be available at the same value of parameters, we show that stable TW solutions localize motors at the trailing edge of the cell in agreement with observations

(Verkhovsky et al., 1999; Csucs et al., 2007; Lombardi et al., 2007; Yam et al., 2007; Vicente-Manzanares et al., 2009; Poincloux et al., 2011). Moreover, we show that if adhesion with the extra-cellular substrate is sufficiently low, the increase of motor-induced contraction may induce transition from the steady state TW solution back to a static solution. This re-symmetrization transition, leading to the motility arrest, can be directly associated with the behavior of keratocytes prior to cell division and our model shows that such re-entrant behavior can be ensured by ‘pullers’ without any engagement of either active protrusion or liquid crystal elasticity.

The paper is organized as follows. In Section 2, we present a discrete “model of a model” which conveys the main ideas of our approach in the simplest form. In Section 3, we develop a continuum analogue of the discrete model, study its mathematical structure and pose the problem of finding the whole set of TW solutions incorporating both static and motile regimes. In Section 4, all static solutions of the TW problem are found analytically. In Section 5, we study the fine structure of multiple bifurcations producing motile solutions from the static ones and identify parametric regimes when these bifurcations become re-entrant. In Section 6, we investigate numerically the initial value problem which allows us to qualify some of the motile TW solutions as attractors. The reconstruction of the background turnover of actin, which takes place in our model without active protrusion at the leading edge, is discussed in Section 7. In Section 8, we demonstrate that our model can quantitatively match the experiments carried on keratocytes. The last section highlights our main conclusions and mentions some of the unsolved problems; three appendices contain material of technical nature.

Some of the results of this paper have been previously announced in two pre-publications (Recho et al., 2013, 2014) but without any details. In addition to providing a necessary background for Recho et al. (2013, 2014), here we develop a new discrete model, investigate the nonlocal nature of the coupling between mechanics and diffusion of active agents, give a thorough analysis of the static regimes, study the bifurcation points by using the Lyapunov–Schmidt reduction technique, investigate the non-steady problem numerically, generalize the model to account for nonlinear dependence of contractile stress on motor concentration and provide a detailed quantitative comparison of the model with experiment.

2. The discrete model

Our point of departure is a conceptual discrete model elucidating the mechanism of contraction-driven crawling and emphasizing the role of symmetry breaking in achieving the state of steady self-propulsion. This “model of a model” allows us to clarify the role of different components of the contraction-dominated motility machinery and link the proposed mechanism with the previous work on optimization of the crawling stroke irrespective of the underlying microscopic processes (e.g. DeSimone and Tatone, 2012; Noselli et al., 2014). It does not, however, address directly the main issues of motility initiation and motility arrest that require more elaborate constructions.

Recall that in crawling cells, the ‘motor part’ containing contracting cytoskeleton (lamellipodium) is a thin active layer located close to the leading edge of the cell, see Fig. 1. We assume that all mechanical action originates in lamellipodium and that from the mechanical viewpoint the rest of the cell, including the nucleus, can be interpreted as cargo. The main task will be to develop a model of freely moving lamellipodium which we schematize as a segment of active gel in viscous contact with a rigid background. The actin network inside the gel is contracted by myosin motors which leads to an internal flow opposed by the viscous interaction with the background. The unidirectional motion in a layer adjacent to the background that ultimately propels the cell is a result of the asymmetry of contraction.

A toy model elucidating this point involves three rigid blocks of size l_b placed in a frictional contact with a rigid support, characterized by the viscous drag coefficient ξ . The neighboring blocks are connected by *active pullers* (force dipoles) exerting contractile forces. The essential long range interactions representing global volume constraint (due to passive elastic structures and osmotic effects, see Section 3) are modeled by a linear spring with stiffness k connecting the first and the last block. To regularize the problem we place in parallel with contractile elements additional *dashpots* characterized by the viscosity coefficient η . In the absence of inertia, we can then write the force balance equations in the form

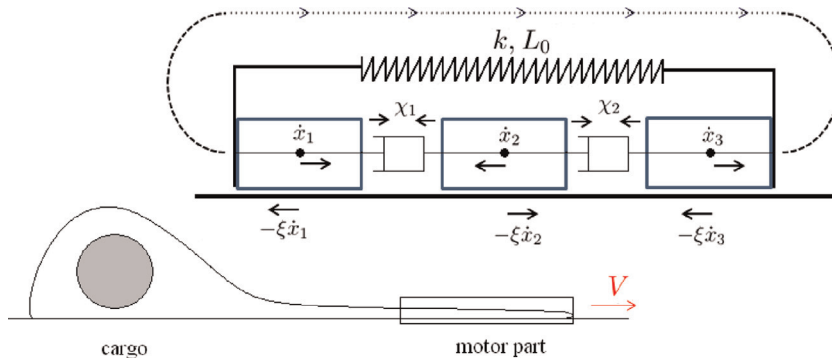


Fig. 1. Conceptual discrete model of the motility mechanism in a crawling keratocyte cell.

$$\begin{aligned}
-l_b \xi \dot{x}_1 + k \frac{x_3 - x_1 - L_0}{L_0} + \chi_1 - \eta \frac{\dot{x}_1 - \dot{x}_2}{l_b} &= 0 \\
-l_b \xi \dot{x}_2 - \chi_1 + \chi_2 - \eta \frac{\dot{x}_2 - \dot{x}_1}{l_b} - \eta \frac{\dot{x}_2 - \dot{x}_3}{l_b} &= 0 \\
-l_b \xi \dot{x}_3 - k \frac{x_3 - x_1 - L_0}{L_0} - \chi_2 - \eta \frac{\dot{x}_3 - \dot{x}_2}{l_b} &= 0,
\end{aligned} \tag{1}$$

where $x_1(t)$, $x_2(t)$, $x_3(t)$ are the current positions of the blocks and L_0 is the reference length of a linear spring. This spring describes the membrane-cortex ‘bag’ around the lamellipodium allowing the inhomogeneous contraction to be transformed into a protruding force. We assume that polarization has already taken place and therefore the contractile force dipoles $\chi_1 \geq 0$ and $\chi_2 \geq 0$ acting between the two pairs of blocks are not the same $\chi_1 \neq \chi_2$. The polarization itself requires additional constructs and will be addressed later.

System (1) can be rewritten as three decoupled equations for the length of our active segment $L(t) = x_3(t) - x_1(t)$, its geometric center $G(t) = (x_3(t) + x_1(t))/2$ and the position of a central block $x_2(t)$ representing the internal flow:

$$\begin{aligned}
-l_b \xi (1 + l_0^2/l_b^2) \dot{L} &= \chi_1 + \chi_2 + 2k(L/L_0 - 1) \\
2l_b \xi (1 + 3l_0^2/l_b^2) \dot{G} &= \chi_1 - \chi_2 \\
-l_b \xi (1 + 3l_0^2/l_b^2) \dot{x}_2 &= \chi_1 - \chi_2
\end{aligned} \tag{2}$$

where $l_0 = \sqrt{\eta/\xi}$ is the hydrodynamic length scale which will ultimately play the role of a regularizing parameter. The first equation shows that the length is converging to a steady state value:

$$L_\infty = L_0[1 - (\chi_1 + \chi_2)/(2k)].$$

Notice that in order to avoid the collapse of the layer due to contraction, it is necessary to ensure that the spring has sufficiently large stiffness $k > (\chi_1 + \chi_2)/2$. We also observe that independently of the value of the evolving length $L(t)$, the velocity of the geometrical center of our train of blocks V is always the same

$$V = \dot{G} = \frac{\chi_1 - \chi_2}{2l_b \xi (1 + 3l_0^2/l_b^2)}. \tag{3}$$

One can see that the system can move as a whole only if $\chi_1 \neq \chi_2$, which emphasizes the crucial role for motility of the *polarization* and the ensuing inhomogeneity of contraction.

We observe that the middle block moves in the direction opposite to the motion of the center of the system with a constant velocity $\dot{x}_2 = -2V$. Therefore, it takes a finite time $\sim L_\infty/(3V)$ for the central block to collide with the block at the rear. After this time, system (1) formally collapses and additional assumptions are needed to extend the dynamics beyond the collision point. The origin of the problem is our focus on the layer adjacent to the rigid background and the neglect of the global flow of actin.

To make the model more adequate we have to take into consideration that while the flow of F-actin (polymerized or filamentous actin) is continuous along the contact surface, the cytoskeletal network disintegrates into G-actin (unpolymerized monomers) at the trailing edge and reintegrates from the available G-actin at the leading edge. The polymerization induced depletion of G-actin at the leading edge is compensated by the diffusive counter-flow of actin monomers from the back of the cell to its front. This counter-flow cannot be described directly in the 1D setting.

It can be modeled, however, in an indirect way by mass and momentum preserving periodic boundary conditions allowing F-actin to disappear at the rear and reappear in the front. This situation is rather typical for continuum mechanics where unresolved spatial scales are often replaced by balance-law-preserving jump/singularity conditions as in the case of shock waves, crack tips and boundary layers.

More specifically, to account for global circulation (turnover) of the cytoskeleton in a one dimensional setting, we assume that there is a singular source of actin at the front of the cell that is compensated by the equivalent singular mass sink of actin at the rear of the cell. This assumption allows us to close the treadmilling cycle, even though the details of the discontinuous part of the cycle, involving both the polymerization reaction and the diffusive transport of monomers, are not explicitly resolved in the model. We essentially postulate that there is a pool of G-actin which is replenished as fast as it is depleted and that the resulting reverse flow of actin is synchronous with the direct flow. Under these assumptions the reverse flow is viewed as passive and is assumed to be driven exclusively by inhomogeneous contraction. In particular, we neglect active propulsion on free boundaries due to growth and lessening of the network.

We describe these processes in our *toy model* by assuming the possibility of creation and destruction of the blocks. Our goal is to account for the fact that actin polymerizes at the leading of the cell (where blocks are assembled) and depolymerizes at the trailing edge of the cell (where blocks are disassembled). We offer two interpretations of the underlying continuous process in terms of discrete blocks emphasizing different sides of such passive treadmilling.

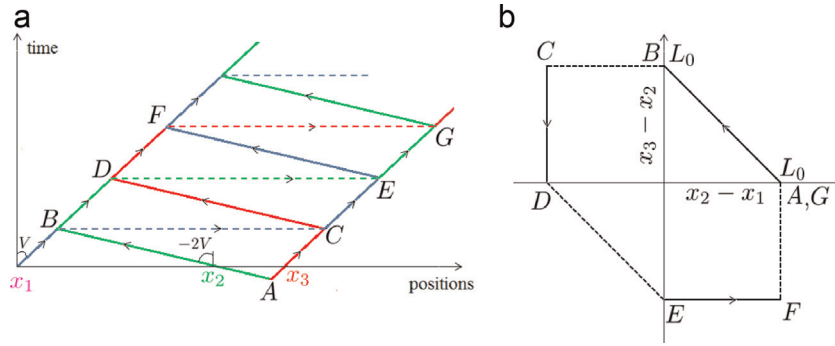


Fig. 2. (a) Schematic representation of the motion of individual particles (blocks) forming the motor part of a crawler in a steady state regime (three particle case). Trajectories in space time coordinates of the particles x_1 (magenta, OBCEF), x_2 (green, ABDEG) and x_3 (red, ACDGF); dashed lines show the jump parts of the crawling cycle. Continuous flows have to overcome friction while the jumps are assumed to be friction free. (b) A closed loop constituting one full stroke in the parameter space ($x_2 - x_1$, $x_3 - x_2$). The time of one full stroke (A to G) is $T_s = L_0/V$ and the distance traveled by the crawler per stroke is $VT_s = L_0$. (For interpretation of the references to color in this figure caption, the reader is referred to the web version of this paper.)

In a *first interpretation*, we assume that as a result of each collision a block at the rear is instantaneously removed from the chain and at the same time an identical block is added at the front. In other words, each (equilibrium) de-polymerization event at the rear is matched by an (equilibrium) polymerization event at the front. Here we implicitly refer to the existence of a stationary gradient of chemical potential of actin monomers and of a large pool of monomers ready to be added to the network at the front as soon as one of them is released at the rear. The ‘instantaneous’ reappearance of the disappearing blocks should be understood as a mean to model the overall continuity of the flow.

The structure of the resulting stroke in the t, x plane and in the $x_2 - x_1, x_3 - x_2$ plane is shown in Fig. 2. One can see that each block maintains its identity through the whole cycle and that its trajectory involves a succession of continuous segments described by (1) that are interrupted by instantaneous frictionless jumps from the rear to the front. Notice that in this interpretation the blocks can change order and the condition $x_1 < x_2 < x_3$ is not always satisfied. For instance, when the blocks x_1 and x_2 collide at point B, the block x_1 disappears at the back (point B) and reappears at the front (point C) ahead of the block x_3 . This jump mimics the frictionless part of the treadmilling cycle. Similarly, when the block x_3 collides with the block x_2 at point D, the latter reappears at the point E ahead of the block x_1 . This interpretation is attractive because it allows one to trace the trajectories of the blocks through subsequent treadmilling cycles. It is, however, a bit misleading because in reality the block that disappears at the back and the block which instantaneously reappears at the front are definitely not the same even though they are identical.

According to a *second interpretation*, illustrated in Fig. 3, the middle block is the only one to undergo cycling motion. As a result, the ordering $x_1 < x_2 < x_3$ is always preserved and the distances between the first two blocks $l_1 = x_2 - x_1$ and the last two blocks $l_2 = x_3 - x_2$ can be only positive. We can alternatively say that now the notations x_1, x_2, x_3 indicate positions only and can refer to different blocks in different times. In this interpretation, when the middle blocks hit the rear one, it is the middle block that gets recycled to the front while the rear one keeps moving continuously.

In coordinates (l_1, l_2) the cycle collapses on a single line, which is traveled continuously in one direction and discontinuously in the other direction, see Fig. 3(a). Notice that the internal parameters $l_1(t)$ and $l_2(t)$ undergo a periodic sequence of extensions and contractions which resemble the mechanism propelling the swimming sheet (Taylor, 1951) and its crawling analogue (DeSimone and Tatone, 2012). The main difference is that in our case the propulsion is achieved because of the asymmetry of friction forces acting in the different phases of the stroke. More specifically, we assume that during the continuous phase of the cycle the blocks move with friction (polymerized filaments experience effective drag transmitted by focal contacts), while during the discontinuous phase the dissipation (associated with reaction and diffusion)

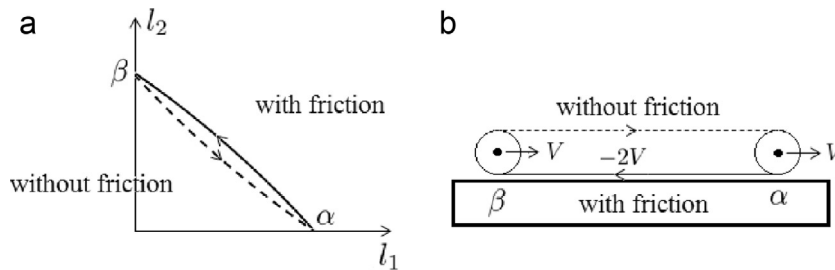


Fig. 3. Schematic representation of the continuous (α, β) and the jump (β, α) part of the crawling stroke. The zero area loop in l_1, l_2 plane illustrating the stroke is shown in (a). The loop is not symmetric because continuous flow have to overcome friction while the jumps are assumed to be friction free. The ‘tank thread’ analogy in (b) is not fully adequate because the ‘departing’ blocks at point β , that enter the pool of actin monomers, and the arriving blocks at point α , that are simultaneously taken from the same pool, are not the same.

can be neglected. The situation is remotely analogous to that of a rotating ‘tank tread’, see Fig. 3(b), even though in reality the disappearing block and the appearing block are not the same. This interpretation is closer to the physical picture where the points of the membrane (cortex) represented by two side blocks move with a constant speed ensuring that the cell maintains its length. We reiterate that both discrete interpretations are schematic and will be backed later in the paper by an appropriate continuum modeling.

Since the obtained expression for velocity (3) remains finite in the limit $l_0/l_b \rightarrow 0$ it appears that the dashpots play a redundant role in this model and can be dropped. To illustrate the role of the dashpots we now consider the case of N coupled blocks. Then, the force balance for the central blocks $j \in [2, N-1]$ reads

$$-l_b \xi \dot{x}_j - \chi_{j-1} + \chi_j - \eta \frac{\dot{x}_j - \dot{x}_{j-1}}{l_b} - \eta \frac{\dot{x}_j - \dot{x}_{j+1}}{l_b} = 0.$$

This system of equations can be written in the matrix form,

$$\mathbf{T}\dot{\mathbf{x}} = \mathbf{b}, \quad (4)$$

where we denoted by $\dot{\mathbf{x}}$ the unknown vector $\dot{x}_1, \dots, \dot{x}_N$. The tri-diagonal matrix

$$\mathbf{T} = \begin{bmatrix} -(2 + \frac{l_b^2}{l_0^2}) & 1 & 0 & 0 & 0 \\ 1 & -(2 + \frac{l_b^2}{l_0^2}) & 1 & 0 & 0 \\ 0 & \ddots & \ddots & \ddots & 0 \\ 0 & 0 & 1 & -(2 + \frac{l_b^2}{l_0^2}) & 1 \\ 0 & 0 & 0 & 1 & -(2 + \frac{l_b^2}{l_0^2}) \end{bmatrix}$$

describes the viscous coupling and frictional interaction with the background while the vector

$$\mathbf{b} = \frac{l_b}{\xi l_0^2} \begin{bmatrix} -\chi_1 + \sigma_0 - \frac{\xi l_0^2}{l_b} \dot{x}_1 \\ \chi_1 - \chi_2 \\ \vdots \\ \chi_{N-2} - \chi_{N-1} \\ \chi_{N-1} - \sigma_0 - \frac{\xi l_0^2}{l_b} \dot{x}_N \end{bmatrix}$$

with $\sigma_0 = -k(\chi_N - \chi_1 - L_0)/L_0$ carries the information about the active forcing, the mean field type elasticity and the boundary layer effects. To find the solution $\dot{\mathbf{x}}$, we need to invert the matrix \mathbf{T} and then solve a system of two coupled linear equations $\dot{x}_1 = (\mathbf{R} \mathbf{b})_1$ and $\dot{x}_N = (\mathbf{R} \mathbf{b})_N$ where $\mathbf{R} = \mathbf{T}^{-1}$. The components of the matrix \mathbf{R} can be found explicitly (Meurant, 1992)

$$R_{i,j} = \frac{\cosh((N+1-j-i)\lambda) - \cosh((N+1-|j-i|)\lambda)}{2 \sinh(\lambda) \sinh((N+1)\lambda)},$$

where $\lambda = \text{arccosh}(1 + l_b^2/(2l_0^2))$. Knowing the ‘velocity field’, we can now compute the steady state value of the length

$$L_\infty = L_0 \left(1 - \frac{\sum_{j=1}^{N-1} \cosh(\lambda(j - N/2)) \chi_j}{\sum_{j=1}^{N-1} \cosh(\lambda(j - N/2)) k} \right).$$

From this formula we see again that a finite stiffness is necessary to prevent the collapse of the system under the action of contractile stresses: assuming for instance that $\chi_i = \bar{\chi}$ we obtain the low bound for the admissible elasticity modulus $k > \bar{\chi}$.

The steady velocity $V = (\dot{x}_N + \dot{x}_1)/2$ of the geometrical center of the system can be also computed explicitly

$$V = - \frac{l_b \sum_{j=1}^{N-1} \sinh(\lambda(j - N/2)) \chi_j}{2\eta \sinh(\lambda N/2)}.$$

When N is even, by denoting $M = N/2$, we can rewrite this expression in the form

$$V = - \frac{l_b \sum_{j=1}^{M-1} \sinh(j\lambda) (\chi_{M+j} - \chi_{M-j})}{2\eta \sinh(\lambda M)}$$

from where it is clear that (as in the case of three blocks) the symmetry of the vector χ with respect to the center must be broken for the system to be able to self-propel.

If we now formally drop the dashpots by assuming that $l_0 = 0$ we obtain similar expressions for the velocity and for the steady state length as in the three block ($N=3$) case

$$V = \frac{\chi_{N-1} - \chi_1}{2\xi l_b}, \quad L_\infty = L_0 \left(1 - \frac{\chi_1 + \chi_{N-1}}{2k} \right). \quad (5)$$

The reason behind this similarity is that, in this limit, the ‘flow’ fully localizes in the two boundary elements, the only ones present in the case $N=3$. More precisely, the solution of the discrete problem depends singularly on the ratio l_b^2/l_0^2 and becomes progressively more concentrated around the boundary elements as $l_b^2/l_0^2 \rightarrow \infty$. Such localization presents a certain analytical problem if we consider the continuum limit when $N \rightarrow \infty$ and $l_b \rightarrow 0$ while $Nl_b \rightarrow L$, where L is the continuum length of the self-propelling segment. Indeed, in this limit the size of boundary layers tends to zero and the discrete solution converges to a distribution. The viscosity, introducing a length scale l_0 , is thus needed to preserve the regularity of solutions in the continuum limit.

Observe also that the limits $l_0 \rightarrow 0$ (dropping dashpots) and $l_b \rightarrow 0$ (continuum approximation) do not commute. For instance, if we choose in (5) the motor distribution with all $\chi_i = 0$ except for one $\chi_2 = \chi^* > 0$ we obtain $V=0$ for any value of l_b , in particular, when $l_b \rightarrow 0$ we still have $V \rightarrow 0$. If instead we first perform the continuum limit while keeping l_0 finite we obtain

$$L_\infty = L_0 \left(1 - \frac{\int_0^{L_\infty} \cosh[(x - L_\infty/2)/l_0] \chi(x) dx}{2kl_0 \sinh[L_\infty/(2l_0)]} \right) \quad (6)$$

and

$$V = - \frac{\int_0^{L_\infty} \sinh[(x - L_\infty/2)/l_0] \chi(x) dx}{2\eta \sinh[L_\infty/(2l_0)]}. \quad (7)$$

If we now take a distribution of motors $\chi(x) = \chi^* \delta_0$ where δ_0 is the Dirac mass at $x=0$, which can be viewed as a continuum analog of the discrete distribution considered above, we obtain that $V = \chi^*/(2l_0^2 \xi)$. Then in the limit $l_0 \rightarrow 0$ we obtain that $V \rightarrow \infty$ which is in conflict with our previous assertion that $V=0$, obtained when the order of limits was reversed. Assume now that $l_b \sim N^{-1}$ and hence $l_b^2/l_0^2 \sim 1/(\eta N^2)$. One can see that the crossover scaling $\eta \sim N^{-2}$ separates the two non-commuting limiting regimes. For $l_b^2/l_0^2 \rightarrow \infty$ (which is a dimensionless version of $\eta \ll N^{-2}$) the internal flow localizes in the boundary layers whose thickness disappears when $\eta \rightarrow 0$; when we dropped the dashpots in the three element model we could not detect this localization because the two boundary links were the only ones present in the system. In the other limit $l_b^2/l_0^2 \rightarrow 0$ (dimensionless version of $\eta \gg N^{-2}$) the viscosity dominates the dynamics and the internal flow becomes uniform.

In the next sections the formulas (6) and (7) will be obtained directly from the continuum model. We will also see more clearly how the introduction of the viscosity-related internal length scale and the associated nonlocality regularizes the continuum model which otherwise has only singular solutions.

3. The continuum model

We model the lamellipodium as a one dimensional continuum layer in frictional contact with a rigid background, see Fig. 4. Assuming that the drag is viscous and neglecting inertia we can write the force balance in the form

$$\partial_x \sigma = \xi v, \quad (8)$$

where $\sigma(x, t)$ is the axial stress and $v(x, t)$ is the velocity of the cytoskeleton (actin network). Eq. (8) is the continuous analog of the system (4) in the discrete problem.

As in the discrete model, we denoted by ξ the coefficient of viscous drag. Such representation of active adhesion is usual in the context of cell motility (Rubinstein et al., 2009; Larripa and Mogilner, 2006; Jülicher et al., 2007; Shao et al., 2010;

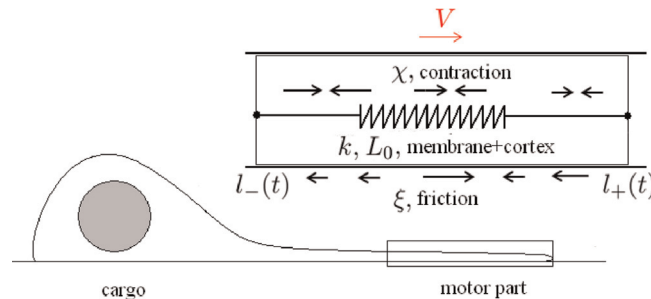


Fig. 4. Schematic representation of a continuum model simulating lamellipodial contraction-driven crawling.

Doubrovinski and Kruse, 2011; Hawkins et al., 2011). It implies that the time-averaged shear stress generated by constantly engaging and disengaging focal adhesions is proportional to the velocity of the retrograde flow, see Tawada and Sekimoto (1991) for a microscopic justification. There is evidence (both experimental Gardel et al., 2008, 2010; Mogilner, 2009; Bois et al., 2011; Schwarz and Gardel, 2012 and theoretical DiMilla et al., 1991; Mi et al., 2007) that this assumption describes the behavior of focal adhesions accurately only when the retrograde flow is sufficiently slow. The behavior of adhesion strength in the broader range of velocities is biphasic and since we neglect this effect, we potentially misrepresent sufficiently fast dynamics. Observe though that for both keratocytes and PtK1 cells the rate of lamellar actin retrograde flow varies from 5 to 30 nm s⁻¹ in usual experimental conditions (Schwarz and Gardel, 2012) and in this range a direct proportionality relationship between traction stress and actin retrograde flow has been confirmed experimentally (Gardel et al., 2008; Fournier et al., 2010; Barnhart et al., 2011). The characteristic velocity of the flow in our problem is 20 nm s⁻¹ which falls well into the aforementioned interval where the biphasic behavior can be neglected.

Following Kruse et al. (2006), Jülicher et al. (2007), Bois et al. (2011) and Howard et al. (2011), we assume that the cytoskeleton is a viscous gel with active pre-stress. We neglect the bulk elastic stresses that relax over a time scale of 1–10 s (Rubinstein et al., 2009; Wottawah et al., 2005; Kole et al., 2005; Panorchan et al., 2006; Mofrad, 2009; Recho and Truskinovsky, 2013) which is much shorter than characteristic time scale of motility experiments (hours). We can then describe the constitutive behavior of the gel in the form

$$\sigma = \eta \partial_x v + \chi c, \quad (9)$$

where η is the bulk viscosity, $c(x, t)$ is the mass concentration of motors and $\chi > 0$ is a contractile pre-stress (per motor) representing internal activity. The constitutive relation (9) generalizes the parallel bundling of dashpots and contractile units in the discrete model. The important new element is that the strength of the contractile elements may now vary in both space and time.

In the discrete model the concentration of motors c was given as a function of x . To obtain a more self-consistent description we assume that the function $c(x, t)$ satisfies a convection–diffusion equation (Rubinstein et al., 2009; Bois et al., 2011; Barnhart et al., 2011; Wolgemuth et al., 2011; Hawkins et al., 2011)

$$\partial_t c + \partial_x(cv) = D \partial_{xx} c, \quad (10)$$

where D is the diffusion coefficient. Behind (10) is the assumption that myosin motors, actively cross-linking the actin network, are advected by the network flow and can also diffuse which accounts for thermal fluctuations.

To justify this model, consider a simple mixture model with two species representing attached and detached motors. The attached motors are advecting with the velocity of actin filaments and can detach. The detached motors are freely diffusing, and can also attach. Suppose that the attachment–detachment process can be described by a first order kinetic equation. Then the system of equations governing the evolution of the concentrations of attached c_a and detached c_d motors can be written as

$$\begin{aligned} \partial_t c_a + \partial_x(c_a v) &= k_{\text{on}} c_d - k_{\text{off}} c_a \\ \partial_t c_d - \tilde{D} \partial_{xx} c_d &= k_{\text{off}} c_a - k_{\text{on}} c_d \end{aligned}$$

where k_{on} and k_{off} are the chemical rates of attachment and detachment and \tilde{D} is the diffusion coefficient of detached motors in the cytosol. Now suppose that the attachment–detachment process is chemically equilibrated and hence $c_a/c_d = K$, where $K = k_{\text{on}}/k_{\text{off}}$ is the reaction constant. Then for the attached motors performing contraction we obtain

$$\frac{K+1}{K} \partial_t c_a + \partial_x(c_a v) - \frac{\tilde{D}}{K} \partial_{xx} c_a = 0.$$

Our Eq. (10) is obtained in the limit $K \rightarrow \infty$ (fast attachment) and $\tilde{D}/K \rightarrow D$ (fast diffusion).

Denote by $L_-(t)$ and $L_+(t)$ the rear and front boundaries of our gel segment. To account for cortex/membrane elasticity we assume, as in the discrete model, that the boundaries are linked through a linear spring (Barnhart et al., 2010; Du et al., 2012; Loosley and Tang, 2012; Recho and Truskinovsky, 2013). This assumption affects the values of the stress in the moving points $L_-(t)$ and $L_+(t)$:

$$\sigma(L_{\pm}(t), t) = -k(L(t) - L_0)/L_0.$$

Here $L(t) = L_+(t) - L_-(t)$ is the length of the segment, k is the effective elastic stiffness and L_0 is the reference length. As we have seen in the discrete model, the presence of an elastic interaction plays a crucial role in preventing the collapse of the segment due to contractile activity of motors.

Our next assumption is that the external boundaries of the self-propelling segment are isolated in the sense that they move with the internal flow $\dot{L}_{\pm} = v(L_{\pm})$. We imply here that the addition and deletion of F-actin particles inserted at the front and taken away at the rear does not contribute to propulsion. We also impose a zero exterior flux condition for motors $\partial_x c(L_{\pm}(t), t) = 0$ ensuring that the average concentration of motors

$$c_0 = \frac{1}{L_0} \int_{L_-}^{L_+} c(x, t) dx \quad (11)$$

is conserved. To complete the setting of the problem we need to impose the initial conditions $l_{\pm}(0) = l_{\pm}^0$ and $c(x, 0) = c^0(x)$.

Our assumption that the bulk stiffness of the cytoskeleton is equal to zero (also known as the infinite compressibility assumption [Jülicher et al., 2007](#); [Rubinstein et al., 2009](#)) allowed us to uncouple the force balance problem (which becomes statically determinate) from the mass transport problem. Then by solving the main system of governing equations (8)–(11) we can obtain the velocity field and the concentration of motors. To recover the mass distribution of the cytoskeleton we need to solve a decoupled mass balance equation with a kinematically prescribed velocity field ([Recho and Truskinovsky, 2013](#); [Recho et al., 2013](#)).

Indeed, suppose that by solving the system (8)–(11) we found the velocity field $v(x, t)$. This means that we also know the trajectories of the free boundaries $l_{-}(t)$ and $l_{+}(t)$. To find the mass density of actin $\rho(x, t)$ in the gel, we need to solve the mass balance equation

$$\partial_t \rho + \partial_x(\rho v) = 0 \quad (12)$$

with initial condition $\rho(x, 0) = \rho_0(x)$. Here we neglected the diffusion of actin which is weak comparing to the diffusion of myosin. Now, since both the leading and the trailing edges of the moving lamellipodium coincide with the trajectories of particles, the total mass M is conserved

$$M = \int_{l_{-}(t)}^{l_{+}(t)} \rho(x, t) dx.$$

To address the problem of continuous circulation and to close the cycle of the cytoskeleton flow we need to interpret the points of density singularities as actin (mass) sources and sinks. In [Section 7](#) we show how the solutions can be regularized if we cut out small regularization domains around the sources and sinks and appropriately reconnect the incoming and the outgoing flows of matter.

Dimensionless problem: If we now normalize length by L_0 , time by L_0^2/D , stress by k , concentration by c_0 and density by M/L_0 , we can rewrite the main system of equations in dimensionless form (without changing the notations)

$$\begin{aligned} -\mathcal{Z} \partial_{xx} \sigma + \sigma &= \mathcal{P} c, \\ \partial_t c + \mathcal{K} \partial_x(c \partial_x \sigma) &= \partial_{xx} c. \end{aligned} \quad (13)$$

Here we introduced three main dimensionless constants of the problem:

$$\mathcal{Z} = \eta/(\xi L_0^2),$$

the ratio of viscous and elastic length scales;

$$\mathcal{K} = k/(\xi D),$$

the ratio of stiffness induced agglomeration over diffusion and finally

$$\mathcal{P} = c_0 \chi / k,$$

the dimensionless measure of motor contractility. One can discern in (13) the structure of the Keller–Segel system from the theory of chemotaxis (e.g. [Perthame, 2012](#)). The role of the distributed chemical attractant is played in our case by the stress field σ whose gradient is the driving force affecting the ‘colony’ of myosin motors.

The main mathematical difference between our formulation and the standard chemotaxis problem is that we have free boundaries. Using dimensionless variables we can rewrite the boundary conditions in the form

$$\dot{l}_{\pm}(t) = \mathcal{K} \partial_x \sigma(l_{\pm}(t), t), \quad (14)$$

$$\sigma(l_{\pm}(t), t) = -(L(t) - 1), \quad (15)$$

$$\partial_x c(l_{\pm}(t), t) = 0. \quad (16)$$

The integral constraint (11) reduces to

$$\int_{l_{-}}^{l_{+}} c(x, t) dx = 1. \quad (17)$$

In dimensionless variables the mass balance equation (12) takes the form

$$\partial_t \rho + \mathcal{K} \partial_x(\rho \partial_x \sigma) = 0,$$

and the total mass gets normalized

$$\int_{l_{-}(t)}^{l_{+}(t)} \rho(x, t) dx = 1. \quad (18)$$

Non-local reformulation: Since the first of Eq. (13) is linear, it can be solved explicitly for σ

$$\sigma(x, t) = -\frac{(L-1) \cosh[(G-x)/\sqrt{\mathcal{Z}}]}{\cosh[L/(2\sqrt{\mathcal{Z}})]} + \frac{\mathcal{P}}{\sqrt{\mathcal{Z}}} \int_{L_-}^{L_+} \Psi(x, y) c(y) dy, \quad (19)$$

where

$$\Psi(x, y) = \frac{\sinh[(l_+ - x)/\sqrt{\mathcal{Z}}] \sinh[(y - L_-)/\sqrt{\mathcal{Z}}]}{\sinh(L/\sqrt{\mathcal{Z}})} - H(y - x) \sinh[(y - x)/\sqrt{\mathcal{Z}}].$$

We introduced the notations: $H(x)$ – the Heaviside function and $G(t) = [L_-(t) + L_+(t)]/2$ is the position of the geometric center of the moving fragment. By eliminating σ from (13)₂ we obtain a single non-local partial differential equation with quadratic non-linearity for $c(x, t)$

$$\partial_t c(x, t) - \mathcal{K}(L-1) \partial_x [\theta(x) c(x, t)] + \frac{\mathcal{PK}}{\sqrt{\mathcal{Z}}} \partial_x \left(\int_{L_-}^{L_+} \varphi(x, y) c(y, t) c(x, t) dy \right) = \partial_{xx} c(x, t), \quad (20)$$

where the auxiliary velocity field

$$\theta(x) = \frac{\sinh[(x - G)/\sqrt{\mathcal{Z}}]}{\cosh[L/(2\sqrt{\mathcal{Z}})]}$$

describes advective flow induced by the elastic coupling between the rear and the front of the active segment. The feedback behind contraction-driven motility is contained in the kernel

$$\varphi(x, y) = -\frac{\cosh[(l_+ - x)/\sqrt{\mathcal{Z}}] \sinh[(y - L_-)/\sqrt{\mathcal{Z}}]}{\sinh(L/\sqrt{\mathcal{Z}})} + H(y - x) \cosh[(y - x)/\sqrt{\mathcal{Z}}],$$

which is due to viscosity-induced bulk interactions in the system and the effect of the boundaries. Notice that this kernel has the action/reaction symmetry $\varphi(x, y) = -\varphi(l_+ + L_- - x, l_+ + L_- - y)$ which is a fundamental constraint imposed by the balance of momentum (Kruse and Jülicher, 2003, 2000; Torres et al., 2010).

Inviscid limit: To distinguish the bulk mechanical interactions from the effects of the boundaries, we use the following asymptotic expansion (Ren and Truskinovsky, 2000):

$$\begin{aligned} \varphi_b(y - x) &= \lim_{L \rightarrow \infty} \varphi(x + G, y + G) \\ &= \frac{1}{2} \begin{cases} \exp(\frac{x - y}{\sqrt{\mathcal{Z}}}) & \text{if } x - y < 0 \\ -\exp(\frac{y - x}{\sqrt{\mathcal{Z}}}) & \text{if } x - y > 0. \end{cases} \end{aligned} \quad (21)$$

In Fig. 5, we compare our viscosity induced interaction kernel with a long range kernel proposed in Kruse and Jülicher (2003, 2000) and Torres et al. (2010), as a model of steric interactions between actin filaments with half size l_s

$$\varphi_s(x - y) = \begin{cases} \frac{1}{2} \operatorname{sgn}(y - x) & \text{if } |x - y| \leq l_s \\ 0 & \text{if } |x - y| > l_s \end{cases} \quad (22)$$

The length l_s plays in Kruse and Jülicher (2003, 2000) and Torres et al. (2010), the same role as our viscous length $l_0 = \sqrt{\eta/\xi}$ represented in (21) by the dimensionless parameter \mathcal{Z} .

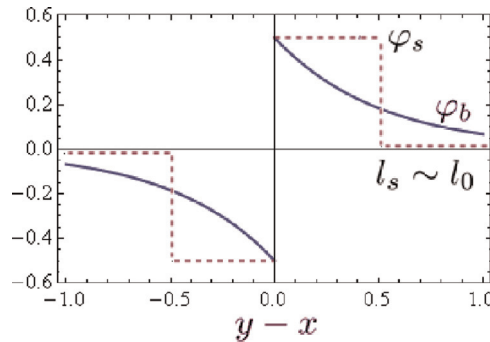


Fig. 5. Comparison of the bulk part of the viscosity induced interaction kernel φ_b (continuous line) with its mean field analog φ_s (dashed line) proposed in Kruse and Jülicher (2003).

Recall that in [Section 2](#) we anticipated a non-trivial limit in the continuum theory when the bulk viscosity η goes to zero. Now we see that when $\mathcal{Z} \rightarrow 0$ the kernel φ_b becomes singular and the nonlocality in the mechanical part of the model disappears. From [\(13\)](#) we also notice that parameter \mathcal{Z} enters as a coefficient in front of the highest derivative. Therefore, outside the boundary layers of size $\sim \sqrt{\mathcal{Z}}$ one can formally assume that $\sigma = \mathcal{P}c$ which makes the main dynamic equation [\(20\)](#) local

$$\partial_t c(x, t) + \mathcal{P} \mathcal{K} \partial_x (c(x, t) \partial_x c(x, t)) = \partial_{xx} c(x, t). \quad (23)$$

At small \mathcal{Z} the non-bulk contributions to the kernel $\varphi(x, y)$ will play a role only around the extremities of the moving segment and in the limit $\mathcal{Z} \rightarrow 0$ will affect only the boundary conditions.

By using a new variable $w = 1 - \mathcal{K} \mathcal{P} c$, we can rewrite Eq. [\(23\)](#) in the form

$$\partial_t w(x, t) + \partial_x (w \partial_x w(x, t)) = 0.$$

Here we recognize the porous flow equation which is, however, unusual because the field $w(x, t)$ may be sign-indefinite. In particular, in the regimes with $c > (\mathcal{K} \mathcal{P})^{-1}$ one can expect an uphill diffusion similar to that of spinodal decomposition. A systematic study of the inviscid case, requiring the knowledge of the boundary conditions in the limiting problem, will be done elsewhere.

Cell velocity: Using the boundary conditions [\(14\)](#) we find from [\(19\)](#) an explicit formula for the (time dependent) velocity of the center of our active segment (see also Eq. [\(7\)](#) in [Section 2](#))

$$\dot{G} = \frac{\mathcal{K} \mathcal{P}}{2\mathcal{Z}} \int_{L_-}^{L_+} \frac{\sinh\left(\frac{G-x}{\sqrt{\mathcal{Z}}}\right)}{\sinh\left(\frac{L}{2\sqrt{\mathcal{Z}}}\right)} c(x, t) dx. \quad (24)$$

Similarly we obtain an equation for the evolving length of the segment (see also Eq. [\(6\)](#) in [Section 2](#))

$$\dot{L} = -2 \frac{\mathcal{K}}{\sqrt{\mathcal{Z}}} (L-1) \tanh\left(\frac{L}{2\sqrt{\mathcal{Z}}}\right) - \frac{\mathcal{K} \mathcal{P}}{\mathcal{Z}} \int_{L_-}^{L_+} \frac{\cosh\left(\frac{G-x}{\sqrt{\mathcal{Z}}}\right)}{\cosh\left(\frac{L}{2\sqrt{\mathcal{Z}}}\right)} c(x, t) dx. \quad (25)$$

Notice that in [\(24\)](#) only the odd component of the function $c(x, t)$ (with respect to the moving center $G(t)$) contributes to the integral while in [\(25\)](#) only the even component matters. In particular, if the concentration of motors is an even function of x then $\dot{G} = 0$ and the segment does not move as a whole. This conclusion is a direct analog of Purcell's theorem ([Purcell, 1977](#)) in the case of a crawling body. Notice that for crawling the emphasis is made on spatial asymmetry which replaces the emphasis on temporal asymmetry in Purcell's interpretation of swimming.

From [\(24\)](#) we infer that the maximal velocity of the self-propelling segment is equal to $\mathcal{K} \mathcal{P} / (2\mathcal{Z})$. If we use the data from [Jülicher et al. \(2007\)](#), [Bois et al. \(2011\)](#), and [Howard et al. \(2011\)](#), we obtain the estimates $\chi c_0 \simeq 10^3$ Pa, $L_0 = 10 \mu\text{m}$ and $\eta = 3 \times 10^4$ Pa s. For the maximal velocity, this gives $\chi L_0 c_0 / (2\eta) \simeq 10 \mu\text{m/min}$ which is rather realistic in view of the data presented by [Jilkiné and Edelstein-Keshet \(2011\)](#) and [Schreiber et al. \(2010\)](#).

Traveling waves: Given our interest in the steady modes of cell motility, which are typical for keratocytes ([Barnhart et al., 2011](#)), we need to study the traveling wave (TW) solutions of the main system [\(13\)](#). To find such solutions we assume that the front and the rear of our segment travel with the same speed $\dot{L}_{\pm}(t) \equiv V$, ensuring the constancy of the length $L(t) \equiv L$, and that both the stress and the myosin concentration depend on x and t through a combination $u = (x - Vt)/L$ only. Using this ansatz we find that Eq. [\(13\)](#)₂ can be solved explicitly

$$c(u) = \frac{\exp[s(u) - VLu]}{L \int_0^1 \exp[s(u) - VLu] du}. \quad (26)$$

Here for convenience we introduced a new stress variable $s(u) = \mathcal{K}[\sigma(u) + (L-1)]$ which represents the inhomogeneous contribution to internal stress field due to active pre-stress. The system [\(13\)](#) reduces to the single nonlocal equation

$$-\frac{\mathcal{Z}}{L^2} s''(u) + s(u) - \mathcal{K}(L-1) = \mathcal{K} \mathcal{P} \frac{\exp[s(u) - LVu]}{L \int_0^1 \exp[s(u) - VLu] du}, \quad (27)$$

supplemented by the boundary conditions

$$s(0) = s(1) = 0 \quad \text{and} \quad s'(0) = s'(1) = LV. \quad (28)$$

The two 'additional' boundary conditions in [\(28\)](#) allow one to determine parameters V and L along with the function $s(u)$. After the problem [\(27\)](#), [\(28\)](#) is solved, the motor concentration profile can be found explicitly by using [\(26\)](#).

4. Static regimes

Initiation of motility is associated with a symmetry breaking instability of a static (non-motile) configuration. To identify non-motile configurations we need to find solutions of (27) with $V=0$. These solutions may still characterize the states with nontrivial active internal rearrangements of both actin and myosin. Static solutions with periodic boundary conditions were studied in Bois et al. (2011) and here we complement and extend their analysis.

If $V=0$, Eq. (27) simplifies considerably

$$-\frac{\mathcal{Z}}{L^2}s'' + s - \mathcal{K}(L-1) = \mathcal{K}\mathcal{P} \frac{\exp(s)}{L \int_0^1 \exp(s(u)) du}. \quad (29)$$

The nonlocal equation (29) was studied extensively in many domains of science from chemotaxis (Senba and Suzuki, 2000) to turbulence (Caglioti et al., 1992) and gauge theory (Struwe and Tarantello, 1998). In our case, this equation, where parameter L remains unknown, has to be solved with three boundary conditions $s'(0) = s(0) = s(1) = 0$ because the forth boundary condition $s'(1) = 0$ is satisfied automatically.

We begin with the study of the regular solutions of (29). Instead of \mathcal{K} and \mathcal{P} , it will be convenient to use another set of parameters $A := \mathcal{K}(L-1) \leq 0$ and $B := \mathcal{K}\mathcal{P}/(L \int_0^1 \exp(s(u)) du) \geq 0$. In terms of parameters (A, B) the problem (29) reads

$$-\frac{\mathcal{Z}}{L^2}s'' + s - A = B \exp(s) \quad \text{with } s'(0) = s(0) = s(1) = 0. \quad (30)$$

A trivial homogeneous solution of this problem $s(u) = 0$ exists when $A + B = 0$ which is equivalent in the $(\mathcal{P}, \mathcal{K})$ parametrization to $L = \hat{L}_\pm$ with,

$$\hat{L}_\pm = (1 \pm \sqrt{1 - 4\mathcal{P}})/2. \quad (31)$$

The sub-branches with longer and shorter lengths $\hat{L}_+(\mathcal{P})$ and $\hat{L}_-(\mathcal{P})$, respectively, that meet at point α where $\hat{L}_-(\mathcal{P}) = \hat{L}_+(\mathcal{P})$ are illustrated in Fig. 6.

To obtain nontrivial static solutions we multiply (30) by s' , integrate and use the boundary conditions to obtain the 'energy integral' $s'^2 = W(s)$, where

$$W(s) = \frac{L^2}{\mathcal{Z}}(s^2 - 2As - 2B(\exp(s) - 1)).$$

The general solution of this equation can be expressed as a quadrature, $u = \pm \int^{s(u)} W^{-1/2}(r) dr$ where we recall that u designates the normalized space variable. A detailed analysis of this equation is given in Appendix A, where different families of static solutions are identified as S_m^\pm and $(S_m^\pm)'$. The index \pm specifies the \hat{L}_\pm trivial branch from which a particular solution bifurcates: the associated lengths \hat{L}_\pm are defined in (31). The integer valued index m corresponds to the number of spikes in the configuration $s(u)$. The prime differentiates between two subfamilies belonging to the same bifurcated branch with primed subfamily having a length L larger than in the trivial configuration and non-primed subfamily having the length L smaller than in the trivial configuration. Fig. 22 illustrates the families S_1^+ and S_2^+ . For each family we plot the length of the fragment L as a function of one of the controlling parameters, in Fig. 7.

In addition to regular solutions described above Eq. (29) has measure-valued solutions corresponding to collapsed cells with length $\hat{L}_0 = 0$. First of all, as we see in Fig. 6, $\hat{L}_-(\mathcal{P}) \rightarrow 0$ when $\mathcal{P} \rightarrow 0$ (point α') and the limiting distribution of motors is concentrated on an infinitely small domain. To characterize the asymptotic structure of the singular solutions we suppose

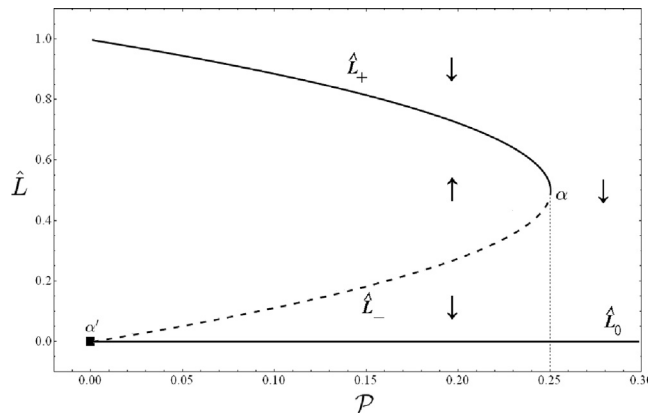


Fig. 6. Three families of trivial static solutions \hat{L}_+ , \hat{L}_- and \hat{L}_0 parameterized by \mathcal{P} . Solid lines show stable branches while dotted lines correspond to unstable branches. Arrows depict the basin of attraction of each branch (see Section 6).

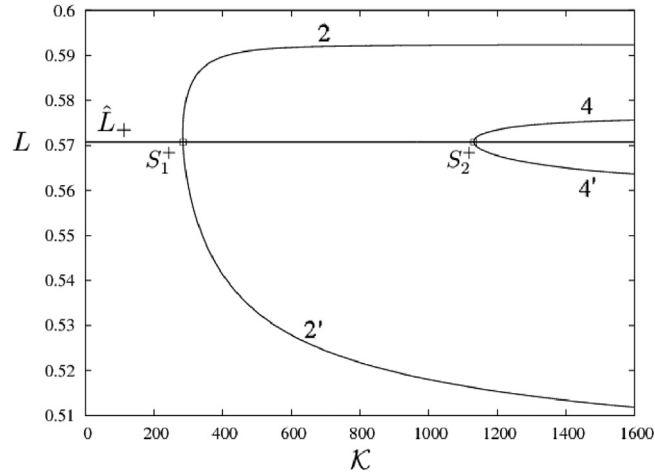


Fig. 7. Bifurcation diagram for the \hat{L}_+ branch at fixed $\mathcal{P} = 0.245$ and $\mathcal{Z} = 1$. See also Fig. 9(a).

that $L \ll 1$ and that the maximum of s is of order L . Then, by ignoring high order terms, we deduce from (29) a simplified boundary value problem

$$-s'' \approx \mathcal{K}PL/(\mathcal{Z} \int_0^1 [1 + s(u)] du) \quad \text{with } s'(0) = s(0) = s(1) = 0. \quad (32)$$

Then $s(u) \approx \mathcal{K}PLu(1-u)/(2\mathcal{Z})$ and the remaining boundary condition $s'(0) = 0$ is automatically satisfied in the limit $L \rightarrow 0$. We can then conclude that the singular solutions are of the form

$$s(x) = \lim_{L \rightarrow 0} Lf(x/L)$$

where $f(u) = \mathcal{K}Pu(1-u)/(2\mathcal{Z})$. Singular solutions of this type can be implicated in the description of cell splitting in a cortical geometry (Turlier et al., 2014); they are also known in other fields where stationary states are described by Eq. (29) (Caglioti et al., 1992; Chen and Lin, 2001; Ohtsuka, 2002; Gladiali et al., 2012). The presence of such solutions is a sign that in a properly augmented theory, accounting for a vanishing internal length, one can expect localization with active contraction balanced by a regularization mechanism, which may be, for instance, active treadmilling (Recho and Truskinovsky, 2013). Our numerical solutions of a non-steady problem, which are naturally regularized because of the finite mesh size (see Section 6), show that the almost singular solutions of the type described above are indeed attractors for initial data with $L < \hat{L}_-$ when $\mathcal{P} < 1/4$. Moreover, numerical experiments suggest that they are the only attractors for $\mathcal{P} > 1/4$. This means that even in the presence of a cortex-type spring, an active segment fragment necessarily collapses after the contractility parameter reaches the threshold $\mathcal{P}_{\max} = 1/4$.

5. Re-entrant bifurcations

We first show that motile branches with $V \neq 0$ can bifurcate only from trivial static solutions with $s(u) = 0$, $V = 0$ and $L = \hat{L}_\pm$. For $V \neq 0$ equation, multiplying (27) by $s' - VL$, we find the relation

$$1 - \exp(-LV) = LV \int_0^1 \exp[s(u) - VLu] du. \quad (33)$$

Then in the limit $V \rightarrow 0$ we obtain that $\int_0^1 \exp(s(u)) du = 1$. Since static solutions $s(u)$ must be necessarily sign definite, see Appendix A, Eq. (33) implies that the corresponding static solution can only be trivial $s(u) = 0$. As we have seen in Fig. 6, there are two non-singular families of trivial solutions: one with longer (\hat{L}_+ family) and the other with shorter (\hat{L}_- family) lengths.

Bifurcation points: To find the bifurcation points along the trivial branch ($s = 0$, $V = 0$, $L = \hat{L}_\pm(\mathcal{P})$), we introduce infinitesimal perturbations $\delta s(u)$, δV , δL and linearize (27) together with boundary conditions (28). We obtain the boundary value problem

$$\delta s'' - \omega^2 \delta s = \frac{\mathcal{Z}\omega^2 - \hat{L}^2}{\hat{L}^2(\hat{L} - 1)} \left(\mathcal{Z} \frac{2\hat{L} - 1}{\hat{L}} \omega^2 \delta L + \frac{\hat{L}^3(\hat{L} - 1)}{2} (2u - 1) \delta V \right), \quad (34)$$

$$\delta s(0) = \delta s(1) = 0, \quad \delta s'(0) = \delta s'(1) = \hat{L} \delta V. \quad (35)$$

Here we introduced the notation

$$\omega^2 = (\hat{L}^2 - \mathcal{K}\mathcal{P}\hat{L})/\mathcal{Z}. \quad (36)$$

Since $\omega=0$ at the trivial branch $\delta s = \delta V = \delta L = 0$, we can assume that $\omega \neq 0$. The general solution of the problem (34), (35) can be written explicitly

$$\delta s(u) = C_1 \sinh(-\omega u) + C_2 \cosh(-\omega u) - \frac{\mathcal{Z}\omega^2 - \hat{L}^2}{\omega^2 \hat{L}^2 (\hat{L} - 1)} \left(\mathcal{Z} \frac{2\hat{L} - 1}{\hat{L}} \omega^2 \delta L + \frac{\hat{L}^3 (\hat{L} - 1)}{2} (2u - 1) \delta V \right). \quad (37)$$

From boundary conditions, non-trivial solutions branch from the trivial ones if the matrix

$$\begin{pmatrix} 1 & 0 & \frac{(2\hat{L} - 1)(\hat{L}^2 - \omega^2 \mathcal{Z})}{(\hat{L} - 1)\hat{L}^3} & \frac{1}{2} \hat{L} \left(\frac{\hat{L}^2}{\omega^2 \mathcal{Z}} - 1 \right) \\ \cosh(\omega) & \sinh(\omega) & \frac{(2\hat{L} - 1)(\hat{L}^2 - \omega^2 \mathcal{Z})}{(\hat{L} - 1)\hat{L}^3} & \frac{1}{2} \hat{L} \left(1 - \frac{\hat{L}^2}{\omega^2 \mathcal{Z}} \right) \\ 0 & \omega & 0 & -\frac{\hat{L}^3}{\omega^2 \mathcal{Z}} \\ \omega \sinh(\omega) & \omega \cosh(\omega) & 0 & -\frac{\hat{L}^3}{\omega^2 \mathcal{Z}} \end{pmatrix} \quad (38)$$

has a zero determinant. This gives a transcendental equation for ω

$$2\hat{L}[\cosh(\omega) - 1] - \mathcal{K}\mathcal{P}\omega \sinh(\omega) = 0. \quad (39)$$

The detailed analysis of this equation is presented in Appendix B. The full locus of bifurcation points in the $(\mathcal{K}, \mathcal{P})$ plane is shown in Fig. 8. The lines of bifurcation points $+$ and $-$ originating on the trivial sub-branches \hat{L}_+ and \hat{L}_- smoothly connect at $\mathcal{P} = 1/4$, see Fig. 6. When parameter \mathcal{P} is held constant while \mathcal{K} is changing each family D_i and S_i in Fig. 8 is represented

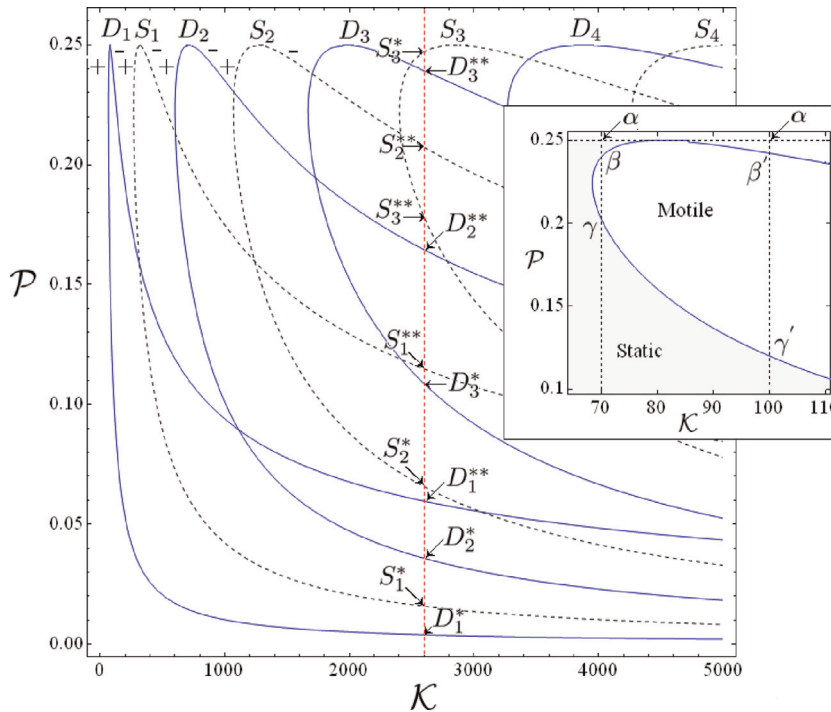


Fig. 8. Locus of the bifurcation points in the $(\mathcal{K}, \mathcal{P})$ plane for $\mathcal{Z} = 1$. Insert shows a zoom on the D_1 branch around the turning point at $\mathcal{P} = 1/4$ where \hat{L}_+ and \hat{L}_- branches meet. The detailed bifurcation diagrams for $\mathcal{P} = 0.245$ and $\mathcal{K} = 70$ and 100 are shown in Figs. 9(a) and 10 from where the meaning of labels $\beta, \gamma, \beta', \gamma'$ becomes clear. The bifurcation points related to the cut $\mathcal{K} = 2600$ (red dashed line) in the (\mathcal{P}, L) space are shown in Fig. 6. (For interpretation of the references to color in this figure caption, the reader is referred to the web version of this paper.)

by two points. For solutions bifurcating from the trivial branch \hat{L}_+ , we have $\mathcal{K}_+ = (\hat{L}_+^2 - \mathcal{Z}\omega^2)/(\mathcal{P}\hat{L}_+)$, which gives points D_1^+ , S_1^+ , D_2^+ , S_2^+ , ... and for the branch \hat{L}_- , we have $\mathcal{K}_- = (\hat{L}_-^2 - \mathcal{Z}\omega^2)/(\mathcal{P}\hat{L}_-)$ which gives points D_1^- , S_1^- , D_2^- , S_2^- , Notice that the total number of bifurcation points increases to infinity as $\mathcal{K} \rightarrow \infty$. Now consider the case when $\mathcal{K} = \text{const}$ and \mathcal{P} is varied. A line $\mathcal{K} = \text{const}$ in the $(\mathcal{K}, \mathcal{P})$ plane cuts again each line of the bifurcation points D_i and S_i in two points which we denote D_i^* , S_i^* , ... (solutions with longer lengths) and D_i^{**} , S_i^{**} , ... (solutions with shorter lengths), see Figs. 6 and 8. In most cases, one of these two points is a bifurcation originating from the \hat{L}_- trivial solution while the other is from the \hat{L}_+ trivial solution. However, as we show in the inset in Fig. 8, the two points may also bifurcate from the same branch \hat{L}_+ . As we show later in the paper such bifurcations are of particular interest because they describe both motility initiation and motility arrest.

Structure of bifurcations: After the bifurcation points are known one can use the Lyapunov–Schmidt reduction technique to identify the nature of the corresponding bifurcations (Nirenberg, 1974; Koiter, 1976; Amazigo et al., 1970). The analysis presented in Appendix C shows that the bifurcations from the trivial to the nontrivial static branch are always transcritical. The bifurcations to motile branches can be either subcritical or supercritical. In particular, at a given \mathcal{K} , the bifurcation from a static homogeneous solution with longer length is always supercritical while the bifurcation from a static homogeneous solution with smaller length can be either subcritical or supercritical depending on the value of \mathcal{K} , see Appendix C.

Bifurcated branches: To illustrate different types of bifurcations we constructed the nonlinear continuation of the bifurcated branches by solving the boundary value problem (27)–(28) numerically for successive values of parameters \mathcal{K} and \mathcal{P} (tracking algorithm, see Doedel et al., 2007). In Fig. 9(a), we show the continuation in \mathcal{K} for both static and motile configurations at fixed \mathcal{P} ; the corresponding profiles of motor concentration, stress and velocity are shown in Fig. 9(b). One can see that each pitchfork (for motile branches) and each transcritical (for static branches) bifurcation points gives rise to two nontrivial solutions. For instance, along the static branch \hat{L}_+ , the bifurcation point D_1^+ is associated with two motile supercritical branches whereas the point S_1^+ is associated with two transcritical static branches. Each pair of motile solutions is symmetric with two opposite polarizations corresponding to two different signs of the velocity. Along the first motile branch originating at D_1^+ , the myosin motors concentrate at the trailing edge. For the second motile branch originating at D_2^+ , there is an additional peak in the concentration profile, see Fig. 9(b). In contrast, the static bifurcation point S_1^+ gives rise to two symmetric configurations with different lengths and with myosin motors concentrated either in the middle of the cell or near the boundaries, see Fig. 9(b). As one would expect, the higher order static and motile bifurcation points produce solutions with more complex internal patterns. For the branches bifurcating from the trivial configurations belonging to \hat{L}_- family, the picture is similar, see Fig. 9(a).

In Fig. 10, we show in more detail the nontrivial solutions originating from the motile bifurcation points D_1 at two values of parameter \mathcal{K} which correspond to two sections $\alpha\beta$ and $\alpha\beta'$ shown in Fig. 8 (insert). Notice that a single solution connects the bifurcation points D_1^* (supercritical) and D_1^{**} (sub- or supercritical) which may belong either to one family \hat{L}_+ ($\alpha\beta$ where D_1^* is the same as D_1^+ and D_1^{**} is the same as D_1^+) or to two different families \hat{L}_+ and \hat{L}_- ($\alpha\beta'$ where D_1^* is the same as D_1^+ and D_1^{**} is the same as D_1^-). In the former case, the nontrivial motile branch has a turning point at a finite value of $\mathcal{P} < 1/4$ giving rise to a re-entrant behavior. Similar behavior was also observed in some other nonlocal models (e.g. Kruse and Jülicher, 2003; Tjhung et al., 2012; Giomi and DeSimone, 2014).

As illustrated in Fig. 10 and shown more clearly in a phase diagram in Fig. 11(a), in the re-entrant regime (sufficiently low \mathcal{K}), the increase of the average concentration of myosin (increase of \mathcal{P} at fixed \mathcal{K}) first polarizes the cell and initiates

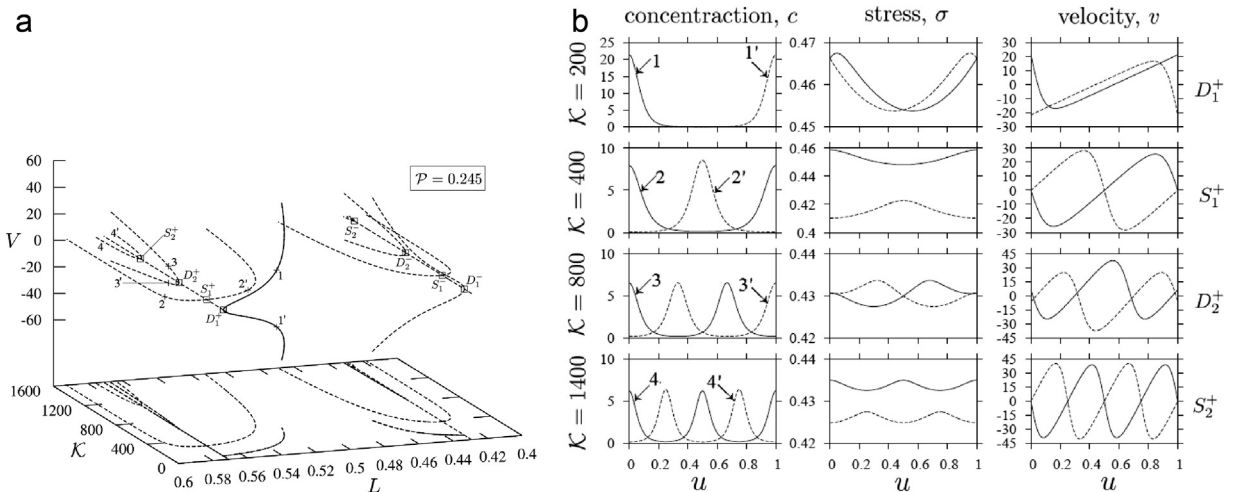


Fig. 9. (a) Bifurcation diagram with \mathcal{K} as a parameter showing nontrivial solutions branching from families of homogeneous static solutions \hat{L}_+ and \hat{L}_- . The value $\mathcal{P} = 0.245$ and $\mathcal{Z} = 1$ are fixed. Solid lines show stable motile branches while all the dotted lines correspond to unstable solutions. The internal configurations corresponding to branches indicated by numbers (1, 1', 2, 2', etc.) are shown in Fig. 9(b). The projection of the bifurcation diagram on the (\mathcal{K}, L) plane is also shown below. (b) Internal profiles associated with successive bifurcated solutions shown in Fig. 9(a) for $\mathcal{P} = 0.245$ and $\mathcal{Z} = 1$. Our notation (1,3) correspond to asymmetric motile branches while (2,4) describe symmetric static branches.

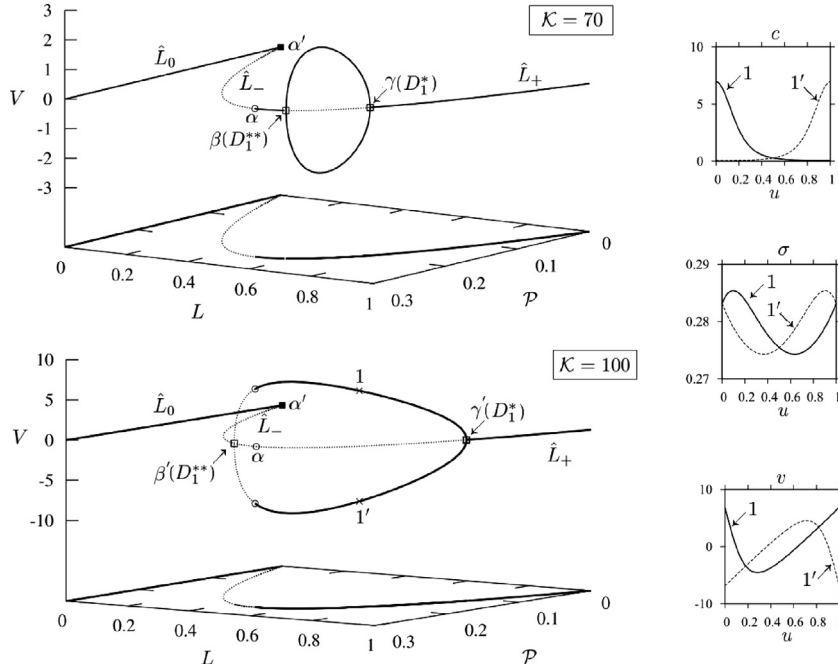


Fig. 10. Bifurcation diagrams along parameter \mathcal{P} showing motile branches connecting points D_1^* and D_1^{**} . Corresponding bifurcation points are shown in insert in Fig. 8. Solid lines show stable motile branches while all the dotted lines correspond to unstable solutions. The projection of the bifurcation diagram on the (\mathcal{P}, L) plane is also shown. Parameter \mathcal{K} is fixed in each graph to $\mathcal{K} = 70$ and $\mathcal{K} = 100$. Internal profiles on the two symmetric motile branches are also shown for $\mathcal{K} = 100$. Parameter $\mathcal{Z} = 1$.

motility, but then, if the contractility is increased further, the cell may become symmetric again by re-stabilizing in another static homogeneous configuration (see Fig. 10, $\mathcal{K} = 70$). We reiterate that re-symmetrization and arrest prior to division (known also as ‘mitotic cell rounding’) is a common feature of almost all animal cells (Stewart et al., 2011; Lancaster et al., 2013; Lancaster and Baum, 2014). In this respect, it is interesting that if contractility (\mathcal{P}) is increased further, the cell collapses to a point because our effective ‘size preserving spring’ cannot support the contraction any more. Following Turlier et al. (2014), we can associate such collapse with cell division. We can then argue that our deliberately minimalistic model succeeds in reproducing a rather general pattern of cell behavior by showing that symmetrization (stabilization) in space immediately precedes the division.

While the physical meaning of the non-dimensional parameter \mathcal{P} in this discussion is rather clear (contractility measure), the significance of varying \mathcal{K} at fixed \mathcal{Z} is less obvious because both these parameters depend on frictional strength of the background. Adhesivity of the cell to the substrate is known to be a crucial parameter for motility initiation and arrest for

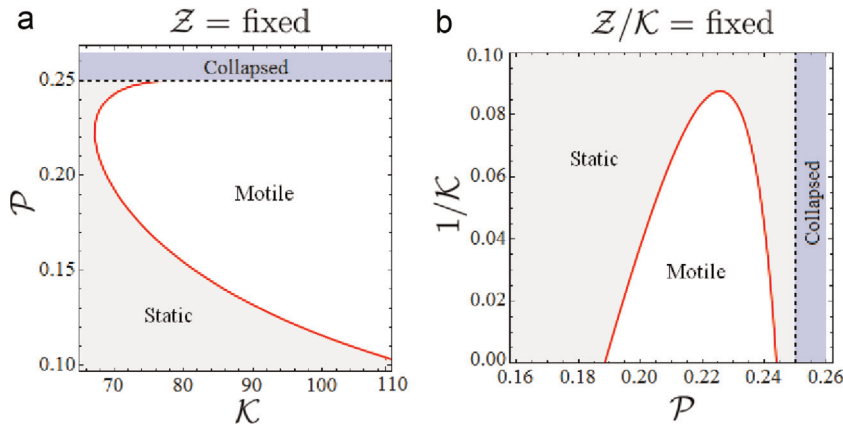


Fig. 11. (a) Phase diagram of the system (13) in the parameter plane $(\mathcal{K}, \mathcal{P})$ at fixed $\mathcal{Z} = 1$. (b) Phase diagram of the same system (13) in the parameter plane $(\mathcal{P}, 1/\mathcal{K})$ at fixed $\mathcal{Z}/\mathcal{K} = 0.015$. The solid (red) line indicates the motile bifurcation point (D_1^* similar to Fig. 8), while the black dashed lines indicate the collapse threshold ($\mathcal{P}_{\max} = 1/4$). (For interpretation of the references to color in this figure caption, the reader is referred to the web version of this paper.)

various cell types (Banerjee and Marchetti, 2011; Löber et al., 2014). To explicitly expose the role of friction, it is instructive to interpret parameter $1/\mathcal{K}$ as a measure of adhesivity while maintaining at a constant level the parameter \mathcal{Z}/\mathcal{K} , which does not have any relation to surface friction and is just a ratio of diffusive and viscous time scales.

The resulting phase diagram in the $(\mathcal{P}, 1/\mathcal{K})$ plane at fixed \mathcal{Z}/\mathcal{K} is shown in Fig. 11(b). In this diagram a horizontal path extending from left to right means fixed adhesivity and increasing contractility. One can see that at high adhesivity motility regimes cease to exist and static solutions collapse as contractility increases. If the adhesivity is below a certain threshold, the contractility increase first causes polarization of a static configuration and motility initiation; further increase of contractility causes re-symmetrization, arrest and eventually collapse. An interesting regime corresponds to the very tip of the motile domain shown in Fig. 11(b). Near this ‘critical’ point the motility can be sustained in a narrow ‘homeostatic window’ of parameters and can be easily arrested by either increase or decrease of contractility.

Very recently new experimental results elucidating motility initiation in fish keratocytes have appeared (Barnhart et al., 2015). According to these experiments, at a fixed contractility level (fixed \mathcal{P} in our model), the increase of surface adhesivity (increase of $1/\mathcal{K}$ in our model) promotes static configurations while lowering adhesivity initiates motility. As it follows from Fig. 11(b), these observations are in agreement with our predictions. Our model also explains another observation made in Barnhart et al. (2015) that at a fixed adhesivity, a blebbistatin (a contractility inhibitor) treatment promotes arrest of the cells while a calyculin A treatment (a contractility stimulator) initiates motility. The question whether a more substantial increase of contractility in experiment can lead to re-symmetrization and arrest remains open. It is promising in this respect that some cells are known to undergo static to motile transformation in response to a *decrease* in the level of contractility (Liu et al., 2010; Hur et al., 2011). The minimal model presented in Barnhart et al. (2015) is exactly a 2D version of the one formulated in Recho et al. (2013) and further developed in the present paper. While active protrusion and non-linear regulation of adhesion were also accounted for in Barnhart et al. (2015) to get a realistic cell shape, it is rather remarkable that the fundamental pattern of motility initiation (including its dependence on contractility and adhesivity) can be already captured within our much more transparent setting, see Fig. 11(b) and Section 8.

Nonlinear active stress: The fact that the bifurcation leading to polarization and motility initiation is always a supercritical pitchfork indicates that this model does not allow for metastability resulting in the coexistence of motile and non-motile configurations that was observed in other models (e.g. Ziebert and Aranson, 2013; Tjhung et al., 2012; Giomi and DeSimone, 2014). To obtain such a coexistence in the present setting, we need to modify our model only slightly. The main idea is to consider a more realistic nonlinear dependence of the active stress on motor concentration which is linear for small values of c but then saturates after around a threshold c^* . More specifically, we rewrite the main system of equations in the form

$$\begin{aligned} -\mathcal{Z}\partial_{xx}\sigma + \sigma &= \mathcal{P}\Phi(rc)/r, \\ \partial_t c + \mathcal{K}\partial_x(c\partial_x\sigma) &= \partial_{xx}c, \end{aligned} \quad (40)$$

where, following Bois et al. (2011), we choose a particular form of nonlinearity $\Phi(x) = x/(1+x)$ and where we introduce the new non-dimensional parameter $r = c_0/c^*$.

For simplicity we analyze below only the ‘rigid’ limit when $k \rightarrow \infty$, $L \rightarrow L_0$ while the stress on the boundaries $-k(L/L_0 - 1)$ remains finite. Notice that in this limit, which formally means that $\mathcal{P} \rightarrow 0$ and $\mathcal{K} \rightarrow \infty$, we have to re-scale the stress by $c_0\chi$ instead of k and as a consequence in the rest of the section we denote, with some abuse of notations, $\sigma := \sigma/\mathcal{P}$. The new dimensionless parameter replacing \mathcal{K} and \mathcal{P} is $\lambda = c_0\chi/(\xi D) = \mathcal{K}\mathcal{P}$ that is assumed to be finite (see also Bois et al., 2011; Howard et al., 2011; Hawkins et al., 2009a, 2011). In dimensionless variables the residual stress can be written as $\sigma_0 = -\lim_{\mathcal{P} \rightarrow 0} \lim_{L \rightarrow 1} (L - 1)/\mathcal{P}$. Then the boundary conditions read

$$\begin{aligned} \dot{l}_+ - \dot{l}_- &= 0 \\ \sigma(l_{\pm}(t), t) &= \sigma_0 \\ \partial_x c(l_{\pm}(t), t) &= 0 \\ \dot{l}_{\pm} &= \lambda \partial_x \sigma(l_{\pm}(t), t). \end{aligned}$$

For TW solutions we can write the analogue of (27)

$$-\mathcal{Z}s'' + s + s_0 = \frac{\lambda}{r}\phi\left(r\frac{\exp(s - Vu)}{\int_0^1 \exp(s - Vu) du}\right), \quad (41)$$

where $s = \lambda(\sigma - \sigma_0)$ and $s_0 = \lambda\sigma_0$. The boundary conditions take the form $s(0) = s(1) = 0$ and $s'(0) = s'(1) = V$. The difference with our static solutions, described in Section 4, is that now we have to find the stress at the boundary s_0 instead of the length L .

The analysis of the motility initiation bifurcation in this case is presented in Appendix D. The results are illustrated in Fig. 12. As we see, when the nondimensional parameter r is small, which means that we are in the linear regime, the bifurcation from static to motile regime is a supercritical pitchfork. However, at larger values of r the nature of the bifurcation changes from supercritical to subcritical. This creates a domain of parameters where static and motile regimes can coexist and where the system may exhibit metastability and hysteresis. Another important effect is that in this range of

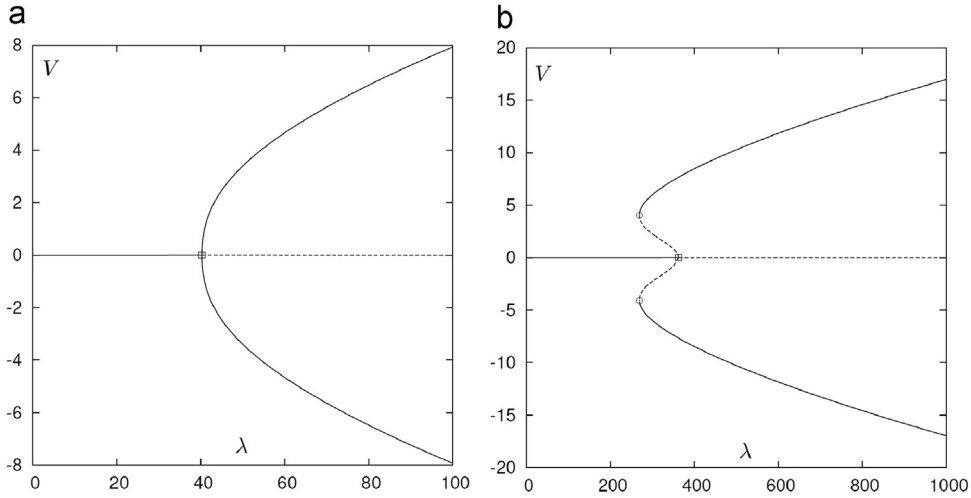


Fig. 12. Bifurcation diagrams in the nonlinear model with fixed length (infinite stiffness) (41) showing the possibility of a switch from supercritical to subcritical bifurcation. Parameters: $Z = 1$. (a) $r=1$ and (b) $r=5$.

parameters the motility initiation/arrest is a discontinuous transition which may explain why experimenters were unable to observe particularly small velocities of self-propulsion in keratocytes (Barnhart et al., 2011). An alternative explanation of this experimental fact based on the idea of optimality and compatible with the supercritical nature of the motility initiation bifurcation was proposed by Recho et al. (2014).

6. Stability of post-bifurcational regimes

Stability of various branches of the TW solutions identified in the previous sections was studied numerically. Since we have to deal with a moving segment, it is convenient to map system (13) onto the fixed domain $[0, 1]$ which makes the coefficients of the governing equations time dependent. To this end, we introduce the new space variable $u(x, t) = [x - L(t)]/L(t) \in [0, 1]$ and denote the new unknown functions $\hat{\sigma}(u, t) = \sigma[L + L(t)u, t]$ and $\hat{c}(u, t) = L(t)c[L + L(t)u, t]$. Then the original problem (13), (15)–(16) takes the form

$$-\frac{Z}{L^2} \partial_{uu} \hat{\sigma} + \hat{\sigma} = \frac{\mathcal{P}}{L} \hat{c} \quad \text{and} \quad \partial_t \hat{c} + \frac{1}{L} \partial_u (\hat{v} \hat{c}) = \frac{1}{L^2} \partial_{uu} \hat{c}, \quad (42)$$

Here we defined the relative velocity $\hat{v} := \mathcal{K} \partial_u \hat{\sigma} / L - \dot{G} - (u - 1/2) \dot{L}$, where

$$\begin{aligned} \dot{G} &= (\mathcal{K}/L) [\partial_u \hat{\sigma}(1, t) + \partial_u \hat{\sigma}(0, t)]/2, \\ \dot{L} &= (\mathcal{K}/L) [\partial_u \hat{\sigma}(1, t) - \partial_u \hat{\sigma}(0, t)]. \end{aligned} \quad (43)$$

The remaining boundary conditions can be written as

$$\hat{\sigma}(u, t) = -(L - 1) \quad \text{and} \quad \partial_u \hat{c}(u, t) = 0 \quad \text{at } u = \{0, 1\}. \quad (44)$$

while the initial data take the form $\hat{c}(u, 0) = \hat{c}^0(u)$, $G(0) = G^0$ and $L(0) = L^0$.

We integrated the dynamical system (42)–(44) with initial data chosen close to one of the known steady states. The numerical scheme was based on the finite volume method (LeVeque, 2002). We used two dual regularly spaced grids on the interval $[0, 1]$: Z and Z_d . Given the initial condition \hat{c} we solved (42)₁ on Z and computed the effective drift term \hat{v} on Z_d . We then applied the upwind finite volume scheme to (42)₂ and updated the concentration profile \hat{c} on Z which provided us with the new initial data for the next time step. The time interval for each time step was adapted to ensure that the Courant–Friedrichs–Lewy condition is uniformly satisfied on Z_d .

Our numerical experiments suggest that the trivial branch \hat{L}_- is unstable together with all nontrivial non-singular static solutions. The singular static solutions from the \hat{L}_0 family appear to be locally stable. To illustrate the attractive nature of the singular static solutions we choose in Fig. 13 the initial configuration with a length smaller than \hat{L}_- with an internal initial profile biased to the front associated to a motile solution. We observe that the length collapses to zero in finite time and cell velocity goes to zero. In accordance with the computations made in Section 4, the stress profile converges to $s(u)/L \sim \mathcal{K} \mathcal{P} u(u - 1)/2$, velocity to $v(u) \sim \mathcal{K} \mathcal{P} (u - 1/2)$ and concentration to $c(u) = 1$.

Next, we observed numerically that the dynamic solutions are all unstable except for the branches bifurcating from the points D_1^+ on the trivial branch \hat{L}_+ . The trivial branch \hat{L}_+ branch is locally stable until the first (motile) bifurcation D_1^+ . Both symmetric subbranches of D_1^+ (subfamilies 1 and 1' in Fig. 9(a) and (b)) are stable. To illustrate the instability of a nontrivial

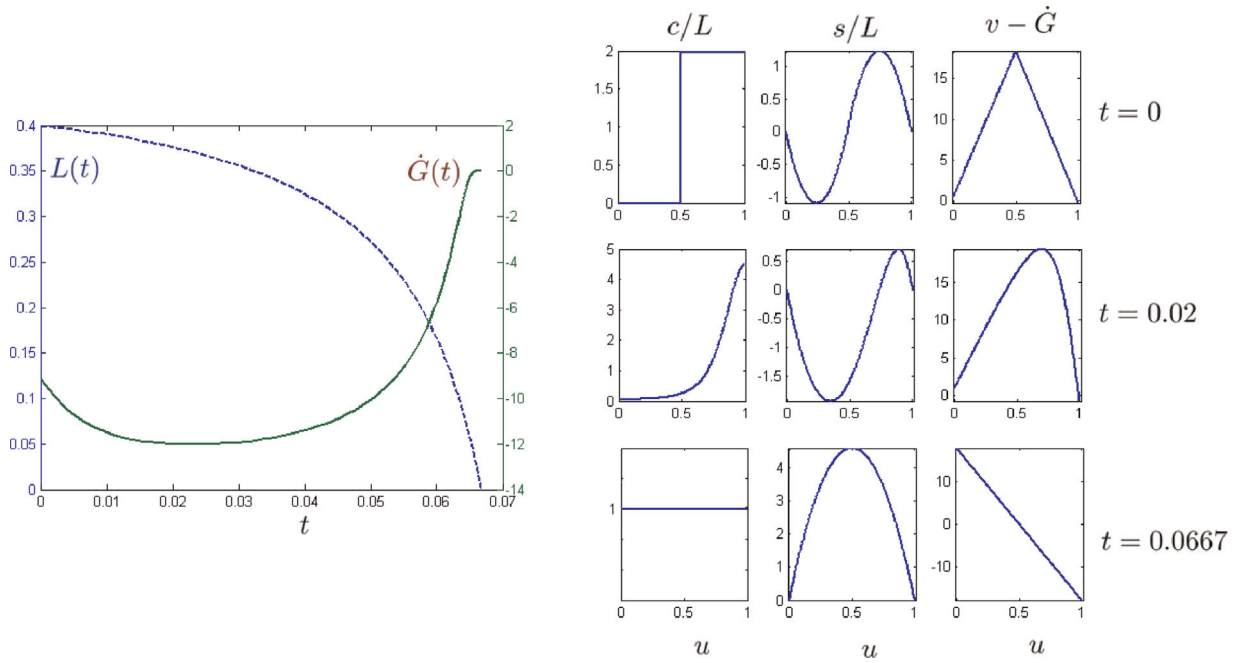


Fig. 13. Cell length $L(t)$, velocity $\dot{G}(t)$ and profiles $c/L(u, t)$, $s/L(u, t)$ and $v(u, t) - \dot{G}(t)$ for the test with initial data shown at $t=0$ with $L(0) = 0.4$. Parameters $\mathcal{P} = 0.245$, $\mathcal{K} = 150$ and $\mathcal{Z} = 1$ as in Fig. 9(a). The layer collapses due to the contractile stress.

static solution, we show in Fig. 15 the escape of the phase trajectory from the neighborhood of the trivial static solution \hat{L}_- . Since in this numerical test the value of \mathcal{K} was chosen to be smaller than the critical value, corresponding to the bifurcation of the first motile branch D_1^+ , the system originally placed near \hat{L}_- becomes unstable and then re-equilibrates on another trivial static branch \hat{L}_+ without moving its geometrical center.

In Fig. 14 we illustrate motility initiation in two initially almost identical and nearly homogeneous static configurations which differ by a localized concentration peak introduced either at the rear or at the front of the cell. We see that with time these two initial profiles converge to the different stable motile solutions D_1 and D_1' . The initial inhomogeneity is remembered and selects the subfamily of the D_1 solutions with the same bias. As we see, independently of the direction of

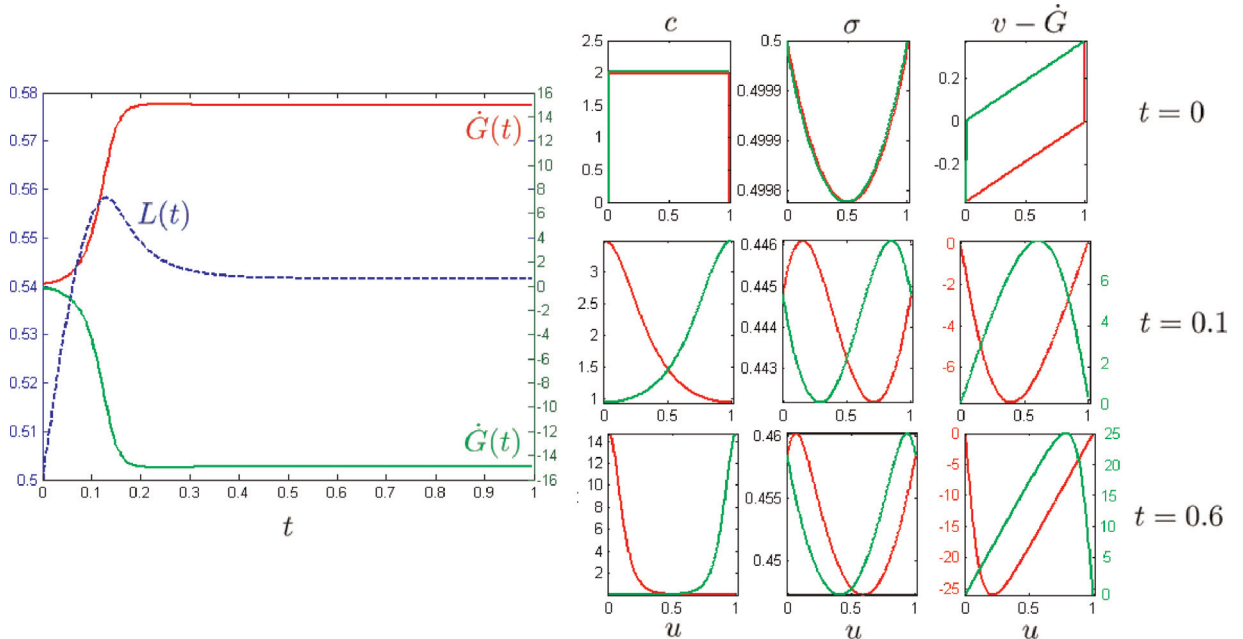


Fig. 14. (Color online) Cell length $L(t)$, velocity $\dot{G}(t)$ and profiles c , σ and $v(u, t) - \dot{G}(t)$ for the test with initial data shown at $t=0$ with $L(0) = 0.5$. Parameters $\mathcal{P} = 0.245$, $\mathcal{K} = 150$ and $\mathcal{Z} = 1$ as in Fig. 9(a). The layer polarizes to one the motile attractor (depending on the initial bias).

motion the cell recovers its length after a short transient period.

As in Bois et al. (2011), Howard et al. (2011), and Kruse and Jülicher (2003), who considered the problem with fixed boundaries, we find that some unstable multi-peaked static and dynamic solutions are long living. This behavior is reminiscent of the spinodal decomposition in a 1D Cahn–Hilliard model where the coarsening process gets critically slowed down near multiple saddle points (Carr and Pego, 1989). To illustrate the long transients near the unstable solutions we study in Fig. 16 evolution of two initially homogeneous concentration profiles with different initial lengths. We observe that the phase trajectory first approaches the unstable branch from subfamily 2 from Fig. 9(a) and (b) before being finally attracted by the stable configuration from the subfamily 1'. Interestingly, the symmetric subfamily 2' can be also initially approached if we choose slightly different initial data, however, this regime is abandoned much faster than the solution from the subfamily 2, see Fig. 16(b). Based on our simulation, we conjecture that the lifespan of an unstable branch is linked to the distribution of motors and the states with higher localization of motors on the periphery of the cell survive longer than the states where motors are spread near the center of the cell.

To summarize, we found considerable numerical evidence that in a problem with *free* boundaries only trivial static solutions can be stable and only solutions with monotone profiles can describe configurations of steadily moving cells. To confirm these results a more systematic mathematical analysis of stability of the obtained TW solutions is needed. Cells with *constrained* or loaded boundaries may show different stability patterns as it is evidenced by the study of a related problem with a periodic boundary conditions (Bois et al., 2011; Howard et al., 2011; Kruse and Jülicher, 2003).

7. Mass transport of actin

As we have already mentioned, the infinite compressibility assumption allowed us to decouple the force balance equation from the mass balance equation. Once the velocity field $v(x, t) = \mathcal{K} \partial_x \sigma(x, t)$ is known, the latter can be solved a posteriori by the method of characteristics.

Denote the trajectories of the mass particles by $x = \phi(\zeta, t)$, where $L_-(0) \leq \zeta \leq L_+(0)$ is the Lagrangian coordinate at $t=0$ and $L_-(t) \leq \phi(\zeta, t) \leq L_+(t)$. The characteristic curves can be found from the equations

$$\frac{d\phi(\zeta, s)}{ds} = v(\phi(\zeta, s), s). \quad (45)$$

Along these curves we must have

$$\frac{d\rho(\phi(\zeta, s), s)}{ds} = -\rho(\phi(\zeta, s), s) \partial_x v(\phi(\zeta, s), s).$$

Integration of this equation gives an explicit formula for the mass density

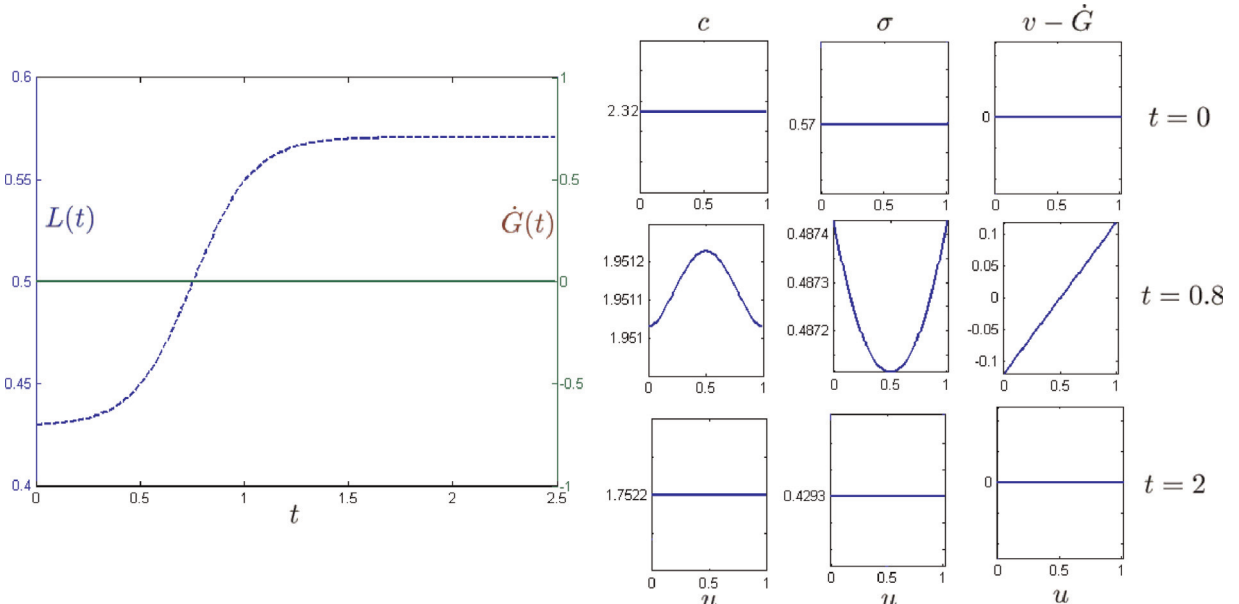


Fig. 15. Cell length $L(t)$, velocity $\dot{G}(t)$ and profiles c , σ and $v(u, t) - \dot{G}(t)$ for the test with initial data shown at $t=0$ with $L(0) = \hat{L}_-$ and the homogeneous concentration $c^0(u) = 1/\hat{L}_-$. Parameters $\mathcal{P} = 0.245$, $\mathcal{K} = 50$ and $\mathcal{Z} = 1$ as in Fig. 9(a). The layer restabilizes from the homogeneous branch \hat{L}_- to \hat{L}_+ .

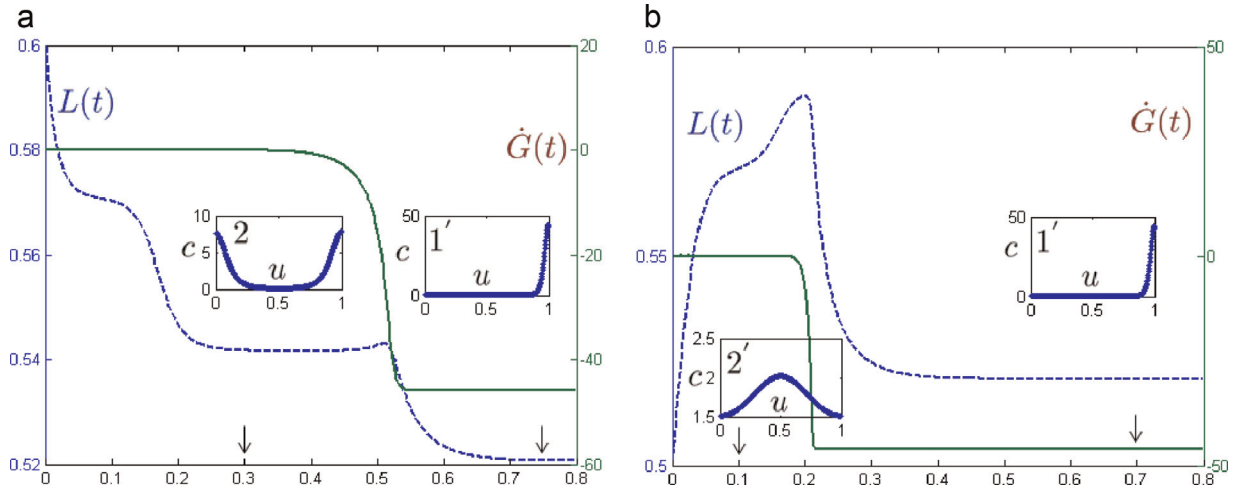


Fig. 16. Cell length $L(t)$ and velocity $\dot{G}(t)$ for the test with $P = 0.245$, $K = 400$ and $Z = 1$ starting from homogeneous initial state with different initial lengths $L(0) = 0.6$ (left) and $L(0) = 0.5$ (right). The labels refer to Fig. 9(a), (b). The two non-trivial static branches bifurcating from S_1^+ denoted 2 and 2' in Fig. 9(a) and (b) have very different kinetic properties.

$$\rho(\phi(\zeta, t), t) = \rho_0(\zeta) \exp \left\{ - \int_0^t \partial_x v(\phi(\zeta, s), s) ds \right\}. \quad (46)$$

As we are going to see below, this solution is applicable only outside the singular points describing the sinks and the sources.

Consider a TW solution of (13) which satisfies the boundary conditions $L_-(t) = Vt$ and $L_+(t) = L + Vt$. Introducing the normalized co-moving variable $\hat{\phi} = (\phi - Vt)/L$ and the normalized Lagrangian variable $\hat{\zeta} = \zeta/L(0)$, both in the interval $[0, 1]$, we obtain that $v = v(\hat{\phi})$ and Eq. (45) reduces to

$$\frac{d\hat{\phi}(\hat{\zeta}, t)}{dt} = \frac{v(\hat{\phi}(\hat{\zeta}, t)) - V}{L}. \quad (47)$$

For TW solutions the general formula (46) describing the mass distribution simplifies

$$L\rho(\hat{\phi}(\hat{\zeta}, t), t) \{v(\hat{\phi}(\hat{\zeta}, t)) - V\} = L(0)\rho_0(\hat{\zeta}) \{v(\hat{\zeta}) - V\}. \quad (48)$$

According to (47) the points of the body where $v = V$ are singular because the relative flow there is stagnated. If at such point the slope of the function $v(\hat{\phi})$ is negative we obtain a sink of particle trajectories $\hat{\phi} = \gamma_+$ (i.e. an attractor for particles as $t \rightarrow \infty$) whereas if the slope of the function $v(\hat{\phi})$ is positive, the singular point $\hat{\phi} = \gamma_-$ corresponds to a source of particle trajectories (an attractor as $t \rightarrow -\infty$). An important feature of the flows described by (47) is that it takes an infinite time for a mass particle to reach a sink or to leave a source because $(v(\hat{\phi}) - V)^{-1}$ is not integrable in the neighborhood of γ_- and γ_+ :

$$\tau = \int_{\gamma_-}^{\gamma_+} \frac{d\hat{\phi}}{|v(\hat{\phi}) - V|} = \infty.$$

This implies that mass density infinitely localizes in the singular points (sources and sinks) because $L\rho(\hat{\phi})|v(\hat{\phi}) - V| = \tau^{-1} = 0$. Then all mass points (corresponding to different values of $\hat{\zeta}$) come from the sources where the characteristic curves accumulate at large negative times and disappear in the sinks where the characteristic curves accumulate at large positive time.

For the trivial static solutions characterized by the lengths \hat{L}_{\pm} , there is no flow ($v - V = 0$) and the mass density does not depend on either space or time. The density profiles for nontrivial static and motile solutions can be illustrated near the bifurcation points where the velocity profiles are known explicitly.

For instance, in the case of the nontrivial static branches S_m^{\pm} introduced in Section 5, we obtain

$$\frac{d\hat{\phi}(\hat{\zeta}, t)}{dt} = \varsigma \sin(\omega_c \hat{\phi}(\hat{\zeta}, t)), \quad (49)$$

where $\omega_c = -2m\pi$. For determinacy, we choose the value of the amplitude ς in such a way that the maximum of our dimensionless velocity field is equal to one. The approximate value of ς can be computed in the vicinity of the bifurcation point from the amplitude equations presented in Appendix C. In Fig. 17(a) we show sample solutions of (49) corresponding

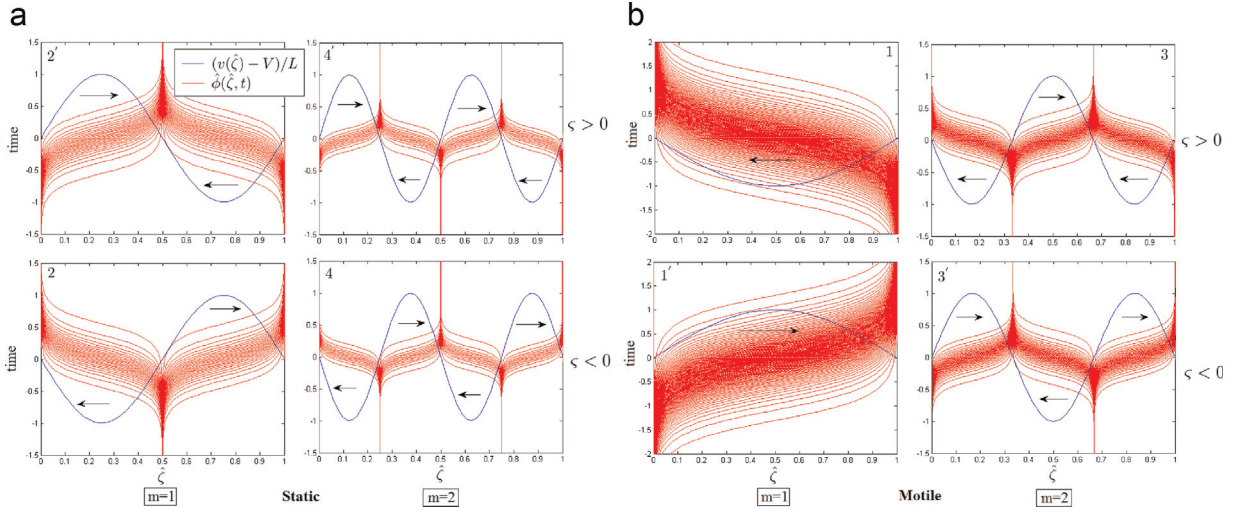


Fig. 17. (a) Trajectories of particles from sources to sinks for the first two static bifurcation points for initially homogeneously distributed set of particles. (b) Trajectories of particles from sources to sinks for the first two motile bifurcation points for initially homogeneously distributed set of particles. Labels 1, 1', 3, 3' and labels 2, 2', 4, 4' are related to Fig. 9(a) and (b).

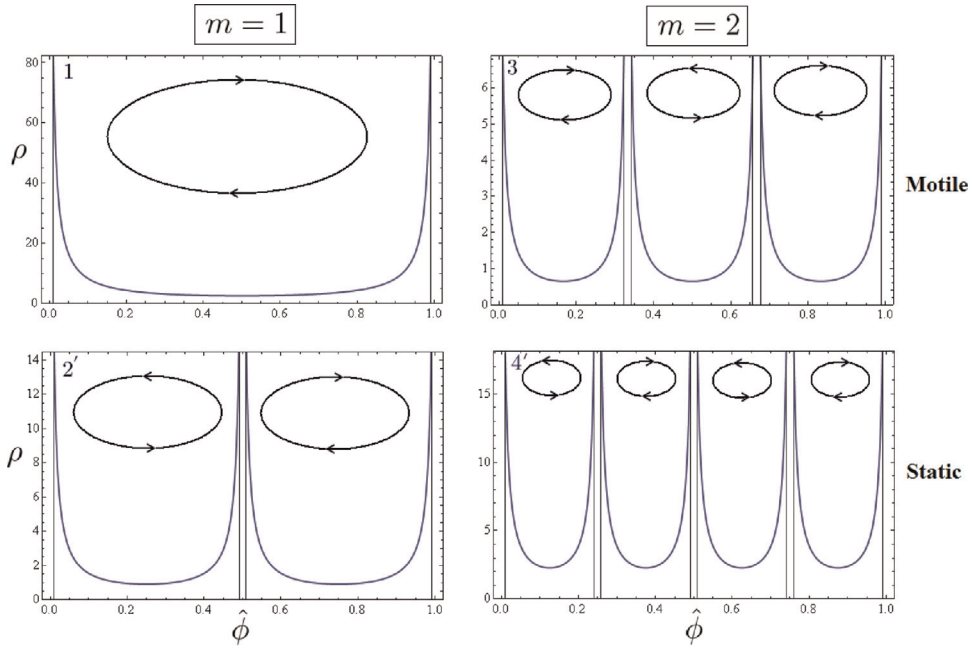


Fig. 18. Density profiles for the first two motile and static branches for $\zeta > 0$, the profiles for $\zeta < 0$ are the same; only the treadmilling cycles (indicated by black circles) are going in the opposite direction. Labels are related to Fig. 9(a) and (b). Parameter is $\epsilon = 0.01$.

to homogeneous initial conditions $\hat{\phi}(\hat{\zeta}, 0) = \hat{\zeta}$ for positive and negative values of ζ corresponding to the two possible branching directions. The corresponding density profiles are illustrated in Fig. 18 where the passive treadmilling cycles are shown by arrows.

Similarly, for the motile branches D_m^\pm we need to solve the characteristic equation

$$\frac{d\hat{\phi}(\hat{\zeta}, t)}{dt} = \zeta \left\{ -\frac{L^2}{\omega_c^3 \cos(\omega_c/2)} \left[\omega_c \cos(\omega_c(\hat{\phi}(\hat{\zeta}, t) - 1/2)) - 2 \sin(\omega_c/2) \right] - 1 \right\}, \quad (50)$$

where ω_c is a solution of Eq. (B.2). Both equations can be solved analytically by separation of variables. In Fig. 17(b), we show the sample solutions of (50) corresponding to homogeneous initial conditions $\hat{\phi}(\hat{\zeta}, 0) = \hat{\zeta}$ again for the positive and negative values of ζ .

We reiterate that this model is singular because in a one dimensional setting we are obliged to over-schematize the treadmilling of actin. To recover the circulation aspect of the flow in a one-dimensional setting, we need to regularize the problem near the singular points and make the mass flux finite. For instance, we can cut out small regularizing domains of size ϵ around sinks and sources. In this way we obtain an effective ‘polymerization zone’ around each source $\Gamma_- = \{\hat{\phi} \in [0, 1] / |\hat{\phi} - \gamma_-| < \epsilon\}$ and an effective ‘depolymerization zone’ around each sink $\Gamma_+ = \{\hat{\phi} \in [0, 1] / |\hat{\phi} - \gamma_+| < \epsilon\}$. We assume that in the domain Γ_- the network is constantly assembled from the abundant monomers while in the domain Γ_+ it is constantly disassembled so that the pool of monomers is replenished. The ensuing closure of the treadmilling cycle is instantaneous (jump process) allowing the monomers to avoid the frictional contact with the environment. More precisely, we assume that the jump part of the treadmilling cycle is a passive equilibrium process driven exclusively by myosin contraction. The turnover time

$$\tau = \int_{\partial\Gamma_-}^{\partial\Gamma_+} \frac{d\hat{\phi}}{|V(\hat{\phi}) - V|}$$

is now finite and the corresponding density profiles are illustrated in Fig. 18. Notice that the flow between the neighboring source and sink can be interpreted as a treadmilling cluster. Thus, for the m th static branch, we have $2m$ such clusters and for the m th motile branch we have $2m - 1$ clusters. We reiterate that according to the numerical stability analysis conducted in Section 6, the only *stable* motile solutions are the ones with a single treadmilling cycle extending from the leading to the trailing edge.

8. Experimental verification of the model

We can now compare the predictions of the model with experiments describing motility initiation in keratocytes. For instance, in the experiment of Verkhovsky et al. (1999), a mechanical force was transiently applied via a micropipette on one side of a keratocyte fragment. Since the data presented in Fig. 5 of Verkhovsky et al. (1999) (and reproduced with permission in our Fig. 19) are of one dimensional nature we can directly apply our model after adjusting it to account for mechanical loading.

In order to make quantitative predictions we need to specify the values of parameters relevant for fish keratocytes. In Barnhart et al. (2011), we find the values of viscosity $\eta \sim 10^5$ Pa s and active stress $\chi c_0 \sim 10^3$ Pa. The drag coefficient can vary over several orders of magnitude depending on the substrate whose physical properties have not been specified in Verkhovsky et al. (1999). However, based on the fact that, in Verkhovsky et al. (1999), the velocity of the fragment after

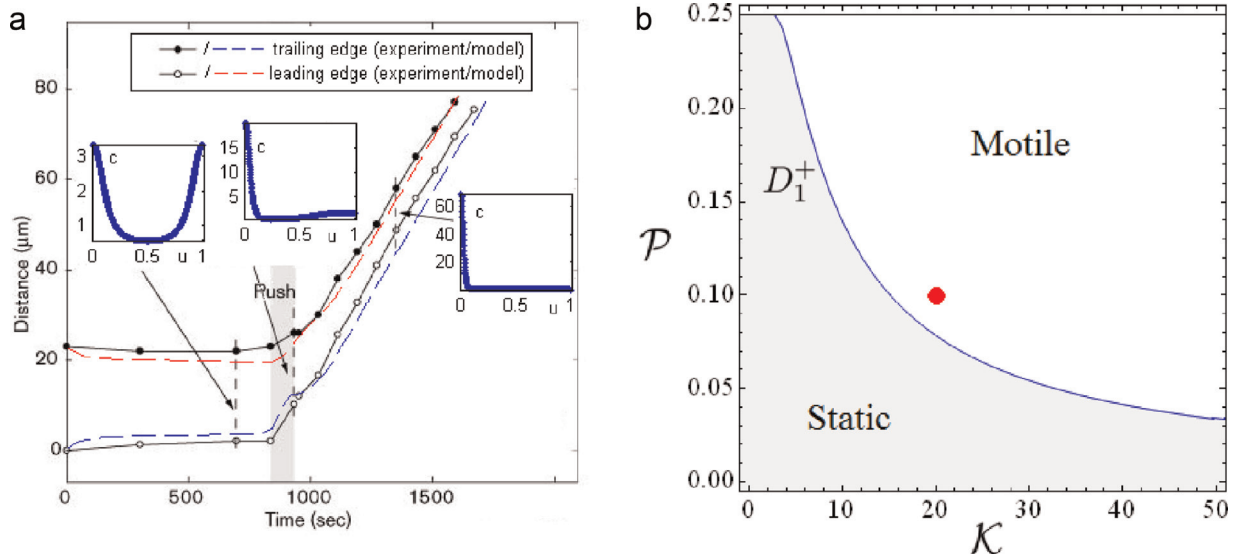


Fig. 19. (a) Comparison of numerics with the experiments performed by Verkhovsky et al. (1999). Parameter values: $Z = 0.0125$, $\mathcal{P} = 0.1$, $\mathcal{K} = 20$. Integration is started from an initial cell length of $L_i = 1.12$ with a homogeneous distribution of motors. In insets we show some snapshots of the distribution of motors obtained by numerical integration. The homogeneous configuration switches fast to a symmetric distribution where motors are relocating at both sides forming a two opposed lamellipods system. This state is long living but unstable and application of a transient loading leads to a break of symmetry and the subsequent localization of motors to the trailing edge forming a one lamellipod system. (b) Locus of the first motile bifurcation point associated to the homogeneous $\hat{\phi}_+$ branch for $Z = 0.0125$. Red dot shows the experimental data for keratocyte $\mathcal{P} = 0.1$ and $\mathcal{K} = 20$ which belongs to the motile regime. Such regime would be spontaneously reached under infinitesimal perturbations from a symmetric state but the long living nature of regime 2 (see Fig. 16) makes it necessary to impose a transient asymmetric perturbation to observe motility in experiments. (For interpretation of the references to color in this figure caption, the reader is referred to the web version of this paper.)

initiation of motility was approximately $0.08 \mu\text{m s}^{-1}$, we can infer from Fig. 5 of Barnhart et al. (2011) that $\xi \sim 2 \times 10^{16} \text{ Pa s m}^{-2}$. From Barnhart et al. (2011) and Luo et al. (2012), we can also obtain the value of the diffusion coefficient $D \sim 0.25 \times 10^{-13} \text{ m}^2 \text{ s}^{-1}$ and, from Barnhart et al. (2010), Du et al. (2012), and Loosley and Tang (2012), we estimate the stiffness of the cortex $k \sim 10^4 \text{ Pa}$. Finally, directly from Verkhovsky et al. (1999), we infer that the characteristic length of the keratocyte fragment is $L_0 \sim 20 \times 10^{-6} \text{ m}$. Based on these estimates we conclude that $Z \sim 0.0125$, $P \sim 0.1$ and $K \sim 20$.

In Verkhovsky et al. (1999) (Fig. 5), the initially round fragment with diameter $L_i = 22 \mu\text{m}$ was subjected to an applied stress of the order of $q_- = 15\text{--}20 \text{ kPa}$. The loading was applied after 830 s and lasted for about 80 s. The additional surface tractions can be easily incorporated into our model through the boundary condition at the rear of the cell: $\sigma(L_-(t), t) = -[L(t)/L_0 - 1] - q_-(t)$.

In Fig. 19(a) we present the results of our numerical simulation of the motility initiation experiment of Verkhovsky et al. (1999). We start with a uniform initial state where motors are distributed homogeneously. We chose a generic value of the length $L(0)$ that is slightly different from the value \hat{L}_+ which is unstable in this range of parameters. The length first decays towards the value corresponding to the branch S_1^+ as one could expect based on Figs. 9(a), (b) and 16. This is an unstable state which we found rather robust to selected perturbations. The distribution of motors remains non-polar with the development of two contractile zones characteristic of the nontrivial static regime S_2^+ . The system then remains in this long living unstable state until we apply an additional one-sided force on the boundary breaking the symmetry of the S_2^+ state. The destabilized system evolves towards the motile state on the D_1^+ branch with both velocity and length well captured by our model.

We can now compare with experiment the stationary density profiles (for both myosin and actin) generated by the model. In the static regime, the flow of actin is absent ($v=0$) and the model then predicts uniform distribution of actin and myosin. From Fig. 20 (left), we see that this prediction is in agreement with experimental observations given that we disregard fluctuations and neglect near-membrane effects.

From Rubinstein et al. (2009), the turnover time of actin can be estimated to be 30 s. Therefore we obtain in non-dimensional units that $\tau=0.018$ which leads to the estimate $\epsilon=0.015$. We recall ϵ accounts for the size of polymerization source and sink at the leading and trailing edge, see Section 7 for details. Knowing the value of ϵ , we can reconstruct the mass density distribution $\rho(u)$ which we show in Fig. 20 (right) together with the motor concentration distribution $c(u)$. One can see that outside the boundary layers the model captures the main effect: the sweeping of actin towards the de-polymerization zone at the back of the cell by the retrograde flow and its regeneration on the polymerization zone at the front of the cell. A more detailed quantitative comparison with experiment requires an account of the two (or even three) dimensional nature of the flow.

Overall, we can conclude that the model reproduces rather well the motility initiation pattern observed in Verkhovsky's experiment. Moreover, the ensuing dynamics is described adequately by the stable motile branch predicted by our theory formerly Fig. 19(b).

In another experiment by Yam et al. (2007), which we interpret here only qualitatively because of the absence of a natural 1D representation, motility was induced by injection of calyculin A, known to be a factor increasing the activity of myosin motors. The conventional interpretation of this experiment refers to the local variation of contractility which disrupts the actin flow and affects the cascade of polymerization and depolymerization (Paluch et al., 2006). Instead, from the perspective of our model it is natural to conjecture that the injection calyculin A affects the value of parameter P pushing it

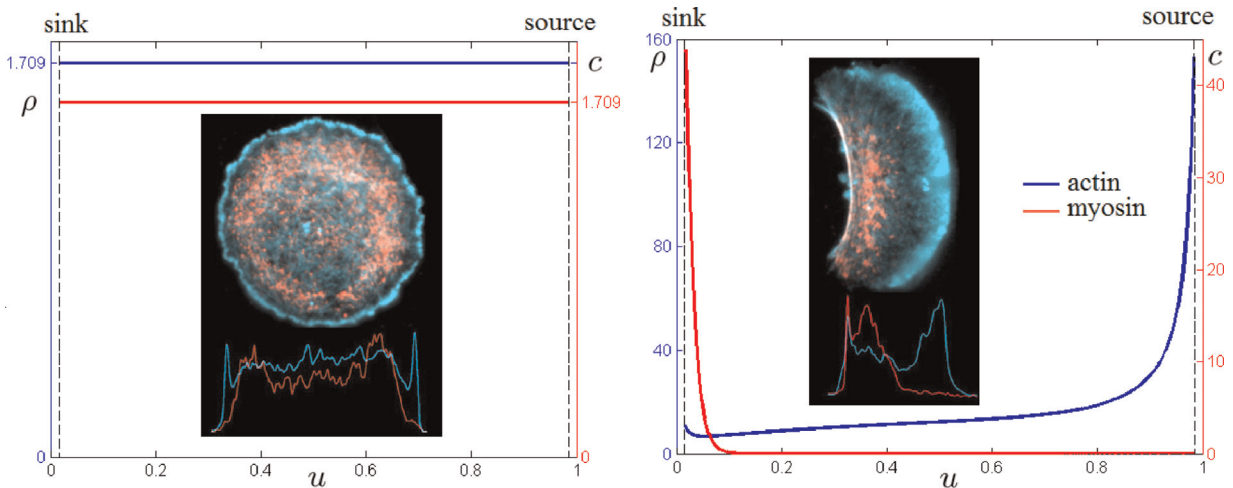


Fig. 20. Distribution of myosin (red) and actin (blue) in the static (left) and motile (right) regimes. Insets show the experimental distributions of actin (cyan) and myosin (red) from Verkhovsky et al. (1999). Picture is taken from <http://lcb.epfl.ch/cms/lang/en/pid/71379>, courtesy A. Verkhovsky. Parameter values: $Z = 0.0125$, $P = 0.1$, $K = 20$ and $\tau = 0.018$. (For interpretation of the references to color in this figure caption, the reader is referred to the web version of this paper.)

beyond the threshold where the static symmetric configuration is stable and initiating in this way the polarization instability which in turn leads to motility.

Notice that in both experiments by Verkhovsky et al. (1999) and by Yam et al. (2007), a fraction of keratocyte cells did not move at all after being exposed to the same mechanical or chemical perturbation as the cells that did become motile. This can be explained by the fact that the realistic values for \mathcal{P} and \mathcal{K} lay rather close to the boundary separating static and motile regimes, see Fig. 19(b). It is then feasible that some cells remain in the symmetric (static) regime despite the perturbation.

It is also feasible that the realistic dependence of active stress on myosin concentration saturates above a certain threshold which, as we have seen, can change the nature of the motility initiation bifurcation (D_1 branch) into a *subcritical* pitchfork, see discussion in Section 5. This opens a finite range of metastability where both the homogeneous static state and the inhomogeneous motile state are locally stable. The implied non-uniqueness may be an alternative explanation of the simultaneous presence of motile and non-motile cells despite apparently equal levels of contractility.

To exemplify this last claim, we show in Fig. 21 the effect of switching to threshold type dependence of contractile stress on the concentration of motors, see (40). Notice that we have dropped in Fig. 21 the assumption that the length of the moving segment is fixed. A comparison of Fig. 21 with Fig. 11(b) shows that the saturation of contractile stress introduces a finite zone of metastability between static and motile configurations: in this zone *finite* perturbations are required to switch from static to a motile regime. This prediction was very recently confirmed in vivo by Barnhart et al. (2015) and the metastability domain as in Fig. 21 was mapped experimentally. We also observe that for sufficiently large values of the active stress saturation threshold r , our model associates metastability with both, motility initiation and motility arrest. On the arrest side (Lancaster and Baum, 2014), this prediction can be linked to the metastability of cell division (Turlier et al., 2014) which to our knowledge has not been yet experimentally documented.

9. Conclusions

We studied a prototypical model of a crawling segment of an active gel showing the possibility of spontaneous polarization and steady self-propulsion in the conditions when contraction is the only active process. Our model, which focuses entirely on ‘pullers’, complements the existing theories of polarization and motility that place the main emphasis on ‘pushers’ and link motility initiation with active treadmilling and protrusion. Mathematically, the proposed model reduces to a dynamical system of Keller–Segel type, however, in contrast to its chemotactic analog, the nonlocality in this model is due to *mechanical* rather than *chemical* feedback. If compared with previous studies of Keller–Segel type problems, our setting is complicated by the presence of free boundaries equipped with Stefan type boundary conditions.

As we argue, the motor proteins with sufficient contractility induce internal stress which can overcome the hydrodynamic resistance and induce flow. The flow produces a drift of motors in the direction of the regions where they

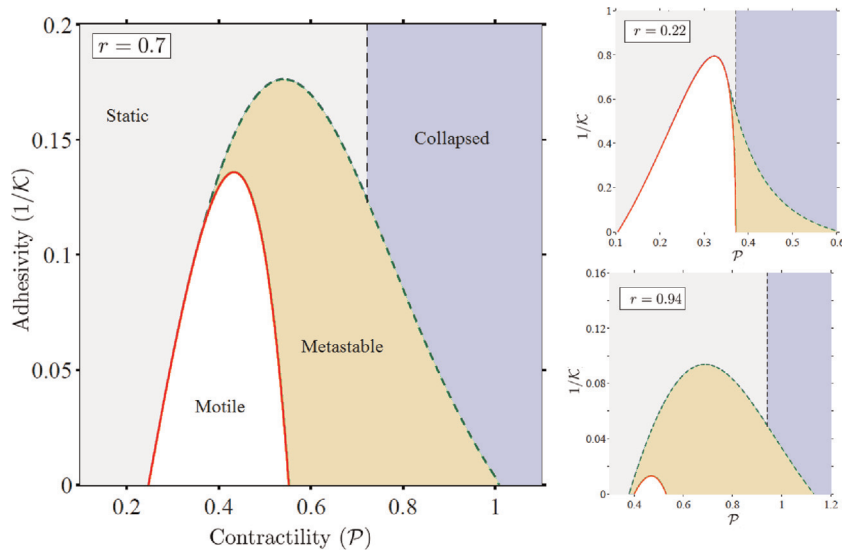


Fig. 21. Left: Phase diagram in the parameter plane (\mathcal{P} , $1/\mathcal{K}$) for the system (40) (with no length constraint). The parameter $Z/\mathcal{K} \approx 6 \times 10^{-3}$ is fixed at its experimental value. The solid (red) line indicates the motile bifurcation threshold for the branch D_1^+ (similar to Fig. 11(b)), while the dashed line bounding the metastability domain indicates the location of the turning points on the motile branch in the appropriate analog of Fig. 12(b). The dashed line separating static and collapsed configurations indicates the location of the turning point α in Fig. 7. Right: effects of a high (top) and low (bottom) concentration saturation thresholds. (For interpretation of the references to color in this figure caption, the reader is referred to the web version of this paper.)

concentrate and such autocatalytic amplification is the mechanism of the positive feedback in our model. The ensuing runaway is countered by diffusion of motors which penalizes creation of concentration gradients and thus plays the role of a negative feedback. When a critical contractility of motors is reached, the homogeneous distribution of motors becomes unstable. The contraction asymmetry then induces a flow of actin filaments towards the trailing edge thus producing frictional forces which propel the cell forward. The rebuilding of the balance between drift and diffusion leads to the formation of a pattern. Among various admissible patterns, whose number increases with contractility, the stable ones localize motors at the trailing edge as observed in experiments.

The proposed model provides an alternative *qualitative* explanation of the experiments of Verkhovsky et al. (1999) and Yam et al. (2007) that have been previously interpreted in terms of active polymerization inducing the growth of actin network (Blanch-Mercader and Casademunt, 2013). Most strikingly, the predictions of our model are also in *quantitative* agreement with experimental data, which is rather remarkable in view of a schematic nature of the model and the absence of fitting parameters.

In addition, the model captures a durotactic effect since the directional motion cannot be initiated if friction with the substrate is larger than a threshold value. We show that below this threshold, motile regimes exist in a finite range of contractility. This means that if the cell is already in motion, it can recover the symmetric (static) configuration either by *lowering* or by *increasing* the amount of operating motors. The predicted possibility of cell arrest under the increased contractility should be investigated in focused experiments.

We have also shown that when the contractility depends on the motor concentration nonlinearly, one can have a metastability range where both static and motile regimes are stable and can coexist. In this range of parameters a mechanical perturbation may be used to switch back and forth between static and dynamic regimes and reproducing such behavior in vivo presents an interesting challenge. This prediction of the model is particularly important in the context of collective cell motility (in tissues) where contact interactions are able to either initiate or terminate the motion (Abercrombie, 1967; Heckman, 2009; Treppe et al., 2009; Vedula et al., 2012).

Despite the overall success of the proposed model, it leaves several important questions unanswered. Thus, our focus on a one dimensional representation (projection) of the motility process obscured the detailed description of the reverse flow of actin monomers which we have replaced with an opaque jump process. Similarly, our desire to maximally limit the number of allowed activity mechanisms, forced us to assume that polymerization of actin monomers and their transport are equilibrium processes. The assumption of infinite compressibility of the cytoskeleton, which is behind the decoupling of the mass transport from the momentum balance, also remains highly questionable in the light of recent advances in the understanding of cytoskeletal constitutive response (Broedersz and MacKintosh, 2014; Pritchard et al., 2014). Finally, our schematic depiction of focal adhesions as passive frictional pads needs to be corrected by the account of the ATP driven integrin activity and the mechanical feedback from the binders to the cytoskeleton (Schwarz and Safran, 2013). These and other simplifying assumptions would have to be reconsidered in a richer setting with realistic flow geometry which will also open a way towards more adequate description of membrane (cortex) elasticity and will allow one to account for the polar nature of the gel (Marchetti et al., 2013).

Ultimately, the answer to the question whether the proposed simplified mechanism provides the *fundamental* explanation of motility initiation in keratocytes will depend on the extent to which the inclusion of all other related factors affects the main conclusions of the paper. A more thorough analysis will also open the way towards deeper understanding of the remarkable *efficiency* of the proposed mechanism of self-propulsion delivering almost optimal performance at a minimal metabolic cost (Recho et al., 2014).

Acknowledgments

P.R. acknowledges support from Monge Doctoral Fellowship at Ecole Polytechnique and a post doctoral grant from Pierre Gilles De Gennes Foundation. T.P. acknowledges support from the EPSRC Engineering Nonlinearity project EP/K003836/1. Authors thank D. Ambrosi, O. Du Roure, A. Grosberg, J.-F. Joanny and K. Kruse for insightful comments.

Appendix A. Analysis of nontrivial static solutions

Solutions of boundary value problem (29) correspond to closed trajectories on the phase plane (s, s') passing through the origin $(s = 0, s' = 0)$ and different types of such trajectories are illustrated in Fig. 22.

Depending on the position of a point in the parametric plane A, B , one can identify five different types of behavior:

1. If $A + B = 0$, then equation $W(r) = 0$ has one double root at $r=0$ and one single root (negative or positive) at $r = s_-$ (Case 3 in Fig. 22). The only solution is then the trivial one $s(u) = 0$ and $L = \hat{L}_\pm$.
2. If $A + B < 0$, then equation $W(r) = 0$ has three roots: $r=0$, $r = s_- < 0$ and $r = s_+ > 0$. This case corresponds to static branches labeled in Figs. 22, 7, 9(a) and (b) by numbers without a prime (Case 1 in Fig. 22). In this domain we find nontrivial static solutions with $0 \leq s(u) \leq s_+$. Different solutions correspond to different number (m) of sign changes for the function $s'(u)$ and different values of $L = 2m \int_0^{s_+} W(\sigma)^{-1/2} d\sigma$.
3. If

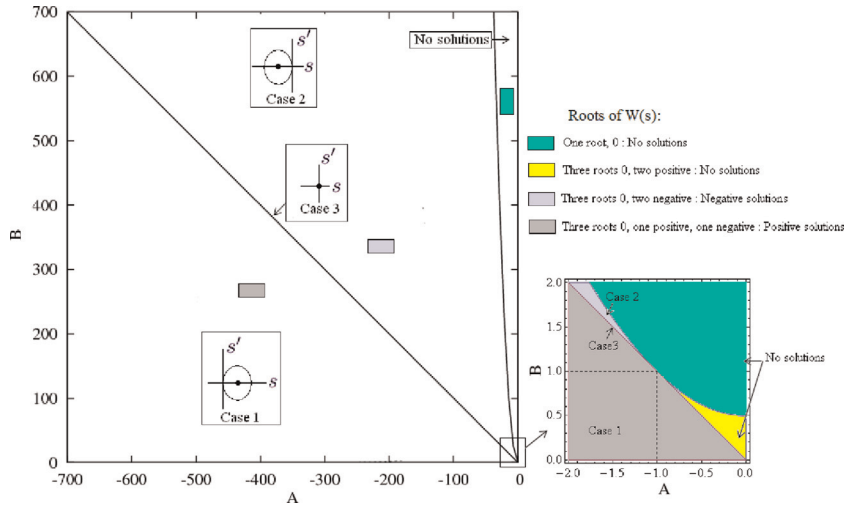


Fig. 22. (Color online) Phase diagram for the static solutions in the parameter space (A, B) . $A + B = 0$ line is the trivial (homogeneous) solution. In the bottom corner we show the blow up of the same diagram.

$$\begin{aligned} & A + B > 0 \\ & \{1 - \sqrt{A^2 - 2B + 1} < Be^{-\sqrt{A^2 - 2B + 1} + A + 1} \\ & A < -1 \end{aligned} \quad (\text{A.1})$$

then equation $W(r) = 0$ has three roots: $r=0$ and $r = s_- < 0$ and $r = s_+ < 0$ with, $s_+ > s_-$. This case corresponds to non-motile branches labeled in Figs. 22, 7, 9(a) and (b) by numbers with a prime (Case 2 in Fig. 22). In this domain, we find nontrivial static solutions with $s_- \leq s(u) \leq 0$. Again, different solutions correspond to different number of sign changes for the function $s'(u)$ and different values of $L = 2m \int_0^{s_+} W(\sigma)^{-1/2} d\sigma$.

4. If

$$\begin{aligned} & A + B > 0 \\ & \{1 - \sqrt{A^2 - 2B + 1} < Be^{-\sqrt{A^2 - 2B + 1} + A + 1} \\ & A > -1 \end{aligned} \quad (\text{A.2})$$

then equation $W(r) = 0$ has three roots: $r=0$ and $r = s_- > 0$ and $r = s_+ > 0$ with, $s_+ > s_-$ and there are no static solutions since there are no closed paths in the phase plane passing through the point $(0, 0)$.

5. If $1 - \sqrt{A^2 - 2B + 1} > Be^{-\sqrt{A^2 - 2B + 1} + A + 1}$, then equation $W(r) = 0$ has only one non-degenerate root at $u=0$. In this case there are no static solutions since again there are no closed paths in the phase plane.

Notice also that for the solutions described above the map between the two parameterizations (A, B) and $(\mathcal{K}, \mathcal{P})$ is explicit

$$\begin{aligned} \mathcal{K} &= A / \left(2m \int_0^{s_+} W(\sigma)^{-1/2} d\sigma - 1 \right) \\ \mathcal{K}\mathcal{P} &= 2m \int_0^{s_+} (\sigma - A) W(\sigma)^{-1/2} d\sigma. \end{aligned} \quad (\text{A.3})$$

Notice also all nontrivial static solutions bifurcate from the trivial branches in the sense that there are no detached solutions. Indeed, if a solution were detached, it would not pass through the origin (trivial solution) in the space (s, s') . But that would mean it cannot satisfies boundary conditions.

Appendix B. Analysis of the characteristic equation (39)

Eq. (39) has two families of solutions depending on whether ω is real or pure imaginary. In the first case, we denote $\omega_c \equiv |\omega| \geq 0$ whereas $\omega_c \equiv -|\omega| \leq 0$ in the second case.

$$\begin{aligned} 2[\cosh(\omega_c) - 1] + (\mathcal{Z}\omega_c^2/\hat{L}^2 - 1)\omega_c \sinh(\omega_c) &= 0 \quad \text{if } \omega_c^2 > 0, \\ 2[\cos(\omega_c) - 1] + (\mathcal{Z}\omega_c^2/\hat{L}^2 + 1)\omega_c \sin(\omega_c) &= 0 \quad \text{if } \omega_c^2 < 0. \end{aligned} \quad (\text{B.1})$$

Eqs. (B.1)₁ and (B.1)₂ need to be analyzed separately:

1. When $\omega_c^2 > 0$, Eq. (B.1)₁ has a unique solution only if $\hat{L}^2/\mathcal{Z} \geq 12$. It is given by the implicit formula

$$2 \tanh\left(\frac{\omega_c}{2}\right) = \left(1 - \frac{\mathcal{Z}}{\hat{L}^2} \omega_c^2\right) \omega_c.$$

The unstable eigen-vector can be written as

$$\begin{pmatrix} \delta L \\ \delta V \\ \delta S(u) \end{pmatrix} = \begin{pmatrix} 0 \\ 1 \\ \frac{\hat{L}^2}{\mathcal{Z} \omega_c^2 \cosh(\omega_c/2)} \{ \sinh[(u - 1/2)\omega_c] - (2u - 1) \sinh(\omega_c/2) \} \end{pmatrix}$$

Since $\delta V \neq 0$, this bifurcation leads to a motile configuration which we denote D_1 . In Fig. 23 the eigen-functions associated with the sub-branch D_1^+ bifurcating from the trivial solution \hat{L}_+ are illustrated for $\mathcal{Z} = 0.01$. As parameter \mathcal{Z} increases the exponential viscous boundary layers thicken. They fully disappear at $\mathcal{Z} = \hat{L}^2/12$ where the ‘hyperbolic’ eigen-vectors become ‘trigonometric’.

2. When $\omega_c^2 < 0$, Eq. (B.1)₂ has two sub-families of solutions:

(a) The first family can be written explicitly: $\omega_c = -2m\pi$ with $m \geq 1$. The unstable eigen-vector has the form

$$\begin{pmatrix} \delta L \\ \delta V \\ \delta S(u) \end{pmatrix} = \begin{pmatrix} 1 \\ 0 \\ \frac{(2\hat{L} - 1)(\mathcal{Z} \omega_c^2 + \hat{L}^2)}{\hat{L}^3(\hat{L} - 1)} [\cos(\omega_c u) - 1] \end{pmatrix}$$

Since $\delta V = 0$, the bifurcated branch describes the nontrivial static solutions S_m studied in Section 4. In Fig. 23 the eigen-functions associated with the sub-branch S_m^+ originating at the trivial solution \hat{L}_+ are illustrated for $\mathcal{Z} = 0.15$.

(b) The second family consists of a countable set of negative roots of Eq. (B.1)₂ given implicitly by

$$2 \tan\left(\frac{\omega_c}{2}\right) = \left(\frac{\mathcal{Z}}{\hat{L}^2} \omega_c^2 + 1\right) \omega_c \quad (\text{B.2})$$

The unstable eigen-vector is

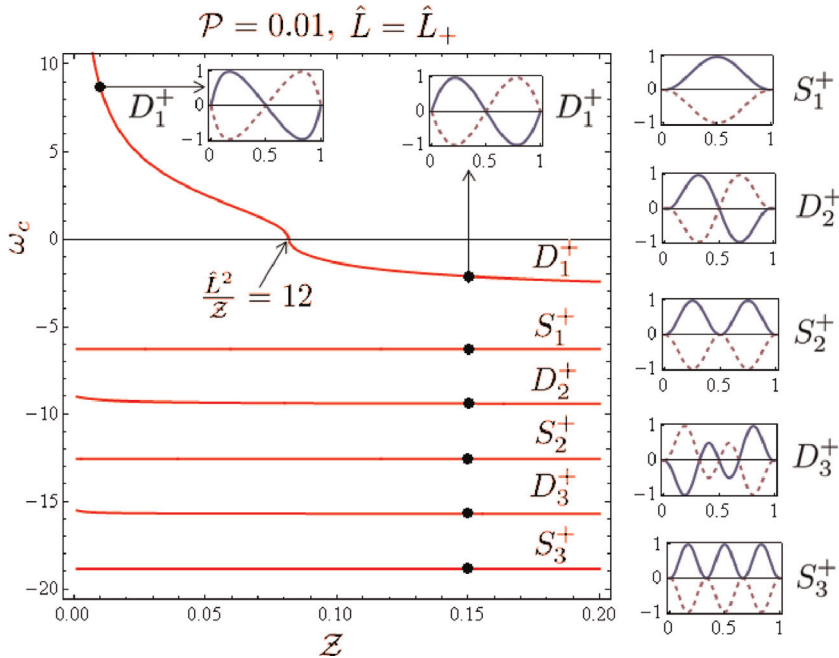


Fig. 23. Solution branches of the characteristic equation (B.1) as functions of \mathcal{Z} for the trivial static solution \hat{L}_+ ($\mathcal{P} = 0.01$). From (36), the locus of the bifurcation points are recovered and shown in Fig. 8. We refer to Fig. 9(a) for the label of bifurcation points. We represent in inserts the eigenfunctions δS related to D_1^+ , S_1^+ , D_2^+ , S_2^+ , D_3^+ , S_3^+ for $\mathcal{Z} = 0.15$ and the eigenfunction δS related to D_1^+ for $\mathcal{Z} = 0.01$. The eigenfunctions are normalized to 1; solid and dashed lines correspond to the two possible directions of the pitchfork bifurcation.

$$\begin{pmatrix} \delta L \\ \delta V \\ \delta s(u) \end{pmatrix} = \begin{pmatrix} 0 \\ 1 \\ \frac{-\hat{L}^2}{Z\omega_c^3 \cos(\omega_c/2)} \{ \sin[(u-1/2)\omega_c] - 2(u-1/2) \sin(\omega_c/2) \} \end{pmatrix}$$

It corresponds to motile branches because $\delta V \neq 0$. We denote this family by D_m . In Fig. 23 the eigen-functions associated with a subbranch D_m^+ originating at trivial solutions \hat{L}_+ are illustrated for $Z = 0.01$.

Appendix C. Normal forms

Normal form in \mathcal{K} : In terms of the normalized stress variable $r = s/L$ the original nonlinear problem can be written as

$$-Zr''(u) + L^2r(u) = \mathcal{K}\mathcal{P} \frac{e^{L(r(u)-Vu)}}{\int_0^1 e^{L(r(u)-Vu)} du} \quad \text{with } r(0) = r(1) = 0, \quad r'(0) = r'(1) = V. \quad (\text{C.1})$$

Assume that ϵ is a small parameter and expand the solution of (C.1) around a bifurcation point up to third order

$$r = 0 + \epsilon \hat{r} + \epsilon^2 \hat{r}^2/2 + \epsilon^3 \hat{r}^3/6 + o(\epsilon^3), \quad V = 0 + \epsilon \hat{V} + \epsilon^2 \hat{V}^2/2 + \epsilon^3 \hat{V}^3/6 + o(\epsilon^3), \quad L = \hat{L} + \epsilon \hat{L}^1 + \epsilon^2 \hat{L}^2/2 + \epsilon^3 \hat{L}^3/6 + o(\epsilon^3).$$

Assume that the bifurcation parameter \mathcal{K} and therefore

$$\mathcal{K} = \hat{\mathcal{K}} + \epsilon \hat{\mathcal{K}}^1 + \epsilon^2 \hat{\mathcal{K}}^2/2 + \epsilon^3 \hat{\mathcal{K}}^3/6 + o(\epsilon^3),$$

where $\hat{\mathcal{K}}$ is the bifurcation point. These expressions are then inserted into Eq. (C.1). Separating different orders of ϵ we obtain three differential equations

$$O(1), \quad \mathbb{L}(\hat{r}, \hat{L}, \hat{V}) = 0, \quad (\text{C.2})$$

$$O(2), \quad \mathbb{L}(\hat{r}^2, \hat{L}, \hat{V}) = \hat{\mathcal{K}} \mathbb{P}_0(\hat{r}, \hat{L}, \hat{V}) + \hat{\mathcal{K}}^1 \mathbb{P}_1(\hat{r}, \hat{L}, \hat{V}), \quad (\text{C.3})$$

$$O(3), \quad \mathbb{L}(\hat{r}^3, \hat{L}, \hat{V}) = \hat{\mathcal{K}} \mathbb{Q}_0(\hat{r}, \hat{L}, \hat{V}) + \hat{\mathcal{K}}^1 \mathbb{Q}_1(\hat{r}, \hat{L}, \hat{V}) + \hat{\mathcal{K}}^2 \mathbb{Q}_2(\hat{r}, \hat{L}, \hat{V}) + \hat{\mathcal{K}}^3 \mathbb{Q}_3(\hat{r}, \hat{L}, \hat{V}), \quad (\text{C.4})$$

where \mathbb{L} is the linear operator already introduced in the stability analysis, see (34):

$$\mathbb{L}(r, L, V) := r''(u) - \omega^2 r(u) + \frac{\left(u - \frac{1}{2}\right) \left(\omega^2 Z - \hat{L}^2\right)}{Z} V + \frac{(2\hat{L} - 1) \omega^2 \left(\omega^2 Z - \hat{L}^2\right)}{(\hat{L} - 1) \hat{L}^4} L$$

and $\mathbb{P}_0, \mathbb{P}_1, \mathbb{Q}_0, \mathbb{Q}_1$ and \mathbb{Q}_2 are known non-linear operators. The boundary conditions remain the same at all orders i :

$$r^i(0) = r^i(1) = 0, \quad r'^i(0) = r'^i(1) = V$$

In the leading order, we obtain the results already reported in Section 5 including the eigenvalue $\hat{\mathcal{K}}$ and the eigenfunction $\hat{r}(u), \hat{L}, \hat{V}$. To have a nontrivial solution in the next order, the right-hand side of Eq. (C.3) must be orthogonal to the kernel of the dual of \mathbb{L} (for the L^2 scalar product). In the $(G, C_2, \delta L, \delta V)$ space, see Section 5, this means orthogonality to the kernel of the transpose of matrix (38). The resulting linear scalar equation determines the value of \mathcal{K} . When this value vanishes, higher orders must be considered in a similar way. We summarize below the main results obtained by implementing this procedure.

1. *Static branches* result from transcritical bifurcations. For the m th branch we have

$$\hat{\mathcal{K}}^1 = (\hat{L}^2 - 4m^2\pi^2 Z)/[\hat{L}^3(\hat{L} - 1)]$$

2. *Motile branches* all correspond to pitchfork bifurcations with $\hat{\mathcal{K}} = 0$. They can be either subcritical or supercritical depending on the sign of

$$\begin{aligned}
\mathcal{K}^2 = & ((2\hat{L} - 1)\hat{L}^{14} (3\omega^2 + 770) + 2\hat{L}^{12} \mathcal{Z} (3(8 - 11\hat{L})\omega^4 + 1415(1 - 2\hat{L})\omega^2 + 4620(1 - 2\hat{L})) + 3\hat{L}^{10} \omega^2 \mathcal{Z}^2 (40\hat{L} (\omega^4 + 61\omega \\
& + 374) - 31\omega^4 - 1340\omega^2 - 7480) + 2\hat{L}^8 \omega^4 \mathcal{Z}^3 (4\hat{L} (6\omega^4 + 89\omega^2 - 3150) - 9\omega^4 + 50\omega^2 + 7380) + \hat{L}^6 \omega^6 \mathcal{Z}^4 (-2\hat{L} (165\omega^4 \\
& + 6502\omega^2 + 23160) + 195\omega^4 + 6574\omega^2 + 22440) + 6\hat{L}^4 \omega^8 \mathcal{Z}^5 ((61\hat{L} - 34)\omega^4 + (2622\hat{L} - 1339)\omega^2 + 7072(2\hat{L} - 1)) \\
& + \hat{L}^2 \omega^{10} \mathcal{Z}^6 (3(31 - 60\hat{L})\omega^4 + 4264(1 - 2\hat{L})\omega^2 - 28224(2\hat{L} - 1)) + 2(2\hat{L} - 1)\omega^{12} (9\omega^4 + 472\omega^2 + 3456) \mathcal{Z}^7) \\
& \left(144(\hat{L} - 1)(2\hat{L} - 1)\omega^8 \mathcal{Z}^3 (\hat{L}^2 - \omega^2 \mathcal{Z}) \left(\hat{L}^4 - 2\hat{L}^2 (\omega^2 + 6) \mathcal{Z} + \omega^4 \mathcal{Z}^2 \right) \right)^{-1}
\end{aligned} \quad (C.5)$$

In Fig. 24(b) we illustrate the function $\mathcal{K}^2(\mathcal{P})$ for the first motile branches D_1^- and D_1^+ . As $\mathcal{K}^2 \geq 0$ for all values of the activity parameter \mathcal{P} , the motile branch D_1^+ always bifurcates from the static branch in a supercritical (pitchfork) manner. In contrast, the motile branch D_1^- can bifurcate either supercritically or subcritically depending on the value of \mathcal{P} . When \mathcal{P} is larger than a threshold value \mathcal{P}_s , the coefficient \mathcal{K} changes sign and becomes negative indicating a subcritical character of the bifurcation on the \hat{L}_- static branch.

Normal form in \mathcal{P} : We now consider \mathcal{P} as the bifurcational parameter. The derivation of the normal form in this case is more complex because the homogeneous static solution $\hat{L}(\mathcal{P})$ is a multivalued function of \mathcal{P} (see Fig. 6). One can circumvent the difficulty by introducing a new variable

$$J = L(L - 1) + \mathcal{P}. \quad (C.6)$$

Then the boundary value problem (C.1) takes the form

$$-\mathcal{Z}r''(u) + L^2r(u) = \mathcal{K}[J - L(L - 1)] \frac{e^{L(r(u) - Vu)}}{\int_0^1 e^{L(r(u) - Vu)} du} \quad \text{with } r(0) = r(1) = 0, \quad r'(0) = r'(1) = V.$$

whose trivial solution is $(J, V, r) = (0, 0, 0)$. In this formulation J, V and $r(u)$ are unknowns while the length L is the bifurcation parameter. The regular expansions near the homogeneous state give

$$\begin{aligned}
r &= \epsilon r^1 + \epsilon^2 r^2/2 + \epsilon^3 r^3/6 + o(\epsilon^3), \quad V = \epsilon V^1 + \epsilon^2 V^2/2 + \epsilon^3 V^3/6 + o(\epsilon^3), \quad J = \epsilon J^1 + \epsilon^2 J^2/2 + \epsilon^3 J^3/6 + o(\epsilon^3), \\
L &= \hat{L}^0 + \epsilon \hat{L}^1 + \epsilon^2 \hat{L}^2/2 + \epsilon^3 \hat{L}^3/6 + o(\epsilon^3).
\end{aligned}$$

Distinguishing the static and motile branches as before, we obtain the following results:

1. *Static branches* are all found to be transcritical bifurcation. For the m th branch, we have $\mathcal{P} = \hat{\mathcal{P}}^0 + \epsilon \hat{\mathcal{P}}^1 + o(\epsilon)$ where

$$\hat{\mathcal{P}}^0 = -\hat{L}^0(\hat{L}^0 - 1), \quad \hat{\mathcal{P}}^1 = 1 - (2\hat{L}^0 - 1)\hat{L}^1.$$

and \hat{L}^0 is a solution of the cubic equation

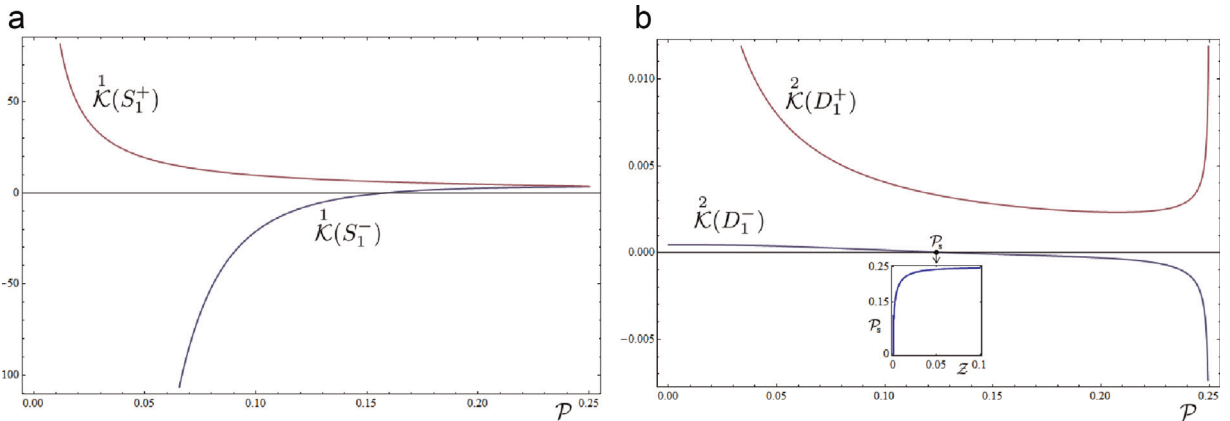


Fig. 24. (a) Values of \mathcal{K}^1 for the S_1^+ and S_1^- branches as functions of parameter \mathcal{P} for $\mathcal{Z} = 0.001$. The point where $\mathcal{K} = 0$ along the \hat{L}_- static branch indicates a nature change of the motile pitchfork bifurcation from supercritical to subcritical pitchfork. The parameter dependence of such a point is represented as a function of $\mathcal{P} = \mathcal{P}_s(\mathcal{Z})$ in the inset.

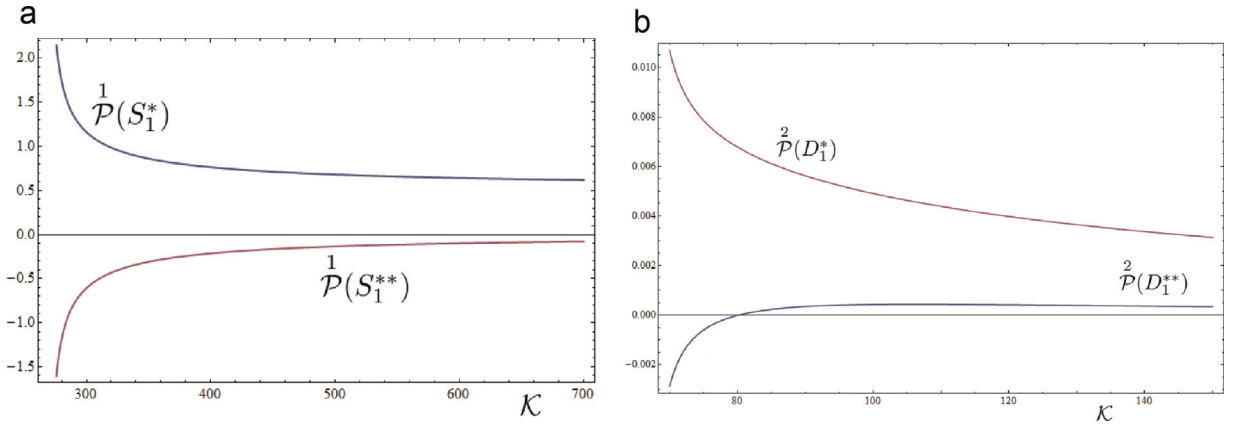


Fig. 25. (a) Values of \mathcal{P}^1 for the first static branch as a function of parameter \mathcal{K} for a fixed $\mathcal{Z} = 1$. (b) Values of \mathcal{P}^2 for the first motile branch ($\mathcal{Z} = 1$).

$$-\mathcal{K}(L)^2(L-1) = \mathcal{Z}4\pi^2 m^2 + (L)^2.$$

In this equation only two roots corresponding to S_m^* (the smaller) and to S_m^{**} (the larger) are in the range $[0, 1]$. In Fig. 25 (a), we illustrate the behavior of the function $\mathcal{P}(\mathcal{K})$ for the branches S_1^* and S_1^{**} .

2. *Motile branches* result from pitchfork bifurcations that can be either supercritical or subcritical with

$$\mathcal{P} = \mathcal{P}^0 + \epsilon^2 \mathcal{P}^2/2 + o(\epsilon^2).$$

The coefficients in this expansion can be written in the form

$$\mathcal{P}^0 = -\frac{0}{L}(L-1) \quad \text{and} \quad \mathcal{P}^2 = \frac{2}{J} - \frac{0}{(2L-1)L},$$

where

$$\frac{2}{J} = \frac{60L\mathcal{Z} - \mathcal{K}(L-1)(L)^3(\mathcal{K}(L-1) - 4)}{24\mathcal{K}(\mathcal{K}(L-1) + 1)^2}.$$

The length L can be found from the system of equations

$$\begin{aligned} -\mathcal{K}(L)^2(L-1) &= -\mathcal{Z}\omega^2 + (L)^2 \\ \tanh(\omega/2) &= (\omega/2)(1 - \mathcal{Z}\omega^2/(L)^2) \end{aligned}$$

Again, two roots are in the interval $[0, 1]$: the smaller one belongs to the branch D_m^* and the larger one to the branch D_m^{**} . In Fig. 25(b), we illustrate the function $\mathcal{P}(\mathcal{K})$ for $m=1$. The bifurcation from the static homogeneous solution with longer length is always supercritical as $\mathcal{P}(D_1^*) > 0$. Instead, the bifurcation from the static homogeneous solution with smaller length can change from subcritical ($\mathcal{P} \leq 0$) to supercritical ($\mathcal{P} \geq 0$).

Appendix D. Normal form for the stiff limit

In the study of (41) we closely follow the procedure developed in Section 5. In essence, the results are exactly the same for fixed $\hat{L} = 1$ and the product $\mathcal{K}\mathcal{P}$ replaced by λ with only one homogeneous state ($s(y) = 0$, $V=0$ and $s_0 = \phi(r)/r$) and where δs_0 replace δL . As a result, there is an infinite sequence of bifurcations branching from the now unique homogeneous state. We shall only focus on the stable attractor of the problem, namely, the homogeneous solution before the D_1 bifurcation and the first motile branch after.

The critical value of the bifurcation parameter λ_c corresponding to the case when a homogeneous static solution becomes linearly unstable is given by the formula $\lambda_c = (1+r)^2(1 - \mathcal{Z}\omega - c^2)$ where ω_c is a root of the equation $\tanh(\omega_c/2) = \omega_c(1 - \mathcal{Z}\omega_c^2)/2$ with the smallest absolute value. We then proceed to the next order developing a regular expansions close to the bifurcation point

$$\begin{cases} s = 0 + \epsilon s^1 + \epsilon^2 s^2/2 + \epsilon^3 s^3/6 + o(\epsilon^3) \\ V = 0 + \epsilon V^1 + \epsilon^2 V^2/2 + \epsilon^3 V^3/6 + o(\epsilon^3) \\ s_0 = \Phi(r)/r + \epsilon s_0^1 + \epsilon^2 s_0^2/2 + \epsilon^3 s_0^3/6 + o(\epsilon^3). \end{cases}$$

Similar expansion for the bifurcation has the form

$$\lambda = \lambda_c + \epsilon \lambda^1 + \epsilon^2 \lambda^2/2 + \epsilon^3 \lambda^3/6 + o(\epsilon^3).$$

For the first motile branch one finds that $\lambda^1 = 0$, indicating a pitchfork bifurcation.

Below we show that this bifurcation can change from supercritical to subcritical depending on the value of the dimensionless parameter r . Assuming without loss of generality that $V = V = 1$, we obtain

$$\lambda^2 = \frac{(\omega^2 \mathcal{Z} - 1)(Ar^2 + Br + C)}{144\omega^8 \mathcal{Z}^3 (\omega^4 \mathcal{Z}^2 - 2(\omega^2 + 6)\mathcal{Z} + 1)}$$

where

$$A = 30\omega^{12}\mathcal{Z}^5 - 123\omega^{10}\mathcal{Z}^4 + 6\omega^8(35 - 164\mathcal{Z})\mathcal{Z}^3 + 2\omega^6\mathcal{Z}^2(1073\mathcal{Z} - 84) + 6\omega^4\mathcal{Z}(1440\mathcal{Z}^2 - 155\mathcal{Z} + 8)$$

$$+ 3\omega^2(1320\mathcal{Z}^2 - 430\mathcal{Z} + 1) - 9240\mathcal{Z} + 770$$

$$B = -2(21\omega^{12}\mathcal{Z}^5 - 87\omega^{10}\mathcal{Z}^4 + 4\omega^8(39 - 173\mathcal{Z})\mathcal{Z}^3 + 2\omega^6\mathcal{Z}^2(707\mathcal{Z} - 66) + 3\omega^4\mathcal{Z}(1440\mathcal{Z}^2 - 210\mathcal{Z} + 13)$$

$$+ \omega^2(2280\mathcal{Z}^2 - 1150\mathcal{Z} + 3) - 9240\mathcal{Z} + 770)$$

$$C = -6\omega^{12}\mathcal{Z}^5 + 21\omega^{10}\mathcal{Z}^4 + 6\omega^8\mathcal{Z}^3(28\mathcal{Z} - 5) + 2\omega^6(12 - 79\mathcal{Z})\mathcal{Z}^2 + 6\omega^4\mathcal{Z}(85\mathcal{Z} - 2) + 3\omega^2(1320\mathcal{Z}^2 - 430\mathcal{Z} + 1)$$

$$- 9240\mathcal{Z} + 770$$

these expressions show that there exists a critical value r_c of the parameter r such that the bifurcation is supercritical (i.e. $\lambda^2 \leq 0$) for $r \leq r_c$. This regime corresponds to a state where contraction is proportional to concentration of motors. For $r \geq r_c$, the pitchfork bifurcation is subcritical (i.e. $\lambda^2 \geq 0$) and the regime is characterized by a contraction which saturates into the plateau. We plot in Fig. 26 the value of λ^2 as a function of r for a fixed $\mathcal{Z} = 1$ and in inset the value $r_c(\mathcal{Z})$. When $\mathcal{Z} \rightarrow 0$, $r_c \rightarrow 2$ and when $\mathcal{Z} \rightarrow \infty$, $r_c \rightarrow (7 + \sqrt{69})/10$.

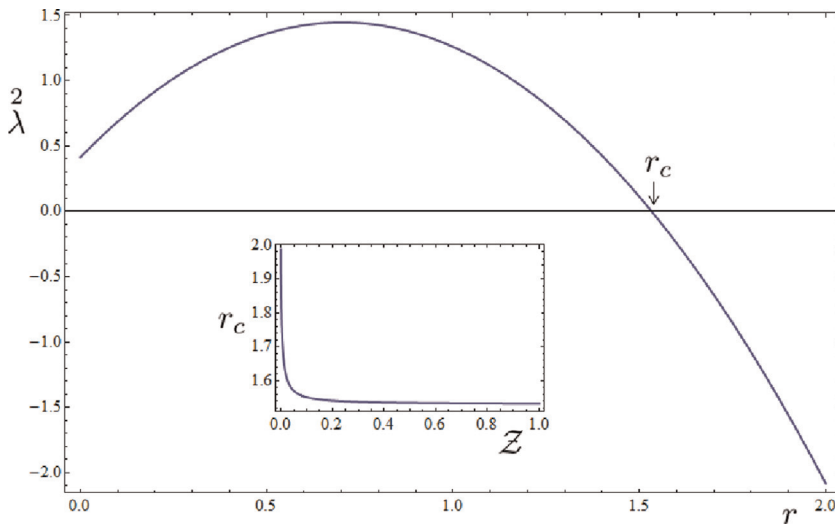


Fig. 26. Parameter λ^2 characterizing the structure of the static to motile bifurcation in the case of non-linear contraction law.

References

- Abercrombie, M., 1967. Contact inhibition: the phenomenon and its biological implications. *Natl. Cancer Inst. Monogr.* 26, 249.
- Abercrombie, M., 1980. Croonian lecture, 1978 – crawling movement of metazoan cells. *Proc. R. Soc. Lond. Ser. B–Biol. Sci.* 207, 129.
- Adler, Y., Givli, S., 2013. Closing the loop: lamellipodia dynamics from the perspective of front propagation. *Phys. Rev. E* 88, 042708, <http://dx.doi.org/10.1103/PhysRevE.88.042708>. URL: (<http://link.aps.org/doi/10.1103/PhysRevE.88.042708>).
- Ahmadi, A., Marchetti, M.C., Liverpool, T.B., 2006. Hydrodynamics of isotropic and liquid crystalline active polymer solutions. *Phys. Rev. E* 74, 061913, <http://dx.doi.org/10.1103/PhysRevE.74.061913>. URL: (<http://link.aps.org/doi/10.1103/PhysRevE.74.061913>).
- Bruce Alberts, Alexander Johnson, Julian Lewis, Martin Raff, Keith Roberts, Peter Walter, 2002. *Molecular Biology of the Cell*, 4th ed. Garland Science Taylor & Francis Group, New York ISBN-10: 0-8153-3218-1 ISBN-10: 0-8153-4072-9.
- Alt, W., Dembo, M., 1999. Cytoplasm dynamics and cell motion: two-phase flow models. *Math. Biosci.* 156, 207–228, [http://dx.doi.org/10.1016/S0025-5564\(98\)10067-6](http://dx.doi.org/10.1016/S0025-5564(98)10067-6). URL: (<http://www.sciencedirect.com/science/article/pii/S0025556498100676>).
- Altschuler, S.J., Angenent, S.B., Wang, Y., Wu, L.F., 2008. On the spontaneous emergence of cell polarity. *Nature* 454, 886–889, <http://dx.doi.org/10.1038/nature07119>.
- Amazigo, J.C., Budiansky, B., Carrier, G.F., 1970. Asymptotic analyses of the buckling of imperfect columns on nonlinear elastic foundations. *Int. J. Solids Struct.* 6, 1341–1356.
- Banerjee, S., Marchetti, M.C., 2011. Substrate rigidity deforms and polarizes active gels. *Europhys. Lett.* 96, 28003. URL: (<http://stacks.iop.org/0295-5075/96/i=2/a=28003>).
- Banerjee, S., Marchetti, M.C., 2012. Contractile stresses in cohesive cell layers on finite-thickness substrates. *Phys. Rev. Lett.* 109, 108101, <http://dx.doi.org/10.1103/PhysRevLett.109.108101>. URL: (<http://link.aps.org/doi/10.1103/PhysRevLett.109.108101>).
- Barnhart, E., Lee, K.C., Allen, G.M., Theriot, J.A., Mogilner, A., 2015. Balance between cell–substrate adhesion and myosin contraction determines the frequency of motility initiation in fish keratocytes. *Proc. Natl. Acad. Sci.* 201417257.
- Barnhart, E.L., Allen, G.M., Jülicher, F., Theriot, J.A., 2010. Bipedal locomotion in crawling cells. *Biophys. J.* 98, 933–942, <http://dx.doi.org/10.1016/j.bpj.2009.10.058>.
- Barnhart, E.L., Lee, K.C., Keren, K., Mogilner, A., Theriot, J.A., 2011. An adhesion-dependent switch between mechanisms that determine motile cell shape. *PLoS Biol.* 9, e1001059, <http://dx.doi.org/10.1371/journal.pbio.1001059>. URL: (<http://dx.doi.org/10.1371%2Fjournal.pbio.1001059>).
- Bell, P., 1984. Cell behavior – a tribute to Abercrombie, Michael – Bellairs, R., Curtis, A., Dunn, G. *Am. Sci.* 72, 88–89.
- Bellairs, R., 2000. Michael Abercrombie (1912–1979). *Int. J. Dev. Biol.* 44, 23–28.
- Bernheim-Groswasser, A., Prost, J., Sykes, C., 2005. Mechanism of actin-based motility: a dynamic state diagram. *Biophys. J.* 89, 1411–1419, <http://dx.doi.org/10.1529/biophysj.104.055822>.
- Blanch-Mercader, C., Casademunt, J., 2013. Spontaneous motility of actin lamellar fragments. *Phys. Rev. Lett.* 110, 078102, <http://dx.doi.org/10.1103/PhysRevLett.110.078102>. URL: (<http://link.aps.org/doi/10.1103/PhysRevLett.110.078102>).
- Bois, J.S., Jülicher, F., Grill, S.W., 2011. Pattern formation in active fluids. *Phys. Rev. Lett.* 106, 028103, <http://dx.doi.org/10.1103/PhysRevLett.106.028103>. URL: (<http://link.aps.org/doi/10.1103/PhysRevLett.106.028103>).
- Bray, D., 2000. *Cell Movements: From Molecules to Motility*, 2nd ed. Garland Science ISBN: 9780815332824.
- Broedersz, C.P., MacKintosh, F.C., 2014. Modeling semiflexible polymer networks. *Rev. Mod. Phys.* 86, 995–1036, <http://dx.doi.org/10.1103/RevModPhys.86.995>. URL: (<http://link.aps.org/doi/10.1103/RevModPhys.86.995>).
- Caglioti, E., Lions, P.L., Marchioro, C., Pulvirenti, M., 1992. A special class of stationary flows for two-dimensional Euler equations: a statistical mechanics description. *Commun. Math. Phys.* 143, URL: (<http://dx.doi.org/10.1007/BF02099262>).
- Callan-Jones, A., Voituriez, R., 2013. Active gel model of amoeboid cell motility. *New J. Phys.* 15, 025022.
- Callan-Jones, A.C., Joanny, J.F., Prost, J., 2008. Viscous-fingering-like instability of cell fragments. *Phys. Rev. Lett.* 100, 258106, <http://dx.doi.org/10.1103/PhysRevLett.100.258106>. URL: (<http://link.aps.org/doi/10.1103/PhysRevLett.100.258106>).
- Callan-Jones, A.C., Jülicher, F., 2011. Hydrodynamics of active permeating gels. *New J. Phys.* 13, <http://dx.doi.org/10.1088/1367-2630/13/9/093027>.
- Calvez, V., Meunier, N., Voituriez, R., 2010. A one-dimensional Keller–Segel equation with a drift issued from the boundary. *C. R. Math.* 348, 629–634, <http://dx.doi.org/10.1016/j.crma.2010.04.009>. URL: (<http://www.sciencedirect.com/science/article/pii/S1631073X1000124X>).
- Campas, O., Mahadevan, L., Joanny, J.F., 2012. Actin network growth under load. *Biophys. J.* 102, 1049–1058, <http://dx.doi.org/10.1016/j.bpj.2012.01.030>.
- Carlsson, A.E., Sept, D., 2008. Mathematical modeling of cell migration. In: *Biophysical Tools for Biologists: In Vitro Techniques*, vol. 1. Elsevier Academic Press Inc., USA. *Methods in Cell Biology*, vol. 84, pp. 911 +, [http://dx.doi.org/10.1016/S0091-679X\(07\)84029-5](http://dx.doi.org/10.1016/S0091-679X(07)84029-5).
- Carr, J., Pego, R.L., 1989. Metastable patterns in solutions of $u_t = e^2 u_{xx} - f(u)$. *Commun. Pure Appl. Math.* 42, 523–576, <http://dx.doi.org/10.1002/cpa.3160420502>.
- Chuin Chuan Chen, Chang-Shou Lin, On the symmetry of blowup solutions to a mean field equation, *Annales de l'Institut Henri Poincaré (C) Non Linear Analysis*, Volume 18, Issue 3, May–June 2001, Pages 271–296, ISSN 0294-1449, [http://dx.doi.org/10.1016/S0294-1449\(00\)00060-3](http://dx.doi.org/10.1016/S0294-1449(00)00060-3).
- Cox, B.N., Smith, D.W., 2014. On strain and stress in living cells. *J. Mech. Phys. Solids* 71, 239–252, <http://dx.doi.org/10.1016/j.jmps.2014.07.001>. URL: (<http://www.sciencedirect.com/science/article/pii/S0022509614001392>).
- Csucs, G., Quirin, K., Danuser, G., 2007. Locomotion of fish epidermal keratocytes on spatially selective adhesion patterns. *Cell Motil. Cytoskeleton* 64, 856–867, <http://dx.doi.org/10.1002/cm.20230>.
- Dawes, A.T., Ermentrout, G.B., Cytrynbaum, E.N., Edelstein-Keshet, L., 2006. Actin filament branching and protrusion velocity in a simple 1D model of a motile cell. *J. Theor. Biol.* 242, 265–279, <http://dx.doi.org/10.1016/j.jtbi.2006.02.017>.
- Deshpande, V.S., Mrksich, M., McMeeking, R.M., Evans, A.G., 2008. A bio-mechanical model for coupling cell contractility with focal adhesion formation. *J. Mech. Phys. Solids* 56, 1484–1510, <http://dx.doi.org/10.1016/j.jmps.2007.08.006>.
- DeSimone, A., Tatone, A., 2012. Crawling motility through the analysis of model locomotors: two case studies. *Eur. Phys. J. E* 35, 1–8, <http://dx.doi.org/10.1140/epje/i2012-12085-x>.
- DiMilla, P., Barbee, K., Lauffenburger, D., 1991. Mathematical-model for the effects of adhesion and mechanics on cell-migration speed. *Biophys. J.* 60, 15–37.
- Doedel, E., Champneys, A., Dercole, F., Fairgrieve, T., Kuznetsov, Y.A., Oldeman, B., Paffenroth, R., Sandstede, B., Wang, X., Zhang, C., 2007. Auto-07p. Continuation and bifurcation software for ordinary differential equations.
- Dobrovinski, K., Kruse, K., 2007. Self-organization of treadmilling filaments. *Phys. Rev. Lett.* 99, 228104, <http://dx.doi.org/10.1103/PhysRevLett.99.228104>. URL: (<http://link.aps.org/doi/10.1103/PhysRevLett.99.228104>).
- Dobrovinski, K., Kruse, K., 2010. Self-organization in systems of treadmilling filaments. *Eur. Phys. J. E* 31, 95–104, <http://dx.doi.org/10.1140/epje/i2010-10548-8>.
- Dobrovinski, K., Kruse, K., 2011. Cell motility resulting from spontaneous polymerization waves. *Phys. Rev. Lett.* 107, 258103, <http://dx.doi.org/10.1103/PhysRevLett.107.258103>. URL: (<http://link.aps.org/doi/10.1103/PhysRevLett.107.258103>).
- Du, X., Dobrovinski, K., Osterfield, M., 2012. Self-organized cell motility from motor-filament interactions. *Biophys. J.* 102, 1738–1745, <http://dx.doi.org/10.1016/j.bpj.2012.03.052>. URL: (<http://www.sciencedirect.com/science/article/pii/S0006349512003931>).
- Jocelyn Étienne, Jonathan Fouchard, Démosthène Mitrossilis, Nathalie Buff, Pauline Durand-Smet, and Atef Asnacios, Cells as liquid motors: Mechanosensitivity emerges from collective dynamics of actomyosin cortex, *PNAS* 2015 112 (9) 2740–2745, <http://dx.doi.org/10.1073/pnas.1417113112>.
- Fournier, M.F., Sauser, R., Ambrosi, D., Meister, J.J., Verkhovsky, A.B., 2010. Force transmission in migrating cells. *J. Cell Biol.* 188, 287–297, <http://dx.doi.org/10.1083/jcb.200906139>.
- Gao, H., Qian, J., Chen, B., 2011. Probing mechanical principles of focal contacts in cell-matrix adhesion with a coupled stochastic-elastic modelling framework. *J. R. Soc. Interface* 8, 1217–1232, <http://dx.doi.org/10.1098/rsif.2011.0157>.

- Gardel, M.L., Sabass, B., Ji, L., Danuser, G., Schwarz, U.S., Waterman, C.M., 2008. Traction stress in focal adhesions correlates biphasically with actin retrograde flow speed. *J. Cell Biol.* 183, 999–1005, <http://dx.doi.org/10.1083/jcb.200810060>.
- Gardel, M.L., Schneider, I.C., Aratyn-Schaus, Y., Waterman, C.M., 2010. Mechanical integration of actin and adhesion dynamics in cell migration. In: Schekman, R., Goldstein, L., Lehmann, R. (Eds.), *Annual Review of Cell and Developmental Biology*. Annual Review of Cell and Developmental Biology, vol. 26, pp. 315–333. <http://dx.doi.org/10.1146/annurev.cellbio.011209.122036>.
- Giomi, L., DeSimone, A., 2014. Spontaneous division and motility in active nematic droplets. *Phys. Rev. Lett.* 112, 147802, <http://dx.doi.org/10.1103/PhysRevLett.112.147802>. URL: <http://link.aps.org/doi/10.1103/PhysRevLett.112.147802>.
- Gladioli, F., Grossi, M., Ohtsuka, H., Suzuki, T., 2012. Morse indices of multiple blow-up solutions to the two-dimensional gel'fand problem. arXiv preprint [arXiv:1210.1373](http://arxiv.org/abs/1210.1373).
- Hawkins, R.J., Bénichou, O., Piel, M., Voituriez, R., 2009a. Rebuilding cytoskeleton roads: active-transport-induced polarization of cells. *Phys. Rev. E (Stat. Nonlinear Soft Matter Phys.)* 80, 040903+, <http://dx.doi.org/10.1103/PhysRevE.80.040903>.
- Hawkins, R.J., Piel, M., Faure-Andre, G., Lennon-Dumenil, A.M., Joanny, J.F., Prost, J., Voituriez, R., 2009b. Pushing off the walls: a mechanism of cell motility in confinement. *Phys. Rev. Lett.* 102, <http://dx.doi.org/10.1103/PhysRevLett.102.058103>.
- Hawkins, R.J., Poincloux, R., Benichou, O., Piel, M., Chavrier, P., Voituriez, R., 2011. Spontaneous contractility-mediated cortical flow generates cell migration in three-dimensional environments. *Biophys. J.* 101, 1041–1045, <http://dx.doi.org/10.1016/j.bpj.2011.07.038>.
- Hawkins, R.J., Voituriez, R., 2010. Mechanisms of cell motion in confined geometries. *Math. Modell. Nat. Phenom.* 5, 84–105, <http://dx.doi.org/10.1051/mmnp/20105104>.
- Heckman, C.A., 2009. Contact inhibition revisited. *J. Cell. Physiol.* 220, 574–575, <http://dx.doi.org/10.1002/jcp.21775>.
- Herant, M., Dembo, M., 2010. Form and function in cell motility: from fibroblasts to keratocytes. *Biophys. J.* 98, 1408–1417, <http://dx.doi.org/10.1016/j.bpj.2009.12.4303>.
- Hodge, N., Papadopoulos, P., 2012. Continuum modeling and numerical simulation of cell motility. *J. Math. Biol.* 64, 1253–1279.
- Howard, J., Grill, S.W., Bois, J.S., 2011. Turing's next steps: the mechanochemical basis of morphogenesis. *Nat. Rev. Mol. Cell Biol.* 12, 392–398, <http://dx.doi.org/10.1038/nrm3120>.
- Hur, E.M., Yang, L.H., Kim, D.H., Byun, J., Xu, W.L., Nicovich, P.R., Cheong, R., Levchenko, A., Thakor, N., Zhou, F.Q., et al., 2011. Engineering neuronal growth cones to promote axon regeneration over inhibitory molecules. *Proc. Natl. Acad. Sci.* 108, 5057–5062.
- Jilkine, A., Edelstein-Keshet, L., 2011. A comparison of mathematical models for polarization of single eukaryotic cells in response to guided cues. *PLoS Comput. Biol.* 7, e1001121, <http://dx.doi.org/10.1371/journal.pcbi.1001121>. URL: <http://dx.doi.org/10.1371%2Fjournal.pcbi.1001121>.
- Joanny, J.F., Jülicher, F., Kruse, K., Prost, J., 2007. Hydrodynamic theory for multi-component active polar gels. *New J. Phys.* 9, <http://dx.doi.org/10.1088/1367-2630/9/11/422>.
- Joanny, J.F., Prost, J., 2011. Constructing tools for the description of cell dynamics. In: Duplantier, B., Rivasseau, V. (Eds.), *Biological Physics: Poincare Seminar 2009*, Commissariat Energie Atomique, Div Sci Matiere; Daniel Iagolnitzer Fdn; Ecole Polytechnique. pp. 1–32. <http://dx.doi.org/10.1007/978-3-0346-0428-41>. 12th Poincare Seminar on Biological Physics, Inst Henri Poincare, Paris, France, January 31, 2009.
- John, K., Peyla, P., Kassner, K., Prost, J., Misbah, C., 2008. Nonlinear study of symmetry breaking in actin gels: implications for cellular motility. *Phys. Rev. Lett.* 100, <http://dx.doi.org/10.1103/PhysRevLett.100.068101>.
- Jülicher, F., Kruse, K., Prost, J., Joanny, J.F., 2007. Active behavior of the cytoskeleton. *Phys. Rep.—Rev. Sect. Phys. Lett.* 449, 3–28, <http://dx.doi.org/10.1016/j.physrep.2007.02.018>.
- Keller, H., Zadeh, A.D., Eggli, P., 2002. Localised depletion of polymerised actin at the front of walker carcinosarcoma cells increases the speed of locomotion. *Cell Motil. Cytoskelet.* 53, 189–202.
- Kimpton, L., Whiteley, J., Waters, S., Oliver, J., 2014. On a poroviscoelastic model for cell crawling. *J. Math. Biol.*, 1–39.
- Koiter, W., 1976. Current Trends in the Theory of Buckling, Budiansky, Bernard, editor, Buckling of Structures, International Union of Theoretical and Applied Mechanics. Springer, Berlin Heidelberg, pp. 1–16, isbn 978-3-642-50994-0, http://dx.doi.org/10.1007/978-3-642-50992-6_1.
- Kole, T., Tseng, Y., Jiang, L., Katz, J., Wirtz, D., 2005. Intracellular mechanics of migrating fibroblasts. *Mol. Biol. Cell* 16, 328–338.
- Kozlov, M.M., Mogilner, A., 2007. Model of polarization and bistability of cell fragments. *Biophys. J.* 93, 3811–3819, <http://dx.doi.org/10.1529/biophysj.107.110411>.
- Kruse, K., Joanny, J., Jülicher, F., Prost, J., Sekimoto, K., 2005. Generic theory of active polar gels: a paradigm for cytoskeletal dynamics. *Eur. Phys. J. E* 16, 5–16, <http://dx.doi.org/10.1140/epje/e2005-00002-5>.
- Kruse, K., Joanny, J.F., Jülicher, F., Prost, J., 2006. Contractility and retrograde flow in lamellipodium motion. *Phys. Biol.* 3, 130–137, <http://dx.doi.org/10.1088/1478-3975/3/2/005>.
- Kruse, K., Jülicher, F., 2000. Actively contracting bundles of polar filaments. *Phys. Rev. Lett.* 85, 1778–1781, <http://dx.doi.org/10.1103/PhysRevLett.85.1778>.
- Kruse, K., Jülicher, F., 2003. Self-organization and mechanical properties of active filament bundles. *Phys. Rev. E* 67, 051913, <http://dx.doi.org/10.1103/PhysRevE.67.051913>. URL: <http://link.aps.org/doi/10.1103/PhysRevE.67.051913>.
- Kruse, K., Zumdick, A., Jülicher, F., 2003. Continuum theory of contractile fibres. *Europhys. Lett.* 64, 716. URL: <http://stacks.iop.org/0295-5075/64/i=5/a=716>.
- Lancaster, O., Le Berre, M., Dimitracopoulos, A., Bonazzi, D., Zlotek-Zlotkiewicz, E., Picone, R., Duke, T., Piel, M., Baum, B., 2013. Mitotic rounding alters cell geometry to ensure efficient bipolar spindle formation. *Dev. Cell* 25, 270–283, <http://dx.doi.org/10.1016/j.devcel.2013.03.014>. URL: <http://www.sciencedirect.com/science/article/pii/S1534580713001858>.
- Lancaster, O.M., Baum, B., 2014. Shaping up to divide: coordinating actin and microtubule cytoskeletal remodelling during mitosis. *Semin. Cell Dev. Biol.* 34, 109–115, <http://dx.doi.org/10.1016/j.semcdb.2014.02.015>. URL: <http://www.sciencedirect.com/science/article/pii/S1084952114000275>.
- Larripa, K., Mogilner, A., 2006. Transport of a 1D viscoelastic actin–myosin strip of gel as a model of a crawling cell. *Phys. A—Stat. Mech. Appl.* 372, 113–123, <http://dx.doi.org/10.1016/j.physa.2006.05.008>. Workshop on Common Trends in Traffic Systems, Kanpur, India, February 08–10, 2006.
- LeVeque, R., 2002. Finite Volume Methods for Hyperbolic Problems, vol. 31. Cambridge University Press ISBN: 9780521009249.
- Lin, Y., 2010. A model of cell motility leading to biphasic dependence of transport speed on adhesive strength. *J. Mech. Phys. Solids* 58, 502–514.
- Lin, Y., Inamdar, M., Freund, L., 2008. The competition between Brownian motion and adhesion in soft materials. *J. Mech. Phys. Solids* 56, 241–250.
- Liu, Z., Van Grunsven, L.A., van Rossen, E., Schroyen, B., Timmermans, J.P., Geerts, A., Reynaert, H., 2010. Blebbistatin inhibits contraction and accelerates migration in mouse hepatic stellate cells. *Br. J. Pharmacol.* 159, 304–315.
- Löber, J., Ziebert, F., Aranson, I.S., 2014. Modeling crawling cell movement on soft engineered substrates. *Soft Matter* 10, 1365–1373.
- Lombardi, M.L., Knecht, D.A., Dembo, M., Lee, J., 2007. Traction force microscopy in dictyostelium reveals distinct roles for myosin II motor and actin-crosslinking activity in polarized cell movement. *J. Cell Sci.* 120, 1624–1634, <http://dx.doi.org/10.1242/jcs.002527>.
- Loosley, A.J., Tang, J.X., 2012. Stick-slip motion and elastic coupling in crawling cells. *Phys. Rev. E* 86, <http://dx.doi.org/10.1103/PhysRevE.86.031908>.
- Luo, T., Mohan, K., Srivastava, V., Ren, Y., Iglesias, P.A., Robinson, D.N., 2012. Understanding the cooperative interaction between myosin II and actin cross-linkers mediated by actin filaments during mechanosensation. *Biophys. J.* 102, 238–247.
- Marchetti, M., Joanny, J., Ramaswamy, S., Liverpool, T., Prost, J., Rao, M., Simha, R.A., 2013. Hydrodynamics of soft active matter. *Rev. Mod. Phys.* 85, 1143.
- Mayer, M., Depken, M., Bois, J.S., Jülicher, F., Grill, S.W., 2010. Anisotropies in cortical tension reveal the physical basis of polarizing cortical flows. *Nature* 467, <http://dx.doi.org/10.1038/nature09376>. 617–U150.
- Meurant, G., 1992. A review on the inverse of symmetrical tridiagonal and block tridiagonal matrices. *SIAM J. Matrix Anal. Appl.* 13, 707–728.
- Mi, Q., Swigon, D., Riviere, B., Cetin, S., Vodovotz, Y., Hackam, D.J., 2007. One-dimensional elastic continuum model of enterocyte layer migration. *Biophys. J.* 93, 3745–3752, <http://dx.doi.org/10.1529/biophysj.107.112326>.
- Mofrad, M.R.K., 2009. Rheology of the cytoskeleton. *Annu. Rev. Fluid Mech.* 41, 433–453, <http://dx.doi.org/10.1146/annurev.fluid.010908.165236>.
- Mogilner, A., 2009. Mathematics of cell motility: have we got its number? *J. Math. Biol.* 58, 105–134, <http://dx.doi.org/10.1007/s00285-008-0182-2>.

- International Conference on Industrial and Applied Mathematics, Zurich, Switzerland, 2007.
- Mogilner, A., Edelstein-Keshet, L., 2002. Regulation of actin dynamics in rapidly moving cells: a quantitative analysis. *Biophys. J.* 83, 1237–1258.
- Mori, Y., Jilkine, A., Edelstein-Keshet, L., 2008. Wave-pinning and cell polarity from a bistable reaction–diffusion system. *Biophys. J.* 94, 3684–3697, <http://dx.doi.org/10.1529/biophysj.107.120824>. URL: (<http://www.sciencedirect.com/science/article/pii/S0006349508704442>).
- Nirenberg, L., 1974. Topics in Nonlinear Functional Analysis, vol. 6. American Mathematical Society. ISBN-10: 0-8218-2819-3, ISBN-13: 978-0-8218-2819-9.
- Noselli, G., Tatone, A., DeSimone, A., 2014. Discrete one-dimensional crawlers on viscous substrates: achievable net displacements and their energy cost. *Mech. Res. Commun.* 58, 73–81. ISSN 0093-6413, <http://dx.doi.org/10.1016/j.mechrescom.2013.10.023>.
- Novak, I.L., Slepchenko, B.M., Mogilner, A., Loew, L.M., 2004. Cooperativity between cell contractility and adhesion. *Phys. Rev. Lett.* 93, 268109.
- Ohtsuka, H., 2002. A concentration phenomenon around a shrinking hole for solutions of mean field equations. *Osaka J. Math.* 39, 395–407.
- Oliver, J., King, J., McKinlay, K., Brown, P., Grant, D., Scotchford, C., Wood, J., 2005. Thin-film theories for two-phase reactive flow models of active cell motion. *Math. Med. Biol.* 22, 53–98.
- Paluch, E., van der Gucht, J., Sykes, C., 2006. Cracking up: symmetry breaking in cellular systems. *J. Cell Biol.* 175, 687–692.
- Panorchan, P., Lee, J.S.H., Kole, T.P., Tseng, Y., Wirtz, D., 2006. Microrheology and ROCK signaling of human endothelial cells embedded in a 3D matrix. *Biophys. J.* 91, 3499–3507, <http://dx.doi.org/10.1529/biophysj.106.084988>.
- Perthame, B., 2012. Growth, Reaction, Movement and Diffusion from Biology. Lecture Notes, University Paris, Citeseer.
- Poincloux, Renaud, Collin, Olivier, Lizárraga, Floria, Romao, Maryse, Debray, Marcel, Piel, Matthieu, Chavrier, Philippe, 2011. Contractility of the cell rear drives invasion of breast tumor cells in 3D matrigel. *PNAS* 108 (5), 1943–1948, <http://dx.doi.org/10.1073/pnas.1010396108>.
- Pritchard, R.H., Shery Huang, Y.Y., Terentjev, E.M., 2014. Mechanics of biological networks: from the cell cytoskeleton to connective tissue. *Soft Matter* 10, 1864–1884, <http://dx.doi.org/10.1039/C3SM52769G>.
- Purcell, E.M., 1977. Life at low Reynolds number. *Am. J. Phys.* 45, 3–11, <http://dx.doi.org/10.1119/1.10903>.
- Rafelski, S., Theriot, J., 2004. Crawling toward a unified model of cell motility: spatial and temporal regulation of actin dynamics. *Annu. Rev. Biochem.* 73, 209–239, <http://dx.doi.org/10.1146/annurev.biochem.73.011303.073844>.
- Recho, P., Joanny, J.F., Truskinovsky, L., 2014. Optimality of contraction-driven crawling. *Phys. Rev. Lett.* 112, 218101.
- Recho, P., Putelat, T., Truskinovsky, L., 2013. Contraction-driven cell motility. *Phys. Rev. Lett.* 111, 108102.
- Recho, P., Truskinovsky, L., 2013. Asymmetry between pushing and pulling for crawling cells. *Phys. Rev. E* 87, 022720, <http://dx.doi.org/10.1103/PhysRevE.87.022720>. URL: <http://link.aps.org/doi/10.1103/PhysRevE.87.022720>.
- Ren, X., Truskinovsky, L., 2000. Finite scale microstructures in nonlocal elasticity. *J. Elast.* 59, 319–355, <http://dx.doi.org/10.1023/A:1011003321453>.
- Ronan, W., Deshpande, V.S., McMeeking, R.M., McGarry, J.P., 2014. Cellular contractility and substrate elasticity: a numerical investigation of the actin cytoskeleton and cell adhesion. *Biomech. Model. Mechanobiol.* 13, 417–435.
- Rubinstein, B., Fournier, M.F., Jacobson, K., Verkhovsky, A.B., Mogilner, A., 2009. Actin–myosin viscoelastic flow in the Keratocyte Lamellipod. *Biophys. J.* 97, 1853–1863, <http://dx.doi.org/10.1016/j.bpj.2009.07.020>.
- Saintillan, D., Shelley, M.J., 2012. Emergence of coherent structures and large-scale flows in motile suspensions. *J. R. Soc. Interface* 9, 571–585, <http://dx.doi.org/10.1098/rsif.2011.0355>.
- Salbreux, G., Prost, J., Joanny, J.F., 2009. Hydrodynamics of cellular cortical flows and the formation of contractile rings. *Phys. Rev. Lett.* 103, 058102, <http://dx.doi.org/10.1103/PhysRevLett.103.058102>. URL: <http://link.aps.org/doi/10.1103/PhysRevLett.103.058102>.
- Sankararaman, S., Ramaswamy, S., 2009. Instabilities and waves in thin films of living fluids. *Phys. Rev. Lett.* 102, 118107, <http://dx.doi.org/10.1103/PhysRevLett.102.118107>. URL: <http://link.aps.org/doi/10.1103/PhysRevLett.102.118107>.
- Schreiber, C.H., Stewart, M., Duke, T., 2010. Simulation of cell motility that reproduces the force–velocity relationship. *Proc. Natl. Acad. Sci. U. S. A.* 107, 9141–9146, <http://dx.doi.org/10.1073/pnas.1002538107>.
- Schwarz, U., Safran, S., 2013. Physics of adherent cells. *Rev. Mod. Phys.* 85, 1327–1381, <http://dx.doi.org/10.1103/RevModPhys.85.1327>. URL: <http://link.aps.org/doi/10.1103/RevModPhys.85.1327>.
- Schwarz, U.S., Gardel, M.L., 2012. United we stand – integrating the actin cytoskeleton and cell-matrix adhesions in cellular mechanotransduction. *J. Cell Sci.* 125, 3051–3060, <http://dx.doi.org/10.1242/jcs.093716>.
- Senba, T., Suzuki, T., 2000. Some structures of the solution set for a stationary system of chemotaxis. *Adv. Math. Sci. Appl.* 10, 191–224.
- Shao, D., Rappel, W.J., Levine, H., 2010. Computational model for cell morphodynamics. *Phys. Rev. Lett.* 105, <http://dx.doi.org/10.1103/PhysRevLett.105.108104>.
- Simha, R., Ramaswamy, S., 2002. Hydrodynamic fluctuations and instabilities in ordered suspensions of self-propelled particles. *Phys. Rev. Lett.* 89, <http://dx.doi.org/10.1103/PhysRevLett.89.058101>.
- Stewart, M.P., Helenius, J., Toyoda, Y., Ramanathan, S.P., Muller, D.J., Hyman, A.A., 2011. Hydrostatic pressure and the actomyosin cortex drive mitotic cell rounding. *Nature* 469, 226–230.
- Stossel, T., 1993. On the crawling of animal-cells. *Science* 260, 1086–1094.
- Stroka, K.M., Jiang, H., Chen, S.H., Tong, Z., Wirtz, D., Sun, S.X., Konstantopoulos, K., 2014. Water permeation drives tumor cell migration in confined microenvironments. *Cell* 157, 611–623.
- Struwe, M., Tarantello, G., 1998. On multivortex solutions in Chern–Simons gauge theory. *Boll. Unione Mat. Ital.-B*, 109–122.
- Tawada, K., Sekimoto, K., 1991. Protein friction exerted by motor enzymes through a weak-binding interaction. *J. Theor. Biol.* 150, 193–200, [http://dx.doi.org/10.1016/S0022-5193\(05\)80331-5](http://dx.doi.org/10.1016/S0022-5193(05)80331-5).
- Taylor, G., 1951. Analysis of the swimming of microscopic organisms. *Proc. R. Soc. London. Ser. A. Math. Phys. Sci.* 209, 447–461.
- Tjhung, E., Marenduzzo, D., Cates, M.E., 2012. Spontaneous symmetry breaking in active droplets provides a generic route to motility. *Proc. Natl. Acad. Sci. U. S. A.* 109, 12381–12386.
- Tjhung, E., Tiribocchi, A., Marenduzzo, D., Cates, M., 2015. A minimal physical model captures the shapes of crawling cells. *Nat. Commun.* 6.
- Torres, P.G., Dubrovinski, K., Kruse, K., 2010. Filament turnover stabilizes contractile cytoskeletal structures. *Europhys. Lett.* 91, <http://dx.doi.org/10.1209/0295-5075/91/68003>.
- Trepat, X., Wasserman, M.R., Angelini, T.E., Millet, E., Weitz, D.A., Butler, J.P., Fredberg, J.J., 2009. Physical forces during collective cell migration. *Nat. Phys.* 5, 426–430.
- Turlier, H., Audoly, B., Prost, J., Joanny, J.F., 2014. Furrow constriction in animal cell cytokinesis. *Biophys. J.* 106, 114–123, <http://dx.doi.org/10.1016/j.bpj.2013.11.014>. URL: (<http://www.sciencedirect.com/science/article/pii/S0006349513012447>).
- Vanderlei, B., Feng, J.J., Edelstein-Keshet, L., 2011. A computational model of cell polarization and motility coupling mechanics and biochemistry. *Multiscale Model. Simul.* 9, 1420–1443, <http://dx.doi.org/10.1137/100815335>. URL: (<http://link.aip.org/link/?MMS/9/1420/1>).
- Vedula, S.R.K., Leong, M.C., Lai, T.L., Hersen, P., Kabla, A.J., Lim, C.T., Ladoux, B., 2012. Emerging modes of collective cell migration induced by geometrical constraints. *Proc. Natl. Acad. Sci. U. S. A.* 109, 12974–12979.
- Verkhovsky, A., Svitkina, T., Borisy, G., 1999. Self-polarization and directional motility of cytoplasm. *Curr. Biol.* 9, 11–20, [http://dx.doi.org/10.1016/S0960-9822\(99\)80042-6](http://dx.doi.org/10.1016/S0960-9822(99)80042-6).
- Vicente-Manzanares, M., Ma, X., Adelstein, R.S., Horwitz, A.R., 2009. Non-muscle myosin II takes centre stage in cell adhesion and migration. *Nat. Rev. Mol. Cell Biol.* 10, 778–790, <http://dx.doi.org/10.1038/nrm2786>.
- Wang, Q., Yang, X., Adalsteinsson, D., Elston, T.C., Jacobson, K., Kapustina, M., Forest, M.G., 2012. Computational and Modeling Strategies for Cell Motility, 257–296.
- Wolgemuth, C.W., Stajic, J., Mogilner, A., 2011. Redundant mechanisms for stable cell locomotion revealed by minimal models. *Biophys. J.* 101, 545–553, <http://dx.doi.org/10.1016/j.bpj.2011.06.032>.
- Wottawah, F., Schinkinger, S., Lincoln, B., Ananthakrishnan, R., Romeyke, M., Guck, J., Kas, J., 2005. Optical rheology of biological cells. *Phys. Rev. Lett.* 94, <http://dx.doi.org/10.1103/PhysRevLett.94.028101>.

[//dx.doi.org/10.1103/PhysRevLett.94.098103](http://dx.doi.org/10.1103/PhysRevLett.94.098103).

- Yam, P.T., Wilson, C.A., Ji, L., Hebert, B., Barnhart, E.L., Dye, N.A., Wiseman, P.W., Danuser, G., Theriot, J.A., 2007. Actin–myosin network reorganization breaks symmetry at the cell rear to spontaneously initiate polarized cell motility. *J. Cell Biol.* 178, 1207–1221, <http://dx.doi.org/10.1083/jcb.200706012>.
- Ziebert, F., Aranson, I.S., 2013. Effects of adhesion dynamics and substrate compliance on the shape and motility of crawling cells. *PloS One* 8, e64511.
- Ziebert, F., Swaminathan, S., Aranson, I.S., 2012. Model for self-polarization and motility of keratocyte fragments. *J. R. Soc. Interface* 9, 1084–1092, <http://dx.doi.org/10.1098/rsif.2011.0433>.